

GUIDED SURGERY USING RAPID PROTOTYPING PATIENT-SPECIFIC GUIDES:  
A METHODOLOGY TO QUANTIFY MECHANICAL STABILITY  
AND UNIQUENESS OF FIT

By

BARBARA GARITA

A DISSERTATION PRESENTED TO THE GRADUATE SCHOOL  
OF THE UNIVERSITY OF FLORIDA IN PARTIAL FULFILLMENT  
OF THE REQUIREMENTS FOR THE DEGREE OF  
DOCTOR OF PHILOSOPHY

UNIVERSITY OF FLORIDA

2007

© 2007 Barbara Garita

To Donato, Noemi, Esteban, Pablo, Ifi, Ignacio and Natalia.

## ACKNOWLEDGMENTS

First, I must thank my committee for taking the time to work with me during this endeavor. I must also express gratitude to my advisor Dr. Frank Bova for persevering with me throughout the time it took me to complete this research and write this dissertation. Dr. Friedman, Dr. Gilland, Dr. Kim, and Dr. Vemuri have also been generous enough to dedicate their time and expertise to improve my work; I am grateful for their contributions and their kind support. I am grateful as well to Dr. Didier Rajon, for his timely appraisals of my work and useful suggestions throughout these years.

I must express my profound gratitude to Dr. Jonathan Earle for invaluable support and friendship, especially during the last year of my dissertation. Jeff Citty has been an immense support as well; working with him and the EFTP program for the last 4 years has given me a true sense of belonging while at the University of Florida.

I need to express my gratitude and deep appreciation to Sergio who always stood next to me in good times and bad times. I must acknowledge, as well the many friends and colleagues who assisted, advised and supported my research and writing efforts over the years, my gratitude goes to Ashley, Mafer, Ryanne, April, Luis, Mike, Pam, Atchar and Rolando.

Finally I sincerely thank my parents and siblings for encouraging my decision to stay away from home for so many years in order to accomplish these academic dreams. I find the time spent separated from them irreplaceable and I hope I will get the chance to make it all up in the near future.

## TABLE OF CONTENTS

|  | <u>page</u> |
|--|-------------|
| ACKNOWLEDGMENTS .....  | 4           |
| LIST OF TABLES .....   | 7           |
| LIST OF FIGURES .....  | 8           |
| ABSTRACT .....   | 12          |
| CHAPTER  |             |
| 1 INTRODUCTION .....   | 14          |
| 2 BACKGROUND AND SIGNIFICANCE.....                             | 19          |
| Image-Guided Surgery.....                                      | 19          |
| Frame-Base and Frameless Stereotactic Approaches.....          | 20          |
| Model Based Guidance.....                                      | 22          |
| Customized positioning frames for pedicle screw placement..... | 22          |
| Customized position frames for intracranial surgery .....      | 24          |
| Significance .....   | 27          |
| Facial Landmarks and Angles .....                              | 28          |
| The Finite Element Method and ITK.....                         | 29          |
| Elements Used in the Simulation .....                          | 30          |
| The space truss .....  | 30          |
| The linear tetrahedron .....                                   | 34          |
| Characteristics of Stiffness Matrices .....                    | 35          |
| Linear Solvers.....  | 35          |
| 3 MATERIALS .....  | 47          |
| 4 METHODOLOGY FOR MEASURING STABILITY.....                     | 54          |
| Introduction.....  | 54          |
| System Components and FEM Setup .....                          | 55          |
| External Forces.....   | 56          |
| Rigid Layer .....  | 56          |
| Bed of Springs .....   | 58          |
| Program Parameters.....  | 59          |
| Input Parameters.....  | 59          |
| Spring height .....  | 59          |
| External force magnitude .....                                 | 59          |
| Rigid layer height .....                                       | 60          |
| Difference in elasticity .....                                 | 60          |
| Output Parameters .....  | 60          |

|   |     |
|---|-----|
| Criteria.....                                       | 62  |
| TNT Ratio.....                                      | 63  |
| Single Point Criterion.....                         | 64  |
| TNT threshold.....                                  | 65  |
| Consistency of TNT threshold.....                   | 67  |
| Single Force Criterion.....                         | 67  |
| 5 PROGRAM DESCRIPTION AND VALIDATION.....           | 82  |
| Program Description.....                            | 82  |
| Validation of FEM elements.....                     | 85  |
| Linear Spring Validation.....                       | 85  |
| Tetrahedron Element Validation.....                 | 86  |
| A Simple Model Validation.....                      | 86  |
| 6 RESULTS AND DISCUSSION.....                       | 93  |
| 7 CONCLUSION AND FUTURE WORK.....                   | 109 |
| APPENDIX  |     |
| A PRINCIPLE OF VIRTUAL WORK AND ITK FEM MODULE..... | 111 |
| FEM Terminology for Truss Elements.....             | 111 |
| Principle of Virtual Work.....                      | 112 |
| ITK FEM and Principles of Virtual Work.....         | 113 |
| Displacement Functions.....                         | 115 |
| Shape Functions.....                                | 115 |
| Strain Displacement Equation.....                   | 116 |
| Local Element Stiffness Matrix.....                 | 117 |
| Gauss Quadrature.....                               | 118 |
| ITK FEM Module.....                                 | 119 |
| LIST OF REFERENCES.....                             | 123 |
| BIOGRAPHICAL SKETCH.....                            | 127 |

## LIST OF TABLES

| <u>Table</u> |  | <u>page</u> |
|--------------|--|-------------|
| 4-1          | Relationship between the tetrahedral height and a measure of the rigidity of the rigid layer.....  | 70          |
| 4-2          | Table that shows the relationship between the difference in elastic modulus between the rigid layer and the bed of springs and the rigidity measure and Cholmod's rcond value..... | 70          |
| 4-3          | Single point criteria.....   | 70          |
| 5-1          | Displacement in the X, Y and Z direction from the example in Figure 5-4 tested with the ITKFEM module and ANSYS.....   | 87          |
| 6-1          | Measurement of the facial angles for the three anatomical models.....  | 99          |
| 6-2          | Instability score, presented as the percentage of forces that resulted in instability and the total forces applied on a frame.....   | 99          |

## LIST OF FIGURES

| <u>Figure</u>  | <u>page</u> |
|--|-------------|
| 1-1 Components involved in this investigation and the prototypes for the new technique for performing image-guided surgery with patient-specific reference guides..... | 18          |
| 2-1 Pre-target localization and pre-surgical planning is done in a computer workstation.....   | 36          |
| 2-2 Procedures related to frame-based image guidance surgery.....  | 37          |
| 2-3 Frameless stereotactic surgery uses fiducials that are glued to the patient’s skin .....   | 37          |
| 2-4 Typical layout when frameless stereotactic surgery is employed.....  | 38          |
| 2-5 Template designs for the spine .....   | 38          |
| 2-6 Router guides for craniotomy .....   | 39          |
| 2-7 Biopsy guides.....   | 40          |
| 2-8 Rapid prototyping machines .....   | 41          |
| 2-9 Chart to visualize the significance of the present work .....  | 42          |
| 2-10 Facial landmarks .....  | 43          |
| 2-11 Facial angles.....  | 44          |
| 2-12 Space truss element has six displacements to establish its deformed position.....   | 45          |
| 2-13 Application of a force perpendicular to the axis of the space truss .....   | 45          |
| 2-14 Space truss in local coordinates.....   | 46          |
| 2-15 The linear tetrahedron has a unique numbering scheme.....   | 46          |
| 3-1 The three models used to evaluate the methodology for testing unique fit .....   | 49          |
| 3-2 Masks built for testing the methodology of fit.....  | 50          |
| 3-3 Cap-like reference frame.....  | 51          |
| 3-4 Virtually created half sphere test model .....   | 51          |
| 3-5 Placement of pins for a simple test on the real stability of the large and small masks.....  | 52          |
| 3-6 Coronal view of placement of the pins onto the real masks .....  | 52          |

|      |  |    |
|------|--|----|
| 3-7  | The method employed to demonstrate the difference in stability between the large and small masks. ....   | 53 |
| 4-1  | The methodology for stability of fit involves simulating a rigid layer onto of a deformable bed of springs.....  | 71 |
| 4-2  | Displacement of a mask as it responds to external forces. ....   | 72 |
| 4-3  | Triangulation of a customized positioning device proper to STL format.....   | 72 |
| 4-4  | Direction of the $N_{main}$ .....  | 73 |
| 4-5  | Nodes point on the rigid frame .....   | 73 |
| 4-6  | In a wedge three tetrahedral elements are fitted .....   | 74 |
| 4-7  | Schematic showing how the maximum rigidity fault is calculated .....   | 75 |
| 4-8  | The behavior of a linear spring element under the application of an axial force.....   | 75 |
| 4-9  | Schematic that demonstrates how each spring’s displacement was evaluated by identifying the normal ( $n_i$ ) and tangential ( $t_i$ ) displacement magnitudes.....                         | 76 |
| 4-10 | Schematic that shows why it is important to distinguish between the springs that are mostly in compression or tension and those that are basically slipping or have a high TNT ratio ..... | 77 |
| 4-11 | Bounding volume for a spring to be in compression .....  | 77 |
| 4-12 | Two-dimensional interpretation of the single point criteria .....  | 78 |
| 4-13 | Schematic to demonstrate the importance of evaluating the percentage slip of TNT ratio for each spring .....   | 78 |
| 4-14 | Schematic to shows at the level at which the TNT threshold was defined.....  | 79 |
| 4-15 | Empirical determination that the TNT threshold greater than 0.6 correlates with the training data, which says that the large masks are stable.....   | 79 |
| 4-16 | Empirical determination that the TNT threshold set smaller than 0.8 correlates with the training data, which says that the small masks are unstable. ....                                  | 80 |
| 4-17 | A case of the large Asian mask, which shows the consistency of an upper TNT threshold of 0.7 .....   | 80 |
| 4-18 | Schematic showing the relation between the volume of the entire frame ( $f_{vol}$ ) and the compression patch volume ( $c_{vol}$ ).....  | 81 |
| 4-19 | Box ratio interpretation. ....   | 81 |

|      |   |     |
|------|---|-----|
| 5-1  | Flow chart of program for testing the uniqueness of fit.....  | 88  |
| 5-2  | Original surface is extended in the positive normal direction to form the top surface and the points extended in the negative normal direction to become boundary condition points..... | 90  |
| 5-3  | Examples of all linear spring element or space truss tested in all 3-dimensions. ....   | 90  |
| 5-4  | Example of two tetrahedral elements used in the validation of the tetrahedral elements used in the program .....  | 91  |
| 5-5  | A corner frame that was used to validate the program .....  | 92  |
| 6-1  | Placement of Caucasian masks onto solid model .....   | 100 |
| 6-2  | Placement of Asian masks onto solid model .....   | 100 |
| 6-3  | Placement of infant masks onto solid model .....  | 101 |
| 6-4  | Placement of a cap-like reference frame onto an upper head model.....   | 101 |
| 6-5  | Surface plot color coded by the maximum full rotation angle for the Caucasian masks.....  | 102 |
| 6-6  | Surface plot color coded by the maximum full rotation angle for the Asian masks.....  | 102 |
| 6-7  | Surface plot color coded by the maximum tilt angle for the infant masks .....   | 103 |
| 6-8  | Surface plot color coded by maximum tilt angle for the cap reference frame design .....   | 103 |
| 6-9  | Surface plots color coded by maximum tilt angle for the half sphere test.....   | 104 |
| 6-10 | Normalized histogram of box ratios for each tilt angle ( $\theta$ ) for the Caucasian large mask.....   | 104 |
| 6-11 | Normalized histogram of box ratios for each tilt angle ( $\theta$ ) for the Caucasian small mask.....   | 105 |
| 6-12 | Normalized histogram of box ratios for each tilt angle ( $\theta$ ) for the Asian large mask. ....  | 105 |
| 6-13 | Normalized histogram of box ratios for each tilt angle ( $\theta$ ) for the Asian small mask.....   | 106 |
| 6-14 | Normalized histogram of box ratios for each tilt angle ( $\theta$ ) for the infant large mask. ....   | 106 |
| 6-15 | Normalized histogram of box ratios for each tilt angle ( $\theta$ ) for the infant small mask.....  | 107 |
| 6-16 | Normalized histogram of box ratios for each tilt angle ( $\theta$ ) for the cap reference frame design.....   | 107 |

|      |   |     |
|------|---|-----|
| 6-17 | Normalized histogram of box ratios for each tilt angle ( $\theta$ ) for the half sphere test..... | 108 |
| 6-18 | Profiles of solid models .....  | 108 |
| A-1  | Differential element subjected to real stresses and in equilibrium. ....                          | 121 |
| A-2  | The greater part of the ITK FEM library .....   | 122 |

Abstract of Dissertation Presented to the Graduate School  
of the University of Florida in Partial Fulfillment of the  
Requirements for the Degree of Doctor of Philosophy

GUIDED SURGERY USING RAPID PROTOTYPING PATIENT-SPECIFIC GUIDES:  
A METHODOLOGY TO QUANTIFY MECHANICAL STABILITY  
AND UNIQUENESS OF FIT

By

Barbara Garita

August 2007

Chair: Frank Bova  
Major: Biomedical Engineering

Rapid prototyping technology (3-dimensional printing) in conjunction with the virtual manipulation of computer-generated 3-D anatomical models rendered from diagnostic images (CT and MRI) is a novel technique for directing image-guided surgery. By incorporating a graphical user interface, the surgeon can plan an intracranial surgical procedure by fabricating a patient-specific reference frame (mask-like facial frame) through the use of rapid prototyping technology.

Early testing of these patient-specific frames revealed the necessity to include a step prior to fabrication to analyze the design of the frame for stability of fit. In response to this need, the objective in the present investigation is to develop a method that numerically assesses the frame's stability. The approach was to create a finite-element simulation that models the patient-specific reference frame as a rigid layer composed of linear tetrahedron elements under a deformable material simulated by a bed of linear spring elements. The program analyzes the displacement of the rigid layer by simulating external forces distributed around its perimeter. The stability of fit is characterized by the response of the linear springs.

Three patients with different facial anatomical features were selected as training data for testing the simulation program. For each case two patient-specific reference frames, one that involves more surface area and surface variations such as contours of the nose bridge and another that consists of less surface area and less surface variations, were built with Rapid prototyping based on the patient's 3-D anatomical facial models. In all three cases the methodology correlated a stability score with the stability of the real reference frames. In addition two more cases were evaluated; the first did not incorporate the facial structures and was design to hold onto the top of the head in a cap-like manner, the second case was a virtually created half sphere. In both cases it was expected to find no a unique fit, and correspondingly the simulation found both cases to be unstable.

## CHAPTER 1 INTRODUCTION

Starting in 2003, researchers in the radiosurgery and biology lab (RSB) at the University of Florida's McKnight Brain Institute developed the capability to fabricate a patient-specific reference frame that has a potential of becoming a new type of image-guided surgery (IGS) technique [33]. The fabrication of the patient-specific reference frame involves coding a series of algorithms that render a detailed 3-dimensional life-like anatomical model from computer tomography (CT) or magnetic resonance imaging (MRI) [6] datasets (Figure 1-1). Onto a patient-specific 3-dimensional anatomical model a surface is selected (virtually "painted") from which the patient-specific reference frames are created. The ability to create, visualize, and manipulate 3-dimensional virtual anatomical models on a computer monitor heightened the enormous potential of utilizing medical image datasets to create customized reference frames for medical diagnostics and treatment, specifically in the area of image guidance surgery [36].

The objective the patient-specific reference frame is to replace existing technology of framed-based (fixing with pins a frame to the skull) and/or frameless (using fiducials and extra tracking equipment in the operation room) stereotactic systems [6]. Stereotactic techniques are used in neurological research and/or surgery to direct a surgical instrument (needle or electrode) into a specific location in the brain [1]. The patient-specific reference frames (or customized guiding template) are designed to tightly fit to a specific patient's facial anatomy contour [6] and allow guidance for neurosurgical applications such as craniotomies, biopsies, and deep brain stimulation [34].

Several clinical trials were initiated to test this new image-guided surgical approach. One of the first involved developing a customized guiding template that fitted onto vertebral bodies and served as a guide for pedicle screw placement. As the templates for vertebral bodies were

tested (through a non-significant risk IRB approved clinical trial) on actual patients in the operation room (OR), the research team quickly identified a problem that was defined within the context of biomedical engineering: the computer selected surface for the reference frame could not accurately predict the surface that the surgeon was able to present (because of the residual soft tissue), therefore “no unique surface” for the template could be identified. Eventually, the idea of using customized guiding templates for the spine was abandoned and the development of this approach for cranial procedures became the primary focus of the design application. The idea of using customized guiding templates for stereotactic surgery proved to have significant potential [33], but the problem of stability of fit was still apparent. The problem of the stability of fit for the reference frames became of great importance because of the need to add attachments to the reference frame for particular intracranial guidance surgeries (Figure 1-1D and 1-1E). As the distance between the reference frame and the attachments increases, the lever arm increases and small movements on the reference frame will result in exaggerated moments on the attachments tips (Figure 1-1D). For this reason, the accuracy of the patient-specific reference frames depends upon the identification of a broad and conforming patient surface. This surface must allow a reference frame mask (negative from the anatomical model’s surface) to be designed in a manner that prevents both rotations and translations. In other words, the mask must fit tightly onto the patient’s surface and not slide or wiggle. Hence, the initiative of the present investigation stems from the necessity to solve this stability problem by developing a numerical methodology to evaluate the patient-specific frame’s design by testing its stability of fit prior to fabrication with Rapid prototyping technology.

The methodology developed for testing stability of fit relies on the creation of a finite element simulation program that models contact interactions between patient-specific frame and

the patient's anatomical face model (Figure 1-1). The approach used is the idealization of a contact mechanics problem by means of the simulating the patient-specific reference frame as a rigid layer composed of linear tetrahedron elements under a deformable material simulated by a bed of linear springs (or truss) elements. The approach will simulate the movement of the rigid tetrahedral layer by the application of external forces onto the frame's surface. As training data for the methodology, three solid life-like anatomical face models of three patients with notably dissimilar facial profiles were created with rapid prototyping and for each patients two frames one the is known to be stable and the other one known to be unstable were also created. The methodology for testing stability of the frames involves two criteria, both based on the resulting simulated movement of the frames onto the patients' 3-dimensional anatomical models. The first criterion is concern with identifying locations of excessive movement and the second criterion provides with a yes or no answer to the stability of the frame on a per force basis. It will be shown that these two criteria are able to predict the degree of instability of the selected surface-mask construct; by identifying when the construct is able to resist translations and rotations to typical external force directions.

The methodology to test uniqueness of fit presented in this investigation is an essential component to the new technique for image-guided surgery that involves rapid prototyping. The design of the patient-specific reference frame has the imperative requirement to have a unique fit onto the patient's anatomy, this is the major concern of this new image-guided surgery technology [33]. Therefore the work presented here, which numerically evaluates the mechanical stability and uniqueness of fit of the patient-specific reference frame, will overcome this major problem and will allow a surgeon to use the new technology with more confidence and accuracy. In this way, the new IGS technology is a step closer towards being distributed to other the

medical communities. In addition, the methodology has been written in the same language and uses the same open source libraries as the main graphical user interface, from which the patient-specific reference frames are designed, so it can be easily adapted as a module component.

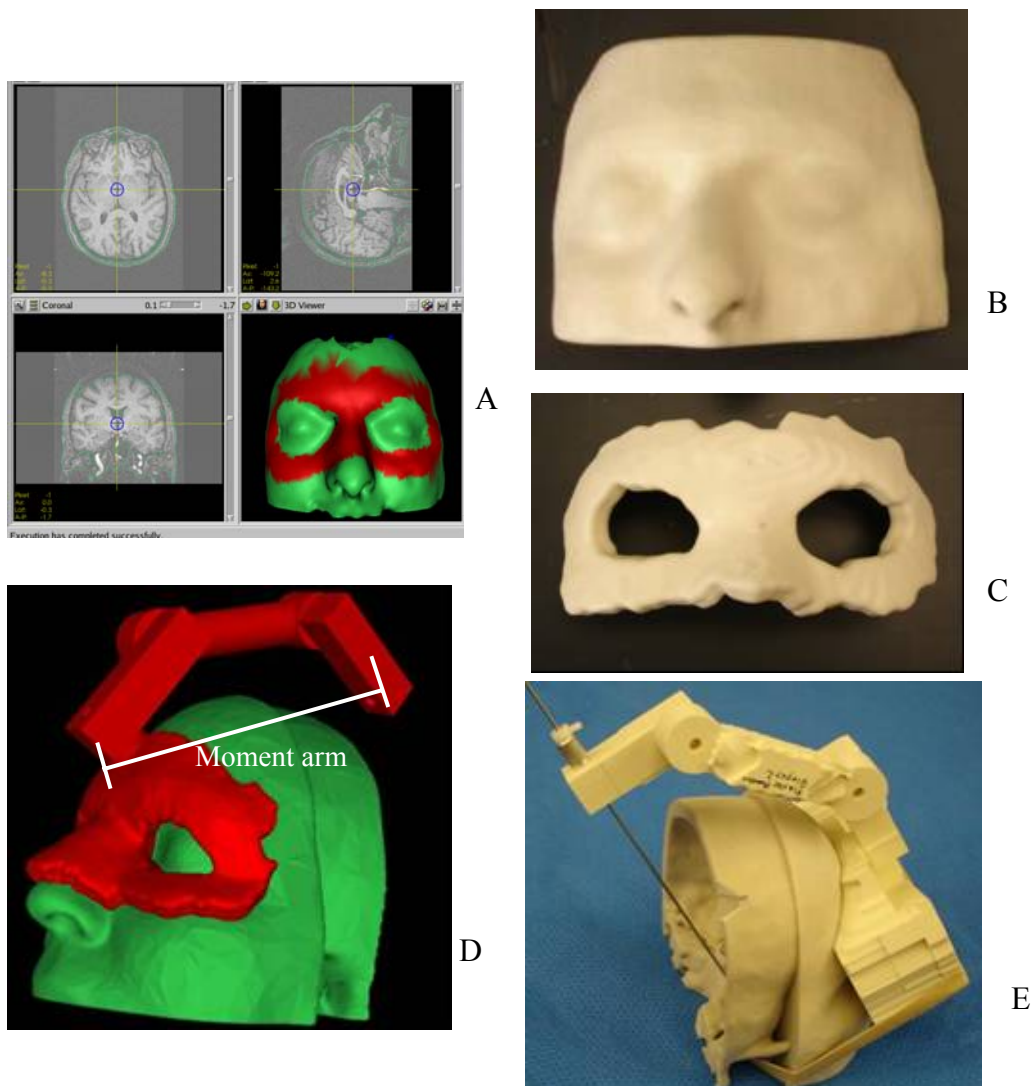


Figure 1-1. Components involved in this investigation and the prototypes for the new technique for performing image-guided surgery with patient-specific reference guides. A) The graphical user interface that can create 3-dimensional patient anatomical model from a series of 2-dimensional medical image datasets, and the selection of a contour surface (in red) for the fabrication of a patient-specific reference frames. B) Physical patient's anatomical model created with Rapid prototyping for evaluating the stability of fit. C) Patient-specific reference frames that conformingly fits onto the patient's model. D) Virtual model and reference frame with attachments to guide a biopsy probe. As the moment arm increases, small rotations and translation on the mask will have an exaggerated effect at the level of the attachment tip. E) Physical reference frame and attachments to guide a biopsy probe.

## CHAPTER 2 BACKGROUND AND SIGNIFICANCE

### **Image-Guided Surgery**

During the early 20th century, Sir Victor Horsley recognized the need for targeting specific diseased regions in the brain without injuring neighboring healthy structures. He hired an engineer to provide with a method to solve the problem; the engineer came up with the idea of using three imaginary orthogonal spatial planes (horizontal, frontal and sagittal) [23] to specify any location in the brain. Later, during the mid 20<sup>th</sup> century, Spiegel and Wycis et al. [41] introduced the first stereotactic application. As it was originally envisioned, the stereotactic approach relates to movement in 3-dimensional space; therefore, stereotactic surgery uses a 3-dimensional coordinate system to locate small targets inside the brain. Spiegel and Wycis et al. [44], began the work of locating specific regions in the brain using intrinsic reference points and in 1952 [43] they published the first stereotactic map of the brain using the pineal body as the only reference point. However, this localization technique proved unreliable because of anatomical differences between patients and as the surgeons moved further from their reference point they lost accuracy. Seeking to improve the reliability of their technique, Spiegel and Wycis et al. developed the approach of fitting a custom cap to the patient and attaching a head ring to this cap; in this way they established a relation between the brain atlas and a reference head ring [43].

Besides the Spiegel and Wycis custom cap apparatus, during the following year several others investigators developed stereotactic devices for different purposes and with different usage methods [18]. Some systems were based on Cartesian coordinates, others used polar coordinates for placing electrodes at target locations; while some designs moved the patient's

head towards a target location; others used interlocking arcs to move the apparatus to get to a specific location [18].

With the advent of computer tomography (CT), imaging of the brain became readily available. The Brown-Roberts-Wells (BRW) system was the first to be designed particularly for use with CT images and was the first to implement a computer base algorithm to calculate coordinates and a trajectory to a target point [22]. As a result, a specific patient's anatomical information obtained through CT imaging was, for the first time, properly visualized and referenced to a head ring [36]. Later, in 1987, Schad et al. [36] introduced multimodality image registration, which increased the accuracy and tissue differentiation for stereotactic targeting.

### **Frame-Base and Frameless Stereotactic Approaches**

Today image guidance procedures can be divided in two categories, according to different referencing methods employed. These are generally termed frame-base and frameless stereotactic approaches. The purpose of both is to provide the surgeon with an understanding of the anatomy beneath the visible operative surface. State of the art stereotactic procedures allow the surgeon to physically relate spatial information from a set of diagnostic images (represented by a patient's 3-dimensional virtual model), onto a patient's actual, real-world anatomy in a reliable and accurate manner. In general, this is accomplished by means of a discernible reference frame (or landmarks) that are integrated in both the virtual patient's model and the real-world patient and correlates the information amongst them. The creation of a diagnostic plan, for both frame-base and frameless stereotactic surgeries, is performed on the virtual, computer generated patient, where image datasets (MR and CT) depict the anatomical information together with the rigid frame landmarks for frame-based or skin landmarks for frameless stereotactic surgeries (Figure 2-1) [6].

Frame-base stereotactic surgery is the most accurate technique available [32], but it is not free of significant disadvantages. This represents the most accurate method because it rigidly fixes a reference frame onto the patient's skull, through the use of minimally invasive pins. For example, in the case of a stereotactic frame-based biopsy a head ring is applied to the patient prior to imaging (Figure 2-2A). The diagnostic scan will allow the surgeon to visualize the intracranial anatomy and create a virtual surgical plan on a computer workstation. With a graphical user interface the surgeon will define the intracranial target location and the computer system will mathematically calculate the corresponding coordinates relating the virtual plan to the real world patient anatomy (Figure 2-1). The coordinates are set on the physical stereotactic system (Figure 2-2B) (which is directly fixed onto the rigid frame), providing a guide or trajectory for the surgeon [8, 35].

The main shortcomings of frame-base stereotactic surgery include the extend of time that the procedure takes (from to pre-surgical frame application to surgery completion), the specific expertise required for frame application, the high cost of replacement equipment, and the discomfort that the head ring causes on the patient. Indeed, the rigid frame is a discomfort for the patient at the time of imaging and during the preparation of the sterile field, and it gets in the way of the surgical procedures in general. Nevertheless, frame-base image-guided surgery provides the gold standard for precision and accuracy for intracranial stereotactic procedures.

Frameless stereotactic surgery has been presented as an alternative to frame-based procedures. The main difference between frame-based and frameless stereotactic systems, is that instead of a head ring, fiducials (landmarks) are used (Figure 2-3). For cranial surgery these are either MR and CT identifiable markers that are temporally glued onto the patient's skin [2, 51] or anatomical landmarks are defined on 3-dimensional rendered images base upon the patient's CT

or MR datasets [39]. In both cases, the procedures do not have to be completed in an extended and continuous span of time. Both frame-based and frameless procedures permit the same virtual computer planning to be performed by the surgeon; however frameless stereotactic surgery requires instrument-tracking equipment within the operating room (OR) [51].

The main drawback of the frameless approach is the necessity for registration of the fiducials with a reference frame used to track movement between the patient and the surgical tools [6]. The registration requires special cameras (electromagnetic) and additional computer workstations to be present in an already crowded operating room (Figure 2-4). Although electromagnetic tracking allows for non-line of sight tracking, the surgical team is still burdened with the additional computers in the OR [6], special traceable instruments, the need to minimize ferrous metals from with the operative field and the registration procedures.

## **Model Based Guidance**

### **Customized positioning frames for pedicle screw placement**

As mentioned in the introduction, researchers in the RSB lab initially built customized guiding templates to fit onto vertebral bodies for the placement of pedicle screws. It was during the testing of these spine templates that the problem of uniqueness of fit was first addressed. The following section provides background information on the first implementations of custom guiding templates for the spine and also provides additional information to aid in better understanding of the problem at hand.

Stereotactic guidance with the aid of customized guiding templates initiated in 1999 for the placement of pedicle screws [20]. In 1999, Goffin et al. [20] first published a paper that explained about a guide for the posterior transarticular screw fixation of C1-C2 (cervical 1 to cervical 2); and in 2001, Goffin et al. [21], Birnbaum et al. [6] and Yoo et al. [50] published papers referring again to template guides for placement of pedicle screws in the spine (Figure 2-5

A-C). While Goffin et al. [20] developed templates for the fixation of the cervical spine, Birnbaum et al. [6] and Yoo et al. [50] tested particularly on the lumbar spine of cadavers and humans.

All three research groups used rendered 3-dimensional CT information to create the template guides based on the bony surface of the spine. Goffin et al. [20] printed the 3-D solid models of the cervical spine with stereolithography and physically defined the correct placement of the pedicle screws, and then he translated the trajectory to a CAD (Computer Aided Design) program. Goffin et al. [21] and Birnbaum et al. [6] used computer controlled milling machines or NC (numerically controlled) machines to create the template guides; Yoo et al. used FDM (Fused Deposition modeling), a machine from Stratasys (Stratasys, Tempe, AZ), that follows the same principle of stereolithography but is composed of a movable nozzles where melted plastic forms the template one layer at a time.

Goffin et al. [21] manufactured the device on an acrylate resin and the template had a horseshoe appearance that was positioned on the posterior aspect of C2 (Figure 2-5 A). He tested on some cadavers and two patients. On the cadavers he initially experienced rotational instability of the template and increased the contact area to include more vertebral support. On one of the two patient cases he was successful; while on the other the template guide did not perform well. Birnbaum et al. [6] created polycarbonate templates with NC machines (Figure 2-5 B), and conducted a cadaveric study comparing computer-assisted surgery with individual templates on thirteen lumbar spines. Under image-guided technique, he found two misplaced screws; while all were correctly placed when using the template guides. Yoo's templates were constructed from ABS plastic and expanded over a large contact area comprising both transverse

processes, the laminae areas and the spinous process [50]. He tested on dry dissected vertebrae. In all cases the positions of the screws were evaluated with postoperative CT scans.

A later paper by Van Cleynenbreugel et al. [47], published in 2002, focuses on the validation of the template guides for the C1-C2 transarticular screws (continuing on Goffin's work). As the others had previously done, he used a preoperative CT to base the design of the template and the testing was done on cadavers. During the first part of the study, he ran into some serious instability issues, particularly in the direction of the application of the drilling force; the result was dramatic displacement of the template guide on the order of 2 to 9 mm. Consequently, they altered the design of the template guides to include more support and had significantly better results.

The appearance of the templates developed by the three researchers resembled a block that overlaps a broad surface area over the spine. From the experience gained in the RSB Lab, it was found that the templates that overlap a broad area on the spine create the necessity of removing a large amount of muscle tissue to expose the mating bony surface of the spine; this design is not beneficial for the patient and time consuming for the surgeon; in addition residual soft tissue causes the surface conformity between the template and the anatomy to be disrupted. As a consequence, the work on custom guiding templates for the spine was abandoned; however important knowledge was learned from the experience. Figure 1-5 shows the template designs published by other investigators and the initial designs of the spine template from the RSB lab.

### **Customized position frames for intracranial surgery**

The first to suggest customized position frames for the head was D'Urso et al. [16]. His approach involved implanting reference sockets on a patient's skull prior to scanning. Then from the diagnostic images he create a physical 3-dimensional model of the patient head that included the mounting sockets. The surgical trajectory was planned on the solid model by

attaching a reference arc to the mounting sockets. By correspondence, the arc was refitted onto the patient and directed the surgeon to the predetermined location in the brain.

The technology developed in the RSB for performing image-guided surgery by use of patient-specific frames has been shown to have superior accuracy and precision when compared to previously documented frame-based procedures [33]. Rajon et al. [33] used a simple phantom to measure the point localization accuracy of the customized guiding frames. He found that the technology could position a probe tip with an accuracy of 1.7mm. As mentioned before, the standard in terms of accuracy for image-guided surgery is the frame-based approach. The overall system accuracy of a standard frame based procedure was measured by Maciunas et al. [27] and determined to be 2.28mm. Their accuracy measurement is an estimated measure of the imaging accuracy and the mechanical system accuracy extrapolated for the ideal case of zero slice thickness (CT or MR slice thickness) to remove image localization related errors.

Today in the RSB lab the researchers have developed customized positioning frames with specific component attachments to perform craniotomies and biopsies (Figure 2-6 and Figure 2-7). Both of these procedures are incorporated into a graphical user interface, with the aim of presenting the technology as another tool available to the neurosurgeon; one where he or she can preplan a surgical procedure and fabricate his or her own patient-specific frames and surgical guiding attachments.

**Rapid prototyping and RPD Designer.** Rapid prototyping (RP) can be accomplished using a number of approaches. One such approach is 3-dimensional printing RP (Figure 2-8A and B), another is subtracting rapid prototyping (SRP) (Figure 2-8D). Both RP technologies provide a means to fabricate a physical 3-dimensional solid model from information contained in a stereolithography (STL) file. The file consists of planar triangular facets that represent a 3-

dimensional surface [29]. In the case of 3-dimensional RP, the first step in creating the solid model is the virtual slicing of the STL file by a preprocessing program [49]. For each virtual slice a layer is printed in real space. The bottom layer is built first, followed by additional layers until the last layer is built (Figure 2-8B). The RP system purchased in the RSB lab is built by ZCorp model 310 (Burlington, MA) and has a build accuracy of 0.3 mm [33]. The system creates the 3-dimensional model by translating a thin layer of powder from a reservoir location onto the building chamber. Subsequently, a binder fluid fuses the powder as specified by the slicing of the STL file. Afterwards, the build chamber moves vertically downwards allowing for a new layer of powder to be placed onto the previous layer, and as the binder fluid is placed again it will also glue within layers. When all layers are built the solid model is taken out of the building chamber (Figure 2-8C) and infiltrated with cyanoacrylate glue to assure durability [33]. The 3-dimensional solid, or in the case of this investigation the patient-specific frame, can be gas sterilized to be used within a sterile operative field [33].

The RSB lab purchase another machine to perform rapid prototyping, this machine is a programmable milling machine, and instead of performing 3-dimensional printing, it starts with a solid object and removes unwanted material (Figure 2-8D). Because it removes material, this type of rapid prototyping is called subtractive rapid prototyping (SRP). There are several reasons why the researchers invested in the model MDX-650 (Roland DG Corp., Knoxville TN); the main reasons are its speed and the capability of using a variety of materials to fabricate the reference guides. With the subtractive rapid prototyping machine the fabrication time was been cut in a third of the original time, from 11 hours to about 3 or 4 hours [34]. Also the reference frames created with this machine can be sterilized at high a temperature which is much faster than cold sterilization required by the patient-specific reference frames created with the 3-

dimensional RP machine. In addition, early accuracy tests demonstrate that the precision of the SRP machine is superior to the 3-D printing machine [34].

The creation of the STL file is conducted by a graphical user interface created in the RSB lab, called RPD designer [33]. The RPD designer has capabilities of rendering a solid model from a set of diagnostic images. The patient-specific frame is created by selecting a reference surface (called selected surface) by “painting” the surface of the virtual 3-dimensional rendered anatomical model [33] (Figure 1-1).

### **Significance**

There is a great potential for the new proposed idea of using diagnostic images and rapid prototyping to create a customized guiding frame for use in image-guided surgery. The most significant benefits of this new technology are rooted on the fact that it will eliminate the need for fixed frame application thereby reducing patient discomfort. It also has the ability to significantly reduce the cost of replacement parts related to frame-base stereotactic surgery. In addition, the use of the patient-specific reference frames will eliminate registration processes required by frameless stereotactic surgery and allow for reorganization of an overwhelmingly crowded OR. The new technology will provide the surgeon with the ability to plan and create his or her own surgical guides while reducing patient wait times during surgical planning. In addition, the surgeon will be able to remove and replace the patient-specific reference frame onto the patient as required, and maintaining high accuracy on a range of cranial procedures such as shunt placement, skin incision placement, bone removal during a craniotomy, biopsies, tumor resections and deep brain stimulation [34]. Besides making stereotactic neurosurgery more minimally invasive, the patient-specific reference frame could maintain frame-based accuracy [33]. Furthermore, the cost for creating a frame and a whole set of attachments to perform model

based image-guided surgery is estimated to be approximately \$50.00 per patient in materials cost [6].

Rajon et al. [34] has already created the software that provides the surgeon with the ability to directly build a virtual 3-dimensional model from diagnostic image datasets. This program allows selecting a surface on the virtual 3-dimensional model for the customized guiding frame and appropriately includes components to effectuate his or her approach towards a patient-specific intracranial surgery.

The significance of the present investigation is based of the fact that some level of testing is required prior to the fabrication of the customized guiding frame. The results of this testing will provide the clinician with prior information of frame-on-patient stability. In addition, it will allow the clinician to effectuate his surgical plan with more confidence and accuracy.

### **Facial Landmarks and Angles**

The stability of fit of the patient-specific frames (or masks) is greatly benefited by the surface characteristics of the human face. If a reference frame is to be designed based on the superficial surface of the human head, the contours of the human face serve the purpose of anchoring landmarks. The facial characteristics are ideal because of various neighboring irregular and curved surfaces. Besides, the facial contour is in close proximity to the brain, the skin is smooth and in most patients, close to the bony structure, to which the brain is naturally referenced. Therefore, it is important to obtain a basic understanding of the surface anatomy of the face. Figure 2-10 illustrates the facial anatomical landmarks of importance. On the forehead one can palpate the *frontal eminences*, which are prominences of the frontal bone that vary among individuals and are often unsymmetrical [10]. Caudal and medial to the frontal eminences is the *glabella*, a smooth somewhat triangular bony prominence on the frontal lobe located above the *nasion*, which is the point of intersection between the two nasal bones and the frontal bone.

The nasion represents the root of the nose. Lateral to the *glabella*, bilaterally, one finds the *superciliary arches*: two arched elevations of the frontal bone that tend to be more prominent on the medial aspect of the face. Some males have notably prominent superciliary arches that may significantly contribute to the stability of the mask. Superciliary arches tend to be small in females and absent in children. Caudal and lateral to the orbit, bilaterally, is the *zygomatic bone*, which forms the prominence, known commonly as the cheek bone. The prominence of the zygomatic bone can vary significantly among individuals. Finally, the *orbital area* is also an important area of depression that contains the eye within the bony skull [10]. Furthermore, based on these facial surface anatomy landmarks, one can extrapolate facial angles that are important to our discussion, as they also play an important role in determining the stability of the mask (Fig 2-11).

### **The Finite Element Method and ITK**

The patient-specific frames are complex in geometry and shape, and the best way to predict its behavior as it response to small external forces is by applying the principles of finite element analysis (FEA). The FEM involves dividing (discretizing) the entire frame into smaller parts or finite elements [5]. By dividing the entire frame into smaller elements, it is possible to obtain an accurate prediction of the displacement of the frame by approximating the displacement of each element to a polynomial function [28].

The patient-specific frames are modeled as rigid frames composed of linear tetrahedral elements under a deformable interface composed of truss elements (or linear springs) (Figure 5-2). The deformable layer, composed of truss elements, is attached at one end to the rigid layer, and on the other end all the truss elements are fixed (cannot moved in any direction x, y and z); this fixing of the elements on one end represent patient's surface.

In addition, FEM has been used extensively in medically related mechanical analyses and modeling [12], such as in orthopedics [26], dentistry [48], head injury [25] and organ analysis[39]; and to evaluate stresses in human bones [37], to mention a few.

For the present investigation, a linear 3-dimensional truss element was added to the local ITK FEM (ITK 1.8, Kitware Inc., Clifton Park, NY) library because it was not available. The ITK FEM module was created for image registration and has three iterative solvers to solve large systems of linear equations; these solvers are slow and not adapted for the cases in the present investigation. A new linear solver, Cholmod [13] was adapted which can solve sparse systems of equations in seconds compared to hours that the available ITK's linear solvers take. Also, the ITK library was carefully studied and manipulated to make the methodology defined in this work progress as fast as possible (Appendix A). The ITK FEM module was chosen for this assignment to provide compatibility to the already built and working graphical user interface (RPD designer).

### **Elements Used in the Simulation**

Two simple elements were used for this investigation. The first one is a 2-node truss element in 3-dimensional space called space truss. The second one is the linear 4-node solid tetrahedral element in 2-dimensional space, which was available in the ITK FEM module.

#### **The space truss**

Space trusses are frequently used to model lattice domes and aerospace structures [4]. They compose 3-dimensional structures that are subjected to 3-dimensional force systems. A space truss element is a long, thin and straight prismatic element. Prismatic means that its cross sections are all homogeneous by having a cross sectional area ( $A$ ) and an elastic modulus ( $E$ ) that remains constant through out the length of the truss. Space trusses are connected by nodes that act as frictionless ball-and-socket joints [17]. In a structure composed of space trusses, any

unsupported node (with no assigned boundary conditions) will result in translations in three local directions (x, y, and z). If no boundary conditions are applied to its nodes, then each truss element has six node displacements or six degrees of freedom (DOF) to establish its deformed position [4] (Figure 2-12). A space truss element is defined by the Young's modulus (E), cross sectional area (A), the length (L), and a Poisson's ratio ( $\nu$ ).

One important characteristic of the any truss element is that it has a preferred dimension, that is, along its longitudinal or axial direction (Figure 2-12). By definition, a truss element will only develop axial forces [17]. Any perpendicular forces will not change its original length (L), since the truss element does not undergo moments and its nodes act like frictionless ball-and-socket joints. For example, Figure 2-13 shows a perpendicular force ( $f_y$ ) applied to a truss element; as a result of the force there is no difference between the original length (L) and the length succeeding the application of the force (L'). Hence, if there are not differences in lengths ( $L' - L = 0$ ), there were no internal forces and no displacements either (Figure 2-13).

The space truss is considered a simple element since it deforms only along one direction (along its local x-axis) [5]. For simple elements like trusses, the direct stiffness method can be use to determine the elements stiffness matrix ( $\mathbf{k}^e$ ). The direct method uses principles of equilibrium and mechanics of materials [46] to define the element stiffness matrix, which is a relation between node displacements ( $u_1$  and  $u_2$ ) and internal forces ( $f_1$  and  $f_2$ ) for each element  $e$  (Figure 2-12).

The characteristic of the space truss element of only responding to axial forces makes the calculation of the element stiffness matrix relatively easy. When the element is analyzed in its local coordinate system, by definition there are no internal forces perpendicular to the truss and hence no perpendicular displacements. In other words, the displacement vector for a truss

element is given by Equation 2-1, and the local node displacements  $u_1$  and  $u_2$  are caused by the local node forces  $f_1$  and  $f_2$ , as seen in Figure 2-14.

$$\mathbf{u} = \begin{bmatrix} u_1 \\ u_2 \end{bmatrix} \quad (2-1)$$

From mechanics of materials [46], the relationship between the local node displacements and the local node forces for a prismatic truss element is linear and given by Hooke's Law [46], or Equation 2-2, where  $k$  is the stiffness coefficient and is equal to  $AE/L$ .

$$f = ku \quad (2-2)$$

With Equation 2-2 and the principles of equilibrium [28], the element stiffness matrix ( $\mathbf{k}^e$ ) for a particular element  $e$  can be calculated. As Figure 2-14A shows, to establish the element stiffness matrix with the direct stiffness method [28], one needs to confine the element to a unit displacement at node 1 ( $u_1$ ) and hold node 2 ( $u_2$ ) fixed. The force at node 1 is equal to  $k \cdot 1$  (by Equation 2-2). Since the element is in equilibrium, then the internal force at node 2 must be equal to  $-k \cdot 1$ . A similar situation is true (Figure 2-14B) when node 2 is confined to a unit displacement, and the internal forces at node 2 and node 1 are equal to  $k$  and  $-k$ , respectively. The element stiffness matrix is a  $2 \times 2$  matrix defined in local coordinates by Equation 2-2.

$$\mathbf{k}^e = \begin{bmatrix} k & -k \\ -k & k \end{bmatrix} \text{ or } \mathbf{k}^e = \frac{AE}{L} \begin{bmatrix} 1 & -1 \\ -1 & 1 \end{bmatrix} \quad (2-3)$$

For the stiffness coefficients  $k_{ij}$  the first subscript identifies the direction of the force, while the second subscript is related to the displacement. The element stiffness matrix represents the forces at the ends of the element as functions of the displacements at the nodes (Equation 2-4).

$$\begin{Bmatrix} f_1 \\ f_2 \end{Bmatrix} = \frac{AE}{L} \begin{bmatrix} 1 & -1 \\ -1 & 1 \end{bmatrix} \begin{Bmatrix} u_1 \\ u_2 \end{Bmatrix} \text{ or } \begin{Bmatrix} f_1 \\ f_2 \end{Bmatrix} = \mathbf{k}^e \begin{Bmatrix} u_1 \\ u_2 \end{Bmatrix} \quad (2-4)$$

The element stiffness matrix (Equation 2-4) defines the space truss in local coordinates.

The transformation to global coordinates is necessary to represent the truss element as part of a entire structure. The transformation matrix and is represented by Equation 2-5.

$$\mathbf{T} = \begin{bmatrix} \cos \theta_x & \cos \theta_y & \cos \theta_z & 0 & 0 & 0 \\ 0 & 0 & 0 & \cos \theta_x & \cos \theta_y & \cos \theta_z \end{bmatrix} \quad (2-5)$$

Finally, for one element the local element stiffness matrix  $\mathbf{k}^e$  can be transformed into the global element's stiffness matrix  $\mathbf{K}^e$  by Equation 2-6 ( $^T$  means the transform of the matrix).

$$\mathbf{K}^e = \mathbf{T}^T \mathbf{k}^e \mathbf{T} \quad (2-6)$$

For the space truss element, the element's stiffness matrix in global coordinates  $\mathbf{K}^e$  results in a 6 x 6 matrix (Equation 2-7).

$$\mathbf{K}^e = \frac{AE}{L} \begin{bmatrix} \cos^2 \theta_x & \cos \theta_x \cos \theta_y & \cos \theta_x \cos \theta_z & -\cos^2 \theta_x & -\cos \theta_x \cos \theta_y & -\cos \theta_x \cos \theta_z \\ & \cos^2 \theta_y & \cos \theta_y \cos \theta_z & -\cos \theta_x \cos \theta_y & -\cos^2 \theta_y & -\cos \theta_y \cos \theta_z \\ & & \cos^2 \theta_z & -\cos \theta_x \cos \theta_z & -\cos \theta_y \cos \theta_z & -\cos^2 \theta_z \\ & & & \cos^2 \theta_x & \cos \theta_x \cos \theta_y & \cos \theta_x \cos \theta_z \\ & \text{Symm.} & & & \cos^2 \theta_y & \cos \theta_y \cos \theta_z \\ & & & & & \cos^2 \theta_z \end{bmatrix} \quad (2-7)$$

Following the direct stiffness method, the most important steps to define the space truss element systematically is first to define the element's stiffness matrix in local coordinates (Equation 2-3); then to calculate the transformation matrix  $\mathbf{T}$  (Equation 2-5) necessary to swap from local to global coordinates; and finally it is important to define the element stiffness matrix in global coordinates  $\mathbf{K}^e$  (Equation 2-7).

In the FEM, all elements stiffness matrices in global coordinates ( $\mathbf{K}^e$  for  $e = 1$  to  $n$ ,  $n$  is the number of elements) are assembled into a global stiffness matrix  $\mathbf{K}_g$  that represents the force-displacement relations for an entire structure composed, in this case, of space trusses.  $\mathbf{F}_g$  is a vector that that defines the external forces in global coordinates and  $\mathbf{U}_g$  is the resulting node

displacements in global coordinates (Equation 2-8). The solution to the system of linear equation is given by solving for the displacements in global coordinates,  $\mathbf{U}_g$ .

$$\mathbf{F}_g = \mathbf{K}_g \mathbf{U}_g \quad (2-8)$$

### The linear tetrahedron

Solid elements are defined in 3-dimensions and can model a solid body. The linear tetrahedron is the simplest solid element in 3-dimensional space; four coordinate points define its geometry with respect to a global coordinate system. It is known to be poor for stress analysis, as results tend to be more rigid than expected [17]. The numbering of the nodes is important for generating every individual tetrahedron correctly.

The numbering of the tetrahedron's nodes must be done following the right-hand rule (Figure 2-14) and the calculation of the tetrahedron's volume must result in a positive value (Equation 2-9). First an initial corner is picked (node 0) and then the triangular face opposite to the initial corner must be numbered following a counterclockwise manner (nodes 1, 2 and 3). The calculation of the tetrahedron's volume gives evidence that the numbering of the nodes is done correctly. In Equation 2-9, the node coordinates for the tetrahedron are given by  $x_i$ ,  $y_i$ , and  $z_i$  where  $i$  is the node number.

$$Volume = \frac{1}{6} \det \begin{bmatrix} 1 & 1 & 1 & 1 \\ x_0 & x_1 & x_2 & x_3 \\ y_0 & y_1 & y_2 & y_3 \\ z_0 & z_1 & z_2 & z_3 \end{bmatrix} > 0 \quad (2-9)$$

The derivation of the tetrahedral element's stiffness matrix is complicated, in fact it rarely derived using the direct stiffness method. In turn, the principles of virtual work are often used to derive stiffness matrices for solid elements, multi-dimensional elements [4].

## Characteristics of Stiffness Matrices

The characteristics of stiffness serve to validate the setup of the ITK FEM module for the two types of elements used in this investigation. The characteristic of the element stiffness matrices for the space truss, the linear tetrahedral element and the global stiffness matrix ( $\mathbf{K}_g$ ) were analyzed for validation of the results.

The element stiffness matrix can be singular; this means that the determinant is equal to zero. Also they need to be squared and symmetric and all element along the diagonal need to be greater or equal to zero [28]. In the case of the reduced form of the global stiffness matrix, it must be square, symmetric and positive definite and all its diagonal values have to be greater than zero [28]. In addition it must have an inverse so the displacement can be solved uniquely for a given force [46].

Positive definite matrices arise frequently in FEM problems. They are characterized by the condition that all their eigenvalues are positive [13]. One of the properties of a positive definite matrix is that it can be decomposed by Cholesky decomposition. If A is a symmetric positive definite matrix, then A can be factored into a product of L and  $L^T$  ( $T$  means the transpose of a matrix), where L is a lower triangular matrix with positive diagonal elements. The definition of a positive definite matrix is given by Equation 2-10, where X is any vector in R space [13].

$$X^T A X > 0 \quad (2-10)$$

## Linear Solvers

The ITK FEM library is fitted to solve image registration problems that incorporate finite elements. The ITK FEM module offers iterative solvers mainly used to solve very large matrices, common to image registration problems. The most reliable iterative solver in the module is the ItPack Solver [24], however due to its iterative nature ItPack is a very slow solver. An alternative to using ItPack is a solver based on Cholesky decomposition called Cholmod [13].

Cholmod is a set of routines for factoring sparse symmetric positive definite matrices and solving linear equations used in Matlab (The Mathworks Inc. Natick, MA). Cholmod proved to be much faster and highly reliable; as a result it was adapted to be used with the ITK FEM module.



Figure 2-1. Pre-target localization and pre-surgical planning is done in a computer workstation.



Figure 2-2. Procedures related to frame-based image guidance surgery. A) A patient with a head ring prior to scanning on a CT. B) A surgeon setting the coordinates on a stereotactic apparatus, which will be mounted onto a head ring (reference frame) to located the coordinates for targeting a specific location on the brain.

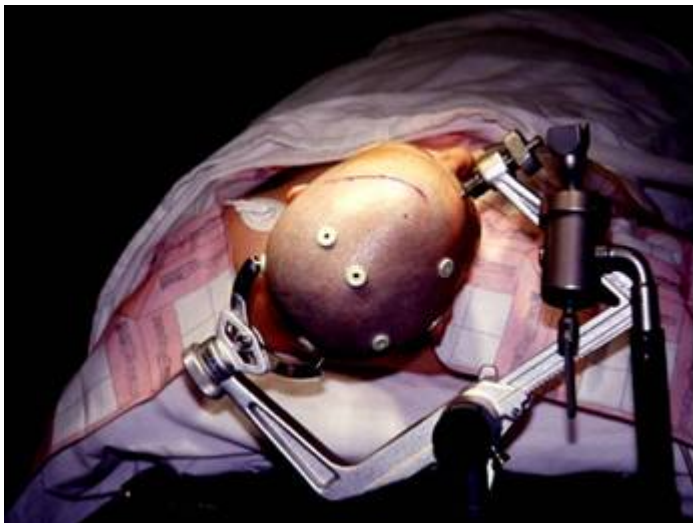


Figure 2-3. Frameless stereotactic surgery uses fiducials that are glued to the patient's skin. The fiducials serve for registering the patient's anatomy in real space to the image datasets on a computer workstation. The tools for the surgery have similar fiducials so they can be tracked by cameras.



Figure 2-4. Typical layout when frameless stereotactic surgery is employed. Both images show how crowded the OR can get by the necessity of additional computer workstations and tracking devices.

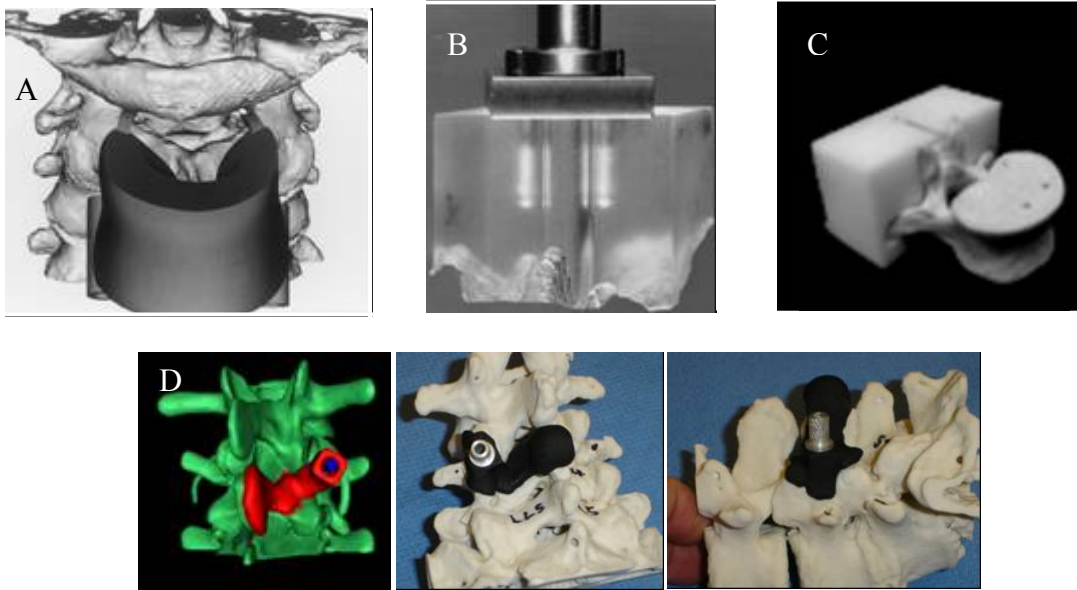


Figure 2-5. Template designs for the spine. A) Goffin [20], B) Birnbaum [6], C) and Yoo [50]. D) The RSB template designs from the first stages on the development of customized positioning frames.

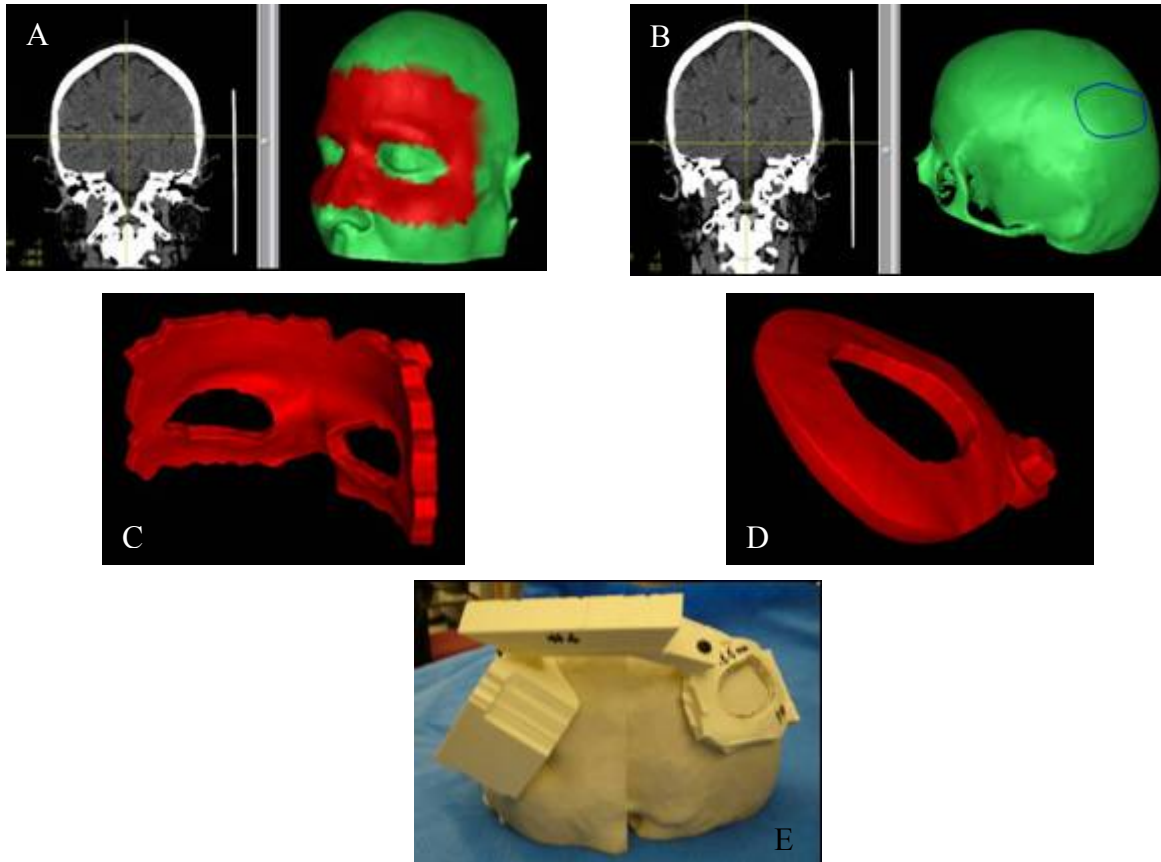


Figure 2-6. Router guides for craniotomy. A) Selection of the customized positioning frame onto the patient's virtual 3D model. B) Selection of craniotomy contour drawn on the surface of the skull. C) Virtual model of the customized positioning frame. D) Craniotomy attachment for the customized positioning frame. E) Fabricated structure that will guide the surgeon to perform the craniotomy as planned [34]

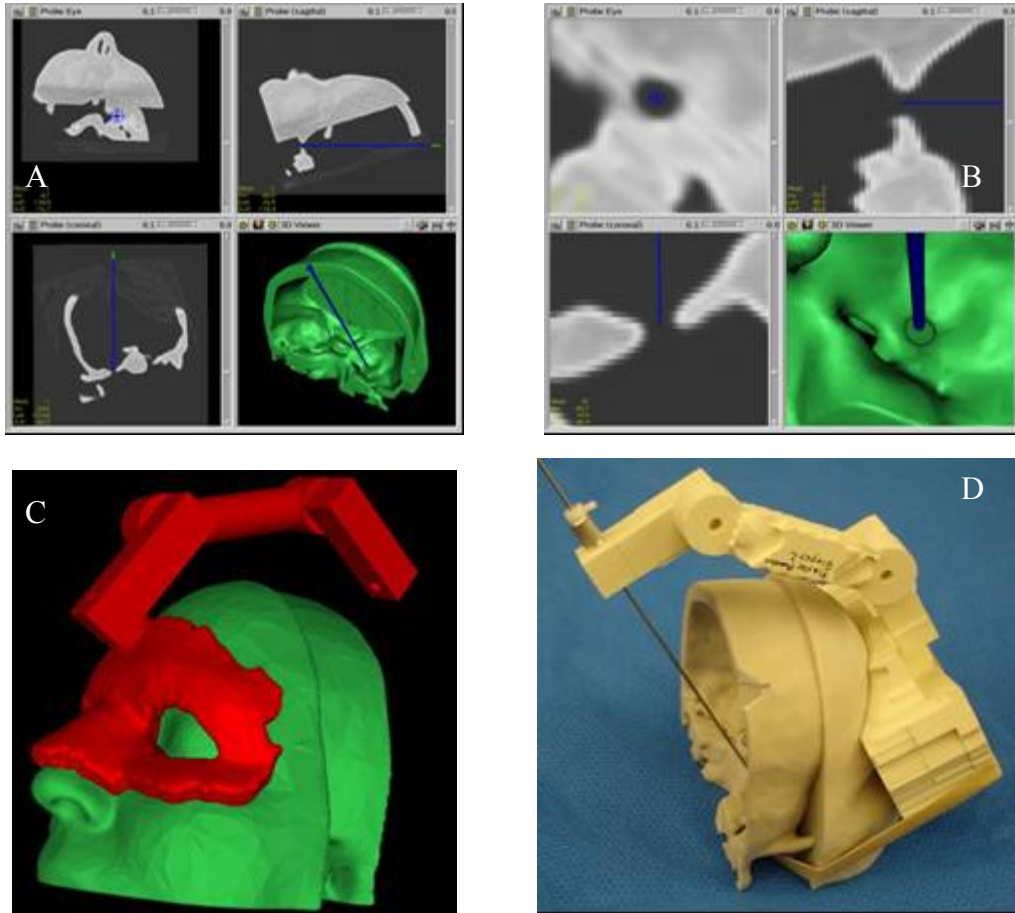


Figure 2-7. Biopsy guides. A and B) Graphical user interface shows the three orthogonal views from diagnostic images and the solid virtual model. The surgeon can select the target location and the graphical user interface will appropriately position the biopsy guide. C) Virtual model of the customized positioning frame and the biopsy guide attachment. D) Fabricated structure that will guide the surgeon to perform the biopsy as planned [34].



Figure 2-8. Rapid prototyping machines. A) Rapid prototyping machine by ZCorp model 310. B) A thin layer of powder is moved to the building chamber by the gantry, which also holds the print head that distributes the binder fluid. C) The 3D model as removed from the building chamber. D) Subtractive RP machine.

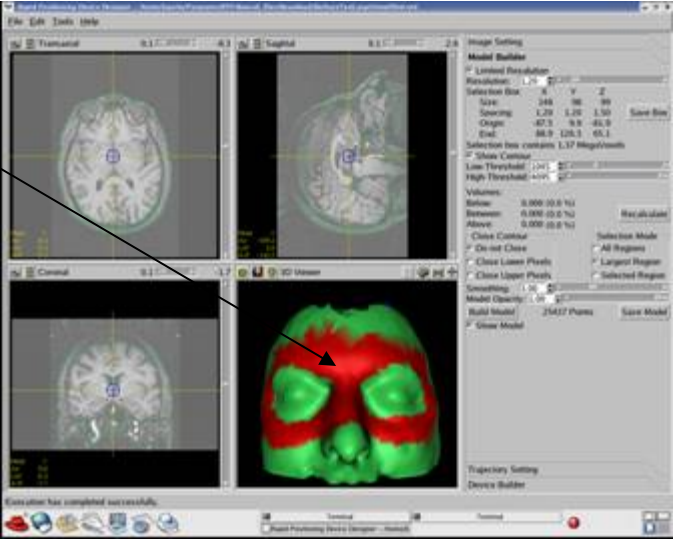
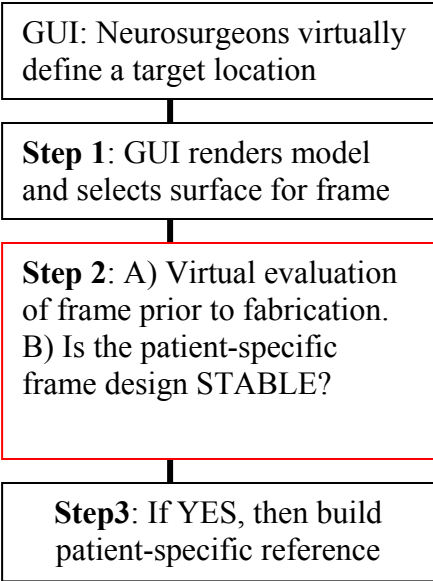


Figure 2-9. Chart to visualize the significance of the present work.

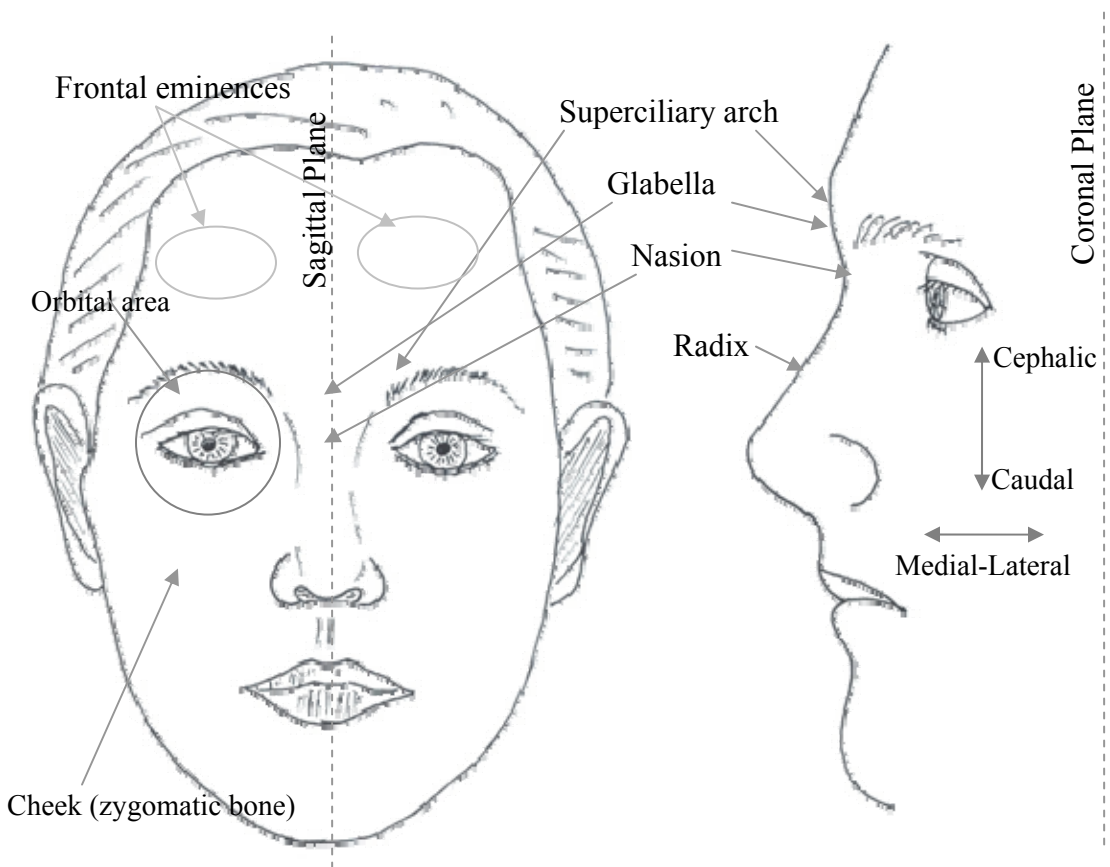


Figure 2-10. Facial landmarks.

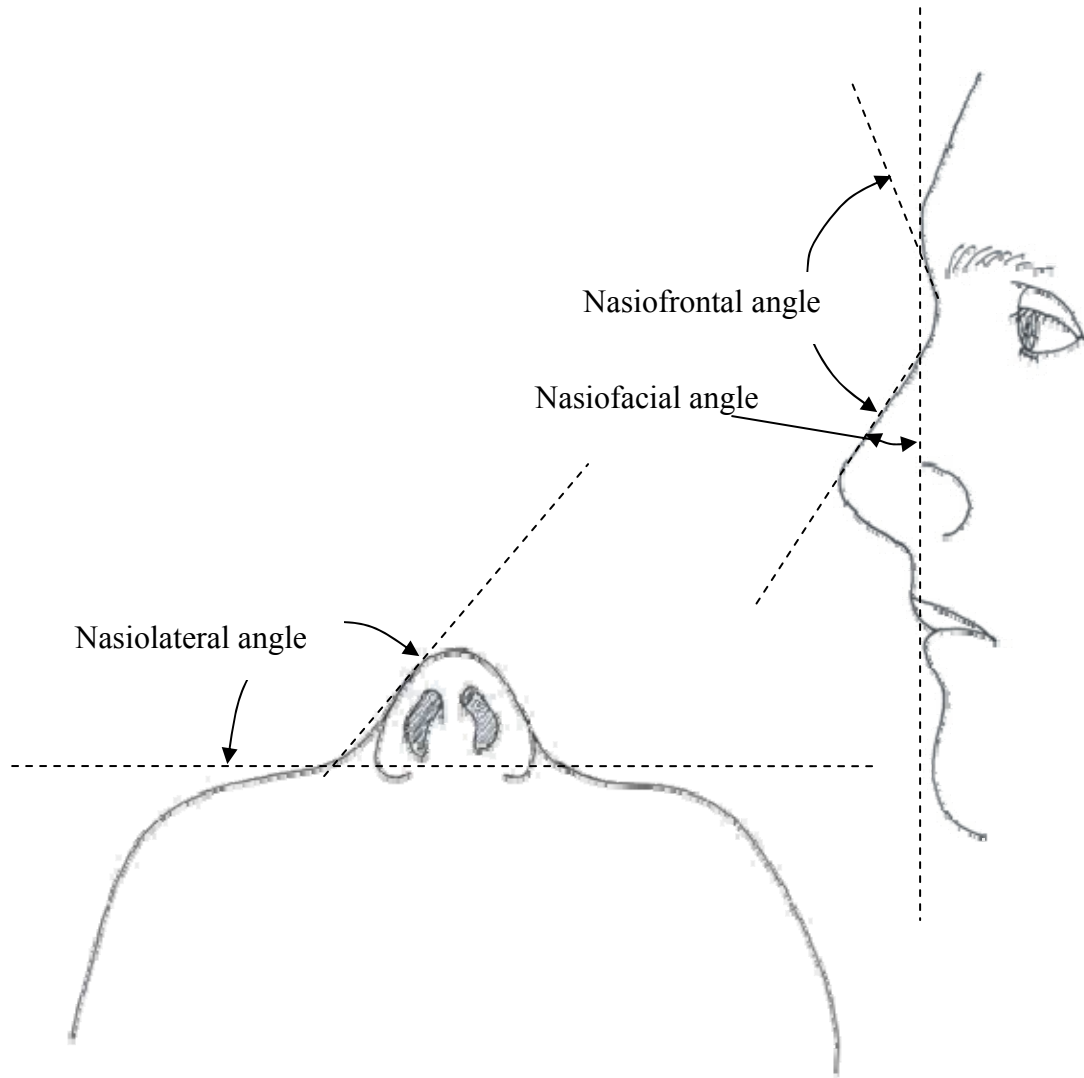


Figure 2-11. Facial angles [10]. The nasiolateral angle is calculated at the level of the radix.

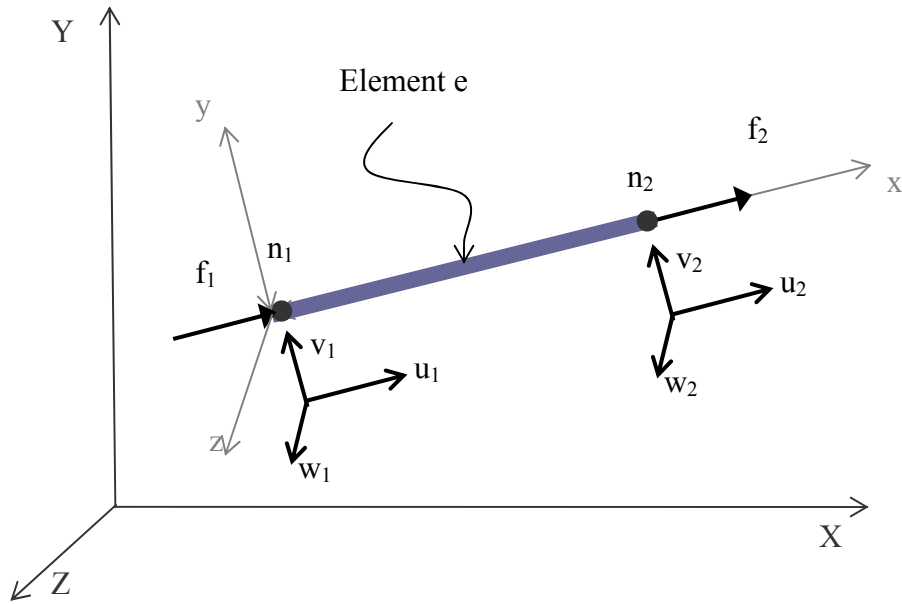


Figure 2-12. Space truss element has six displacements to establish its deformed position. There are  $u_1$  and  $u_2$  along its x-axis,  $v_1$  and  $v_2$  along its y-axis and  $w_1$  and  $w_2$  along its z-axis. Though the space truss is defined in 3-dimensional space, it will only develop axial forces, along its local x-axis.

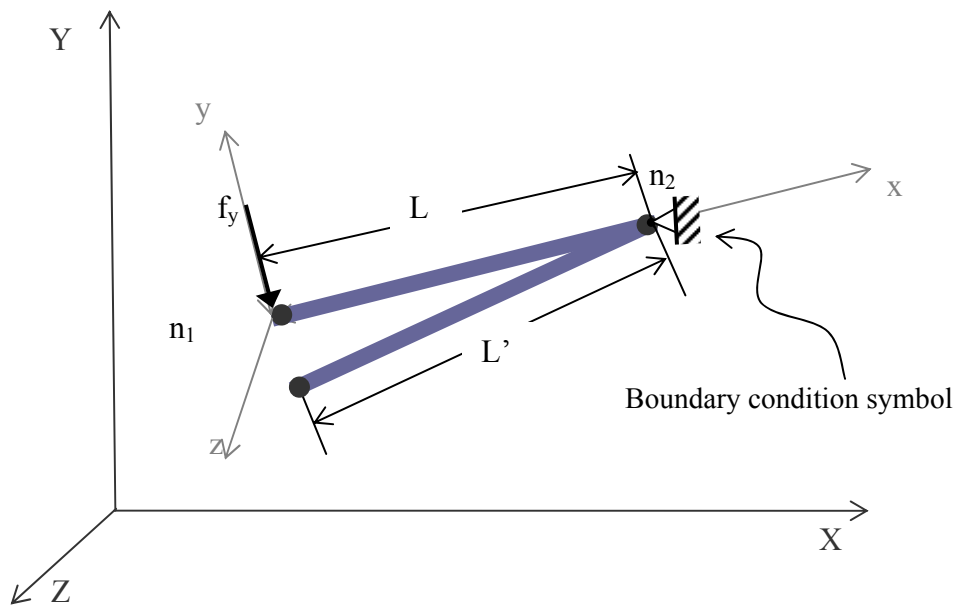


Figure 2-13. Application of a force perpendicular to the axis of the space truss. There is no change in length ( $L' - L = 0$ ) and there are no internal forces (in a real simulation the truss element will not display as in the figure). The boundary condition symbol implies, in this case, that the element is fixed in local x and z directions.

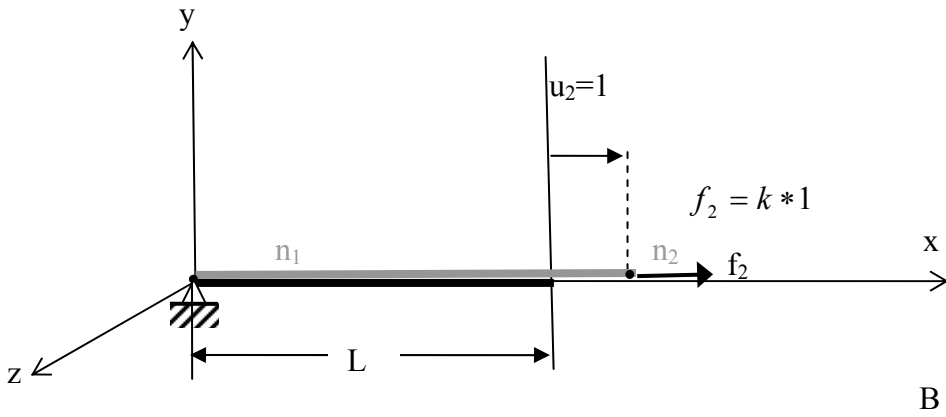
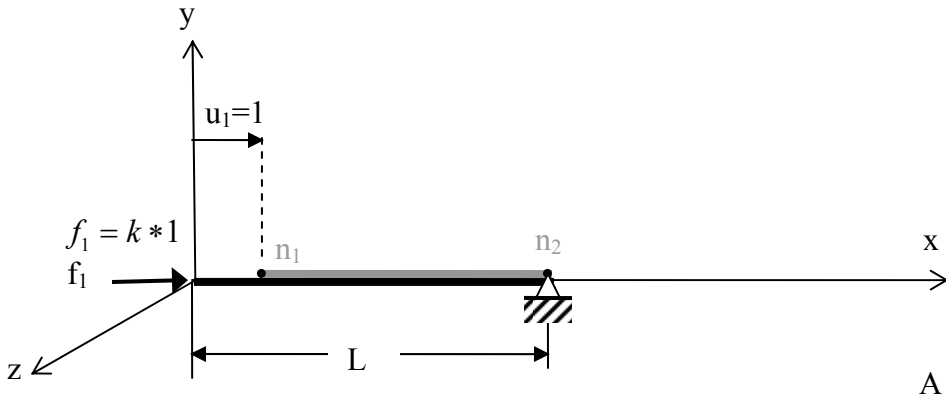


Figure 2-14. Space truss in local coordinates. A truss element in its original position is denoted by the thick black line, and the same truss element in a deformed state is shown in gray. After a force  $f_1$  is applied to node 1 ( $n_1$ ) to create a unit displacement the stiffness coefficient  $k_{11}$  defined the element at  $n_2$ . The reaction force at  $n_2$  is  $k_{12}$ . Similarly, a force corresponding to a unit displacement is applied at  $n_2$  and  $k_{21}$  and  $k_{22}$  are defined.

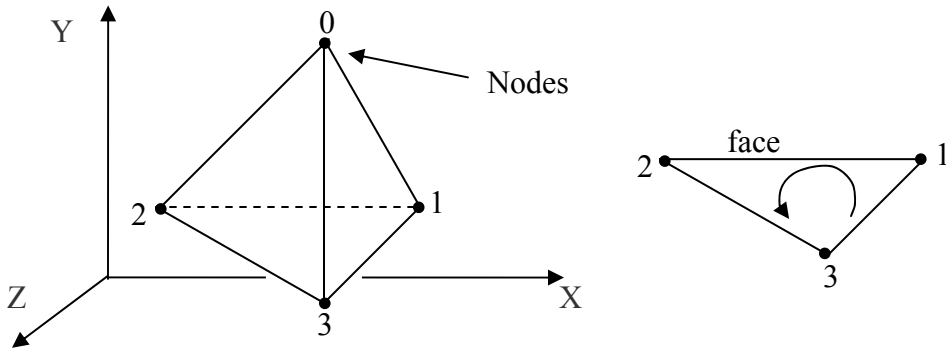


Figure 2-15. The linear tetrahedron has a unique numbering scheme.

## CHAPTER 3 MATERIALS

Three patients with notably dissimilar face profiles were selected as training data for the methodology designed to test uniqueness of fit. With CT datasets and the graphical user interface, RPD designer, three anatomical solid models (Figure 3-1) were built and name Caucasian, Asian and infant because they belonged to a Caucasian male, an Asian male and a infant respectively. Also six masks were built, two for each model (Figure 3-2). For each solid model, a conforming small and a large mask were built; the small masks included considerably less facial landmarks than the large masks. While the large masks included the entire orbital area and extended laterally and medially along the superciliary arches, the small mask only included the upper orbital region and extended to the level of the glabella along the nose region. All masks were created from the “painting” of the corresponding selected surface as shown in Figure 5-1. The six masks designed with RPD designer are the training data for the methodology to test stability and uniqueness of fit.

In reality when the patient specific reference frames are applied onto a patient, the clinician will apply a force to keep the mask in their unique location. Sliding, rotation and translation of the mask on the level of contact with the patient’s face signifies exaggerated displacements at the level of the attachment tips, as shown in Figure 1-1D. While the large mask designed for training the methodology maintain their location when exposed to real transverse forces, the small mask would not withstand normal forces at their extremities, along the length of the superciliary arches. To provide with a real world measure of stability for the small and large masks, a center pin was placed normal to the surface (or the direction on which the mask is placed onto the solid model) and at the location of the glabella on all masks. Oriented by the center pin, crosshairs were drawn on all masks along the transverse and sagittal planes as shown in Figure

3.5. Additional pins were located close to ends of the crosshairs lines as shown in Figure 3-5 and numbered from 1 through 4. Pins 1 and 3 were placed on the sagittal plane and pins 2 and 4 were placed on the transverse plane (Figure 3-6). A normal force of 5 N, applied by weight, was applied onto all pins for large and small masks (Figure 3-7). The large masks remain in their unique location, and sustained the 5N force; on the other hand, the small mask exhibit large displacement when the force was applied on pins 2 and 4. This resulting slippage behavior is mainly attributed to the smaller surface area and less facial irregularities covered by the small masks. All small masks withstood the 5N normal force on pins 1 and 3.

In addition, the placement of all large masks is unique, this is not the case for the small masks; there is not clear unique location where the masks fit. The sliding of all small masks when experiencing a normal force on pins 2 and 4 and the lack of a clear unique fit are evidence that the small masks are unstable, on the contrary all large masks withstood the 5N force on all pins and have a unique fit, which characterize them as stable (the fitting of the masks onto the models can be seen in Chapter 6, Figures 6-1 through 6-3).

In addition to the masks, two other surfaces were created to evaluate the methodology of fit. A cap-like reference frame (Figure 3-3) was created from CT image dataset and a half-sphere surface (Figure 3-4) was virtually created with Paraview (Paraview 1.6, Kitware Inc., Clifton Park, NY). The cap frame covers the top of the head and extends orthogonally along the coronal and sagittal planes no further than at the level of the frontal eminences. The half sphere surface is a faceted surface defined by 31 points evenly distributed (Figure 3-4). The half sphere needed to be defined as a faceted surface with ten angular rotation about its axis and three coplanar levels, because a smoother surface could not be evaluated, since it results in a mechanically underconstrained system.

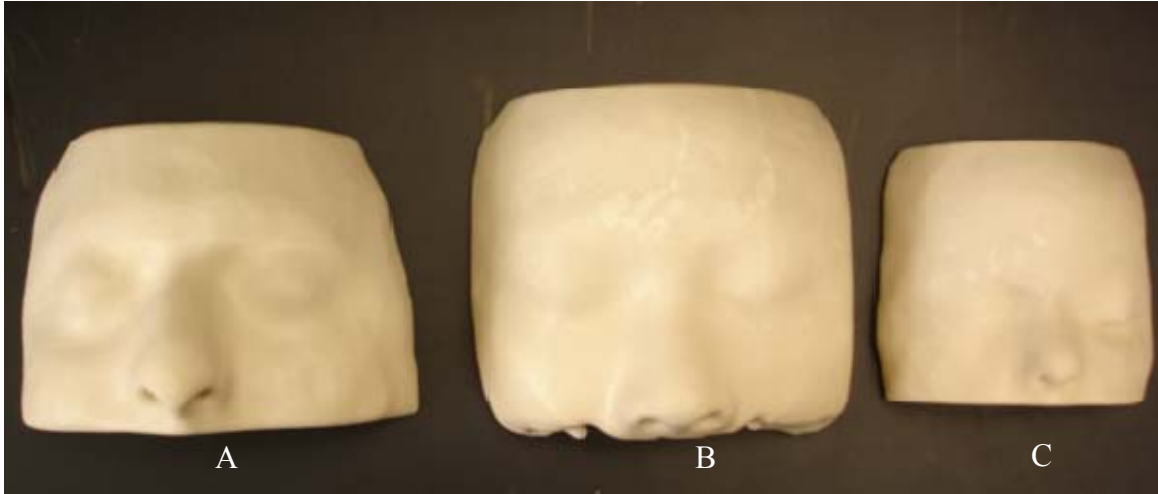


Figure 3-1. The three models used to evaluate the methodology for testing unique fit. A) Caucasian, B) Asian and C) infant.



Figure 3-2. Masks built for testing the methodology of fit. A) Caucasian small and large masks. B) Asian small and large masks. C) Infant small and large masks.

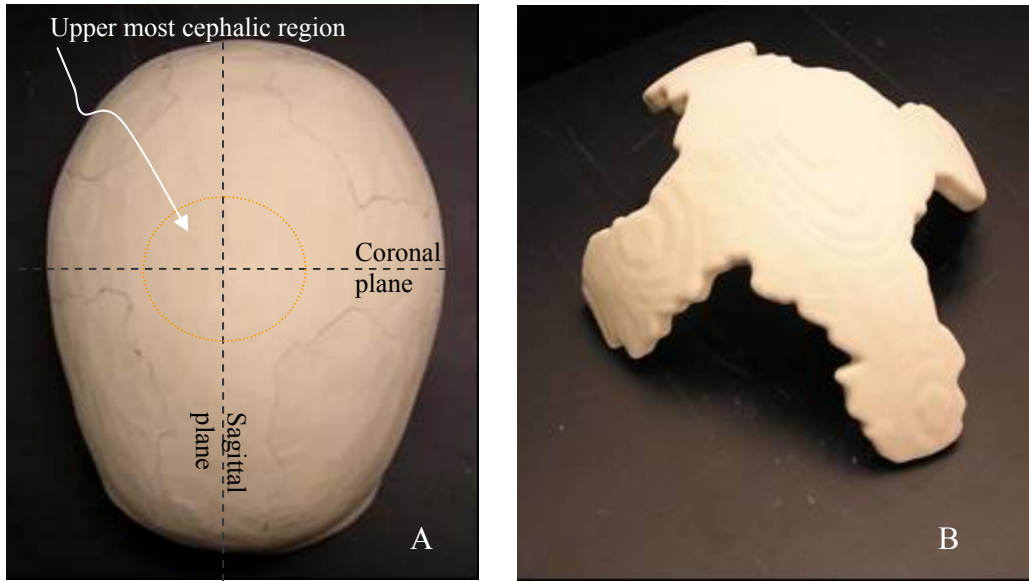


Figure 3-3. Cap-like reference frame. A) Upper head model and B) cap-like frame.

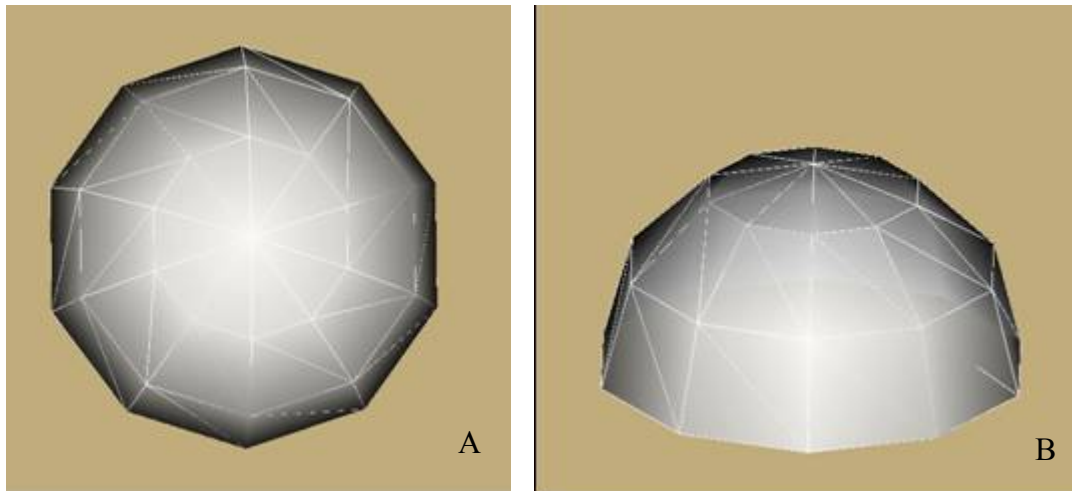


Figure 3-4. Virtually created half sphere test model. A) Top view and B) side view.

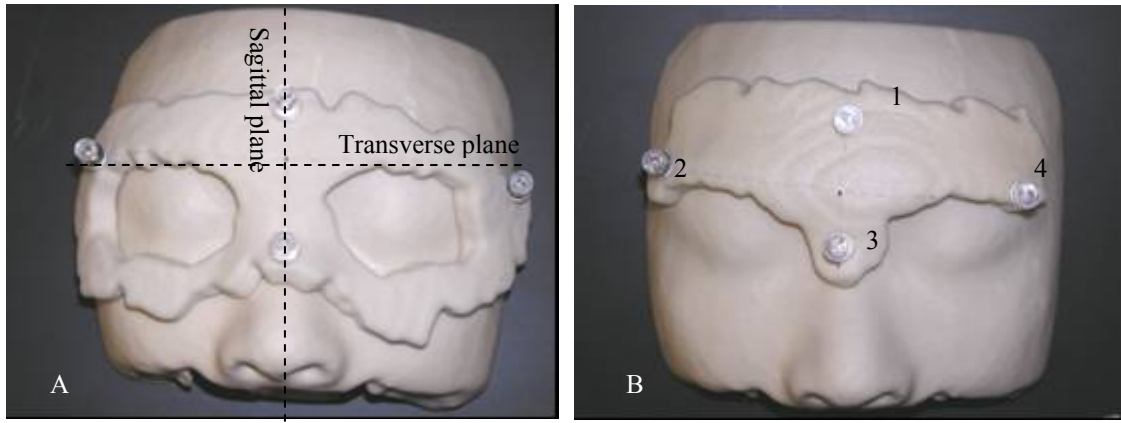


Figure 3-5. Placement of pins for a simple test on the real stability of the large and small masks.  
 A) Large Asian mask and B) small Asian mask.

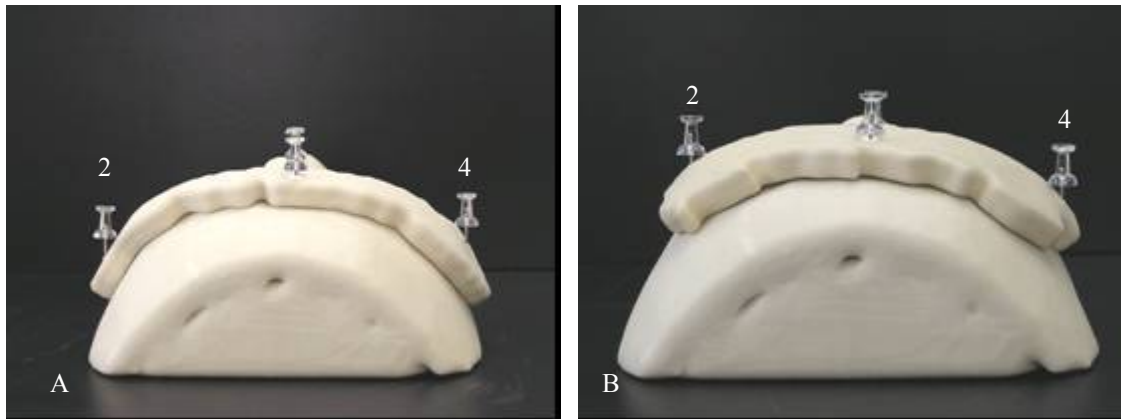


Figure 3-6. Coronal view of placement of the pins onto the real masks. Notice the orientation of pins 2 and 4 and difference in lateral extend between the A) large Asian mask and B) the small Asian mask.

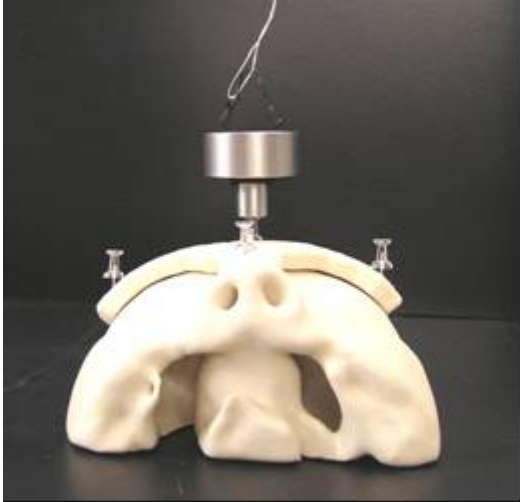


Figure 3-7. The method employed to demonstrate the difference in stability between the large and small masks. The weight represents a 5N force, and it is placed onto a pin to observe the resulting displacement of the small Asian mask.

## CHAPTER 4 METHODOLOGY FOR MEASURING STABILITY

### **Introduction**

The methodology for testing stability of fit of the patient-specific frames relies on the use of the finite element method (FEM) to model the contact interactions between the patient-specific frame and the patient's facial contour. The objective of the methodology is to produce a score value that correlates with the physical stability of the six masks created. The methodology quantifies the stability of fit by information from the simulated movement of the patient-specific frame as it responds to small external forces. The virtual mask is able to experience displacements because it is modeled as a rigid solid surface, which is virtually placed on top of a deformable bed of springs (Figure 4-1), and loaded by small external forces. The small external forces are calculated to cause a spring deflection of 1%, because the simulation does not include friction. For every small external force applied onto the rigid layer, internal forces transfer onto the bed of springs, and by the deformation of the springs, the rigid layer can either move closer to the model in some areas and move away in other areas and still sustain contact; or it can predominantly slide or rotate (Figure 4-2). Sliding and rotation occur when there is relative motion between the two surfaces. The simulated movement of the mask is analogous to testing the fit of a cast by placing it over its mold and applying pressure at various locations to see if it fits securely. In a similar way, the approach used in this investigation involves applying small forces in many directions and locations and monitoring the resulting motion of the mask (cast).

As described in the materials section, three solid life-like facial models that represent three different patient's anatomies were constructed with 3-dimensional printing rapid prototyping. For each solid model two masks were designed with the existing user interface RPD designer, one of the masks is known to be stable and the other is known to be unstable (from information

on Chapter 3). The stability information on the real masks was used as training data for the methodology designed in this investigation.

The methodology designed to test stability of the patient-specific reference frames is presented in four sections; a) system components and FEM setup, b) program parameters, and c) output parameters, and d) the criteria defined to measure stability of fit of the patient-specific reference frames. As mentioned before, the task of measuring stability is critical to understanding the appropriateness of the reference surface selected and thereby appreciating the predicted accuracy and precision of the clinically designated patient-specific design. While this is only a piece of a much broader investigation that seeks to evaluate an alternative method to image-guided surgery, it is critical to this application of patient-specific tool design.

### **System Components and FEM Setup**

The system components are the external forces, the rigid layer (virtual mask or frame), the bed of springs, and the boundary conditions; all are defined in the context of FEM. The STL file, output of the graphical user interface (RPDdesigner), is the only input into the system. The STL file is standard format representation of a 3-dimensional surface as an assembly of planar triangles (Figure 4-3) [29], the point coordinate information of the vertices of each triangle are used to define the rigid layer, the bed of springs and the boundary conditions.

The first component of the FEM setup is a rigid layer and it is composed of tetrahedral finite elements. This layer is virtually constructed between the selected surface and a surface extrapolated along the positive normal direction at each vertex (Figure 4-1 and 4-3). The second component of the system is a bed of springs composed of individual linear springs that are placed between the selected surface and another surface extrapolated along the normal negative direction of each vertex (Figure 4-1). Hence, each individual spring in the bed of springs is constructed between the point coordinates of the selected surface and the boundary condition

points (or nodes). On the whole, the rigid layer represents the patient-specific reference frame (or mask), and the boundary conditions represent the patient's facial surface. With the stimulation of external forces, the bed of springs will allow for the virtual displacement of the rigid layer, simulating the stability or instability of the real mask onto the patient's facial anatomy.

### **External Forces**

The external force direction is defined with respect to a main normal ( $\mathbf{N}_{\text{main}}$ ).  $\mathbf{N}_{\text{main}}$  is a normal perpendicular to the coronal plane and along the sagittal plane of the skull; in other words, in the direction in which the frame will be placed onto the model (Figure 4-4). The angle theta ( $\theta$ ) is the tilt angle from  $\mathbf{N}_{\text{main}}$  and  $\rho$  is the spin angle about  $\mathbf{N}_{\text{main}}$ . The forty nine forces are calculated by incrementing theta ( $\theta$ ) six times, from  $0^\circ$  to  $90^\circ$  in intervals of  $15^\circ$ ; and by rotating the angle  $\rho$  (spin) by eight forces vectors in increments of  $45^\circ$  about the  $\mathbf{N}_{\text{main}}$  (six tilt angles multiplied by eight spin angles plus one normal forces is equal to forty nine forces vectors). All forty nine forces are applied onto every node of the mask with the exception of the edge nodes (Figure 4-5). The force magnitude is very small enough to displace a single spring by 1% and will be discussed in the program parameters section. For example, in a case of a mask similar to the one shown in Figure 4-5, which is composed of about 300 nodes, 49 force vectors will be placed on each node, that will result in 14700 forces applied onto the entire mask. For each of the 14700 force vectors, all 300 springs will have a resulting displacement.

### **Rigid Layer**

Probably the most important characteristic of the system is the difference in strength (elastic modulus) between the linear springs, which compose the bed of springs, and the rigid layer. The rigid layer in comparison to the bed of springs must be rigid in the sense that it can

translate or rotate but not deform. The rigid layer is composed entirely of four node tetrahedral elements. From the extrapolation of the point coordinates that define the planar triangles in the STL file, virtual wedges are built. In each wedge three tetrahedral elements are fitted (Figure 4-6), and created following the right-hand-rule as explained in Figure 2-15. In order to define a four node linear tetrahedron in ITKFEM module [24], four point coordinates are need, and two mechanical properties, the modulus of elasticity (E) and a Poisson ratio ( $\nu$ ).

**RDR ratio.** It is important to measure if the rigid characteristic of the rigid layer are maintained at every force application; for that purpose a program flag was created and called RDR ratio. The RDR ratio is an indicative of major deformations of the rigid layer. The RDR is calculated with respect to the upper surface of the rigid layer and for each external force application because every external force application has the potential of deforming the rigid layer. To calculate the RDR the maximum difference in distance between a vertex (node)  $i$  and its neighboring vertices before ( $L_a$ ) and after ( $L_b$ ) the application of a force is measured and called maximum rigidity fault ( $mrf_i$ ) (Figure 4-7). As Equation 4-1 shows, the RDR is the ratio of the maximum rigidity fault ( $mrf$ ) at a vertex  $i$  divided by the sum of the displacement magnitude ( $d_i$ ) and the  $mrf_i$ .

$$RDR_i = \frac{mrf_i}{mrf_i + d_i} \quad (4-1)$$

If RDR is close to zero (or one over a small displacement), it means that the rigid layer has not deformed. If the RDR ratio is close to one, the rigid layer has taken the entire load and it has deformed at a particular node. In the situation where the rigid layer deforms, the RDR ratio will indicate so and the simulation will not be able to provide reliable results. In the simulation, if the RDR ratio exceeds 0.05 (or 5% rigidity loss) then the force was not included in the results. For

all the masks and frames evaluated, the RDR ratio had a mean of 0.3% and a standard deviation of 0.2%.

### **Bed of Springs**

The bed of springs is the only deformable component of the system given that the individual springs that comprise it considerably are less strong than the rigid layer. The purpose creating a bed of springs is to identify and monitor the individual springs that acquire a state of tension or compression. A linear spring has a characteristic spring stiffness referred to as the spring constant  $k$  [46]; it is related to the strength of the material of what the spring is made of. In addition, the spring has a natural length ( $L_0$ ) that is the length of the spring at rest (Figure 4-8a). Figure 4-8b shows an axial force  $F_Y$  placing a spring under a state of compression and changing its length to a new length  $L_1$ . Figure 4-8c shows the free-body diagram of the system and the spring internal force  $F_S$ , which is determined by the equation in Figure 4-8d. In the Finite Element Method, linear springs that reside in 3-dimensional space are modeled as trusses elements in 3-dimensional space.

In order to define a linear spring in 3-dimensions in ITKFEM module, 2 point coordinates are needed, a modulus of elasticity ( $E$ ), a Poisson ratio ( $\nu$ ) and an area ( $A$ ). The area for each spring element  $i$  is the sum of one third (because each triangle has three vertices) the areas of all triangles surrounding the vertex  $i$  and denoted in Equation 4-1 as  $A_i$ . In this manner, even though the triangular mesh in the STL file is irregular (Figure 4-3); all the springs in the entire bed have the same proportional strength, because the spring stiffness coefficient for each spring element ( $k_i$ ) is set proportional to the area  $A_i$ , as seen in Equation 4-1 [46] the elastic modulus ( $E$ ) and the spring length ( $L_0$ ) are kept constant.

$$k_i = \frac{A_i E}{L_0} \quad (4-2)$$

## Program Parameters

### Input Parameters

In addition to the STL file, the program requires five input parameters that are set for convenience of coding and not to achieve a particular real world test, they are: the natural length ( $L_0$ ) for all linear springs that compose the bed of springs, external force magnitude, the height of the rigid layer ( $h$ ), the modulus of elasticity for the spring elements ( $E_s$ ) and the modulus of elasticity for the rigid surface ( $E_r$ ) [46].

### Spring height

The spring height is set to 0.1 mm, primordially because the displacements are expected to be very small, close to 0.001 or 0.002 mm. The system was design to include linear spring element which do not carry friction and when grounded in all three direction they behave as a ball-and-socket joint.

### External force magnitude

The external force magnitude is calculated by Equation 4-3 and selecting an expected axial displacement ( $\Delta L$ ) of 1% the spring's length. As shown by Equations 3-2 and 4-2, the force required to move a spring a certain displacement is proportional to the cross sectional area of the spring. In a similar way, in order to calculate a average external force magnitude that corresponds to a single spring's displacement of 1%, the force must be weighted by the mask's surface area per number of springs, as shown in Equation 4-3.

$$\frac{\text{AverageForce}}{\text{spring}} = \left( \frac{\frac{\text{area}}{\text{spring}} * E_s}{L_0} * \Delta L \right) \quad (4-3)$$

### **Rigid layer height**

The height of the rigid layer was set to 1.0 mm because increasing the high of the rigid layer increases the rigidity of the frame, and 1.0 mm was found to be the appropriate value (Table 4-1). The rigidity of the frame was quantified with the RDR ratio and Table 4-1 shows that reducing the height of the rigid layer considerably affects the rigidity of the rigid frame. For example, in Table 4-1, a RDR of three over one thousands signifies a 0.3% rigidity loss. In addition, the rigidity is affected by the shape (length and height) of the tetrahedral elements [41]. Since STL information is used to mesh the rigid tetrahedral layer, and the STL facets are not regular triangles, the shape of the tetrahedral elements affects the rigidity; by increasing the height of the rigid layer the tetrahedral elements behaves more rigidly [41].

### **Difference in elasticity**

The elasticity of the rigid layer ( $E_r$ ) is set to have a modulus of elasticity six orders of magnitude higher than that for the bed of springs ( $E_s$ ). Six orders of magnitude is the largest difference that can be established without compromising the numerical stability of the global stiffness matrix. The sparse matrix linear solver Cholmod [13] has an output value which signifies the conditional number of the matrix that relates to the numerical stability of the system of equations, called rcond. It was found that unreliable values resulted when rcond is equal or exceed  $1e-13$ . A difference of six orders of magnitude for the  $E_r$  and  $E_s$  maintains the rigidity and results in a reliable simulation. Table 4-2 shows the how the difference in elasticity between  $E_r$  and  $E_s$  affect the RDR ratio and Cholmod's rcond value.

### **Output Parameters**

For every external force applied onto the rigid layer, there will be a resulting displacement vector ( $\mathbf{d}_i$ ) at every spring  $i$  that make up the bed of springs (Figure 4-9). The displacement vector for each individual spring is characterized by two components, the normal displacement

along the axis of the spring and the tangential displacement perpendicular to the axis of the spring. The normal displacement scalar (or distance) ( $n_i$ ) is calculated by the dot product between the direction of the spring ( $\mathbf{N}_i$ ) and the displacement vector ( $\mathbf{d}_i$ ), (Figure 4-9). The tangential displacement scalar ( $t_i$ ) is calculated by the cross product between the direction of the spring ( $\mathbf{N}_i$ ) and the displacement vector ( $\mathbf{d}_i$ ) divided over the norm of  $\mathbf{N}_i$ .

As Equation 4-4 shows, the compression or tension state of a linear spring is determined by its normal distance ( $n$ ). If the normal distance is less than or equal to zero, the spring is known to be in compression, and if the normal distance is greater than zero, the springs is know to be in tension.

$$\begin{aligned} n_{i \text{ compression}} &= \mathbf{d}_i \bullet \mathbf{N}_i \leq 0 \\ n_{i \text{ tension}} &= \mathbf{d}_i \bullet \mathbf{N}_i > 0 \end{aligned} \quad i \text{ is the number of springs} \quad (4-4)$$

In a similar manner, regardless of the direction of the tangential displacement vector, the tangential distance  $t_i$  is the perpendicular distance from the axis of the spring ( $\mathbf{N}_i$ ) (Equation 4-5 and Figure 4-6) to the final position of the spring (point c on Figure 4-9).

$$t_i = \|\mathbf{d}_i \times \mathbf{N}_i\| / \|\mathbf{N}_i\| \quad i \text{ is the number of springs} \quad (4-5)$$

Linear springs have an inherent characteristic of only responding to axial forces, their internal forces (which are triggered by an application of an external force) should only be measured by it normal displacement ( $n$ ). This means that springs (in the simulation) that predominantly have tangential displacements are not developing internal forces and are not contributing to the stability of the frame onto the patient's model. For example, in Figure 4-10, the external force ( $\mathbf{F}$ ) applied onto a rigid box results in the development of internal forces in the springs aligned with the external force ( $\mathbf{F}$ ), or springs 1, 2 and 3. The tangential displacement and change in length of springs 4, 5 and 6 is due to their attachment to the rigid box, and though

the spring is stretching, its normal displacements is very small (insignificant) and therefore they do are not developing noteworthy internal forces. However, the tangential displacement of an individual spring is a good indicator of the sliding, slipping or rotation of the frame on the patient's model because it gives evidence on the internal forces being developed by other springs. When there are few springs aligned with the external forces the mask experiences tangential displacements and these are expected to be high.

In accordance with the inherent characteristic of linear springs, the final length of a spring ( $L'$  in Figure 4-9) is not a good indicator of the internal forces developed by a linear spring as a response to external forces; however, the final length does helps in determining which springs are exceeding the bounding compression region as shown in Figure 4-11.

### **Criteria**

For this investigation two criteria were defined. The first criterion is a single spring criteria, which determines if the resulting displacement of a single spring is acceptable to aid in the definition of stability. The second criterion is a single force criterion that looks to define if the frame sustains contact and has a unique fit at the onset of a single external force. With the information from the single force criterion an overall instability score for each mask is determined. This is done by providing a percentage ratio between the forces that result in instability and the total number of forces that were applied onto the mask.

The criteria was designed with the expectation that for the stable mask cases, the displacements of the springs will fall on the upper area of the sphere in Figure 4-11, because the external forces applied in the simulation are small. Accordingly, it is expected that the stable masks would not experience full compression or come close to the boundary condition surface. For this reason a ratio called the TNT ratio, which is an indicative of the tangential displacement to normal displacement was define to aid in differentiating between springs that are in a state of

compression, but experience mainly tangential displacement. The TNT ratio is a part of the single point criterion, its definition, the determination of a threshold value and its consistency is discussed in the following sections.

### **TNT Ratio**

The TNT ratio is a normalized measure of the tangential movement of an individual spring with respect to its normal displacement. The TNT ratio is an indication of the fractional slippage of an individual spring. It is calculated from each individual spring's tangential ( $t_i$ ) and normal ( $n_i$ ) displacements (Figure 4-6). Numerically, it is defined by Equation 4-6 as the tangential displacement magnitude ( $t$ ) divided by the sum of the normal displacement magnitude ( $n$ ) and the tangential displacement magnitude ( $t$ ) (Figure 4-9).

$$TNT = \frac{t}{t + n} \quad (4-6)$$

The purpose of the TNT ratio is to differentiate, for small displacements, between springs that are predominantly sliding to springs that are predominately in compression. In Figure 4-10 a force ( $F$ ) is moving a rigid box by a unit displacement in the negative  $x$  direction and is placing three horizontal springs (springs 1, 2, and 3) in compression; since the three horizontal springs are experiencing only compression ( $n = 1$  and  $t = 0$ ), the TNT ratio for all of them is equal to zero. Assuming the box is perfectly rigid, the vertical springs (springs 4, 5 and 6) will be mostly sliding, ( $n = 0$ ,  $t = 1$ ) and their TNT ratio will be equal to 1 by Equation 4-6. After the application of the force ( $F$ ), the horizontal springs will be the only ones developing internal forces to sustain the movement to the rigid box. The vertical springs in Figure 4-10, are not contributing to with their internal forces to the equilibrium of the rigid box, since linear springs are characterized by not responding to perpendicular forces. The displacement of these springs (springs 4, 5, and 6) result from the sliding movement of the rigid box. The TNT ratio

distinguishes springs that slip (or move tangentially) like springs 4, 5 and 6 in Figure 4-10, from springs that compress, like springs 1, 2 and 3 in Figure 4-10.

Furthermore, Figure 4-13 shows two springs in compression; Figure 4-13A shows a spring with a TNT ratio of 0.5 and Figure 4-13B shows a TNT ratio of 0.833. In the case of the latter spring, its normal displacement is in the compression direction ( $n \leq 0$ ) and final spring length is smaller than the original length ( $L' < L$ ), yet this spring is not contributing to the compressive state of a mask. Its behavior is mostly a result of the sliding movement of a rigid body. If a surface has irregularities that can stop the rigid frame from sliding, then the TNT ratio for a particular spring will result in small values (close to 0). In contrast, if the surfaces are smooth, the bodies can move excessively relative to the grounded (fixed) springs, resulting in springs with high TNT ratios that will approximate one (Figure 4-14).

### **Single Point Criterion**

The single point criterion determines if an individual spring is contributing to the stability of the rigid frame onto the patient's model or not. By the single point criterion a spring that contributes to the stability of the frame by experiencing a considerable state of compression is called a "good compressor".

Table 4-3 shows that a "good compressor" is a spring defined by a normal displacement less than or equal to zero ( $n \leq 0$ ), a final spring's length ( $L'$ ) less than or equal to the original spring's length ( $L$ ) ( $L' \leq L$ ) and a TNT ratio below or equal to 0.7. In addition, Figure 4-12 shows a 2-dimensional interpretation of the single point criterion. In order for a spring to be considered a "good compressor", it must remain inside the red area (Figure 4-12). The red area is bounded by the area below the horizontal red line (including the line), which indicates that the normal displacement is less than or equal to zero (compression); the area inside the half circle (including the line), which indicates that the spring should remain inside its compression bounds

and the area under the incline line, which represents a TNT ratio set to 0.70. The slope of the incline line (blue) corresponds to a normal displacement of 1 and a tangential displacement of -2.41, which corresponds to a absolute TNT ratio of 0.7. As mentioned before, it is expected that the springs have small displacements, so the TNT ratio of 0.7 (inclined line) will differentiate between springs that either have a very small normal displacement and a large tangential displacement or springs that have a very small normal and tangential displacement; in both case these springs are not considered “good compressors” because they are not contributing to the stability of the rigid frame by not developing considerable internal forces. The TNT threshold was set to 0.70 because it was defined empirically to correlate with the information about the real stability of the large masks and the instability of the small masks. For example, Figure 4-13B shows that there are occasions where the normal displacement shows a compression state and yet the tangential displacement is high; by defining TNT upper threshold of 0.7, a spring like in Figure 4-13B will be excluded from being considered a “good compressor”, it has a TNT ratio of 0.833.

### **TNT threshold**

The threshold for the TNT ratio was defined empirically to be 0.7 based on the training data provided by the six masks constructed with rapid prototyping and their fitting onto the solid models (Figure 7-1, 7-2, and 7-3). To determine this empirically the simulation was ran with TNT ratios of 0.6, 0.7 and 0.8 for large and small masks (Figure 4-15 and 4-16 respectively). In the simulation a TNT ratio of 0.70 corresponds with the physical stability of the large masks and instability of the small masks.

Figure 4-15 shows color coded surface plot for all three large masks, Caucasian, Asian and infant at different TNT ratios (0.6, 0.7 and 0.8). The location of the color dots correspond to the location where a virtual force was applied and three or more points behaved as “good

compressors” (Table 4-3). The color of the dots corresponds to the maximum tilt angle (for all spin angles) where at least three “good compressors” were found. For example, a red dot signifies that for a maximum tilt angle of  $90^\circ$  (and for all spin angles) three or more “good compressor” springs were found, that is 49 forces resulted in at least three “good compressor” springs.

The first row in Figure 4-15 associates to a TNT of 0.6, and as the figure shows, the Asian and the infant mask are noted as false negatives, because the color coded surface plots show that the maximum tilt angle in which the forces was withheld is smaller than  $90^\circ$ , this indicates that the application of a force resulted in an unstable configurations (this information contradicts that premise that the large masks are stable). The second and third rows, which correspond to TNT ratio of 0.7 and 0.8 respectively, concur with the physically stability of the masks; but in Figure 4-16, a TNT threshold of 0.8 dictates a case of false positive for the small Asian mask, which is mark as maintaining alignment for all forces at all locations. This information also contradicts the premise that the design of the three small masks results in a unstable configurations.

Figure 4-14 shows that when a tangential displacement magnitude is 2.41 times bigger than the normal displacement magnitude the TNT ratio is equal to 0.70. Also a TNT ratio of 0.5 occurs when the tangential displacement is equal to the normal displacement, and the TNT ratio approaches one when the springs experience mostly tangential displacements (Figure 4-14). In summary, a TNT upper threshold was empirically defined at 0.7, this means that all springs that are in compression and exhibit TNT ratios of 0.7 or below are in a “good” compressive state. On the other hand, the springs that exceed a TNT ratio of 0.7 will be regarded as mainly slipping or sliding.

### **Consistency of TNT threshold**

To test the consistency of the TNT threshold, the force magnitude was increased five and ten times, and the number of point on the mask was increase for a single mask case (Figure 4-17). When the force was increased by five and ten times there were no changes in the color coded surface plots shown in Figure 4-14. This means that the TNT threshold is not sensitive to force. In the case of increase number of points, the results are shown in Figure 4-18; which illustrates that with the exception of one single point in the upper left corner of the Asian large mask, which held stability up to a theta value of  $75^\circ$ , the TNT threshold of 0.7 corresponded with physical results.

### **Single Force Criterion**

The purpose of the single force criterion is to define on a per force basis if the frame or mask is stable or not. The criterion requires a minimum of 3 points in compression, that is 3 “good compression” points (as defined by the single point criteria) to consider a mask stable with relation to a particular force vector. Three springs in compression will overcome for translations and rotations of the frame. Translation can be recognized by evaluating the movement of a single point, but two points are needed to recognize rotation, since rotation occurs about a normal vector and at a specific point that may not move. Translations or sliding is defined as the relative motion between two surfaces and rotation is the angular motion about a common normal [45]. The criterion requires a third point because three points are necessary to identify rotation in 3-dimensions.

If the displacement of the rigid body results in three “good compression” points, the simulation indicates that the rigid surface is moving close to the grounded points rather than sliding or rotating, which in turn indicates that the mask and model surfaces remain in alignment. If by the onset of an external force the mask results in a configuration where there are less the

three “good compression” points, then the mask is known to be unstable for that particular force. Intuitively, more than three “good compression” points and their dispersion can give evidence of a level of stability. More “good compression” points and broadly disperser leads to greater stability. Therefore, a bounding volume defined by the minimum volume of all “good compressor” points compared to the bounding volume of the entire mask, is a good indicator of the level of stability of the mask for a particular force.

**Box ratio:** The box ratio quantifies the level of stability as defined by the single force criterion by calculating a ratio between the volume of the compression patch ( $c_{vol}$ ) and the volume of the entire frame model ( $f_{vol}$ ) (Figure 4-18). The box ratio is calculated on a per force basis. The compression patch volume is the minimum volume that includes all “good compression” springs (Figure 4-19). If the mask is unstable, with respect to a particular force (as defined by the single force criteria), then the compression patch volume is equal to 0. The small box in Figure 4-18 shows a compression patch volume ( $c_{vol}$ ), in comparison with the volume of the entire frame ( $f_{vol}$ ). The box ratio is numerically defined by the compression patch volume  $c_{vol}$  over the entire frame’s volume  $f_{vol}$  (Equation 4-7).

$$Box \cdot ratio = \frac{c_{vol}}{f_{vol}} \quad (4-7)$$

As Equation 4-7 shows, a box ratio is equal to 0 when the compression patch volume is equal to zero (or the mask is unstable) (Figure 4-19). When the mask is found stable for a particular force, a compression patch volume takes a value greater than zero. A box ratio close to 1 indicates that the compression patch volume approximates to the volume of the entire frame (Figure 4-19). Box ratios closer to the value of zero correspond to smaller compression patch volumes or “good compressor” points close to each other.

A score for the overall instability (instability score) of the masks can be derived from the single force criteria by providing with an percentage value for the number of forces that result in instability (box ratio equal to 0) to the total number of forces applied to the mask (Equation 4-8). If this value is equal to 0%, there were not external forces that made the mask loose stability, and if this value is 100% it means that all external forces disrupted the alignment of the mask onto the patient's surface.

$$\text{Instability score} = \frac{\text{\#of forces the result in instability}}{\text{total number of forces applied onto the mask}} \times 100 \quad (4-8)$$

In summary, a total of 49 external forces will be applied to all non-edge points onto a mask (if a mask has 300 non-edge points, there will be 14700 forces applied to it).

- For each individual external force applied onto a mask, there will be displacements of all springs that comprise the bed of springs.
- The single point criteria will individually classify each spring as a “good compressor”.
- The number of “good compression” points is recorded.
- If there are less than 3 “good compression” points, the mask is considered unstable, the compression patch volume is equal to zero, and the box ratio is equal to one.
- If there are 3 or more “good compression” springs then the mask is considered stable and the compression patch is calculated and the box ratio will have a value between 0 and 1.

As an overall percentage instability score for a mask, the number of forces the result in instability is compared to the total number of forces applied onto the mask. A value of 0% means zero instability (Equation 4-8).

Table 4-1. Relationship between the tetrahedral height and a measure of the rigidity of the rigid layer.

| Tetrahedral height | Mean RDR      |
|--------------------|---------------|
| 1 mm               | 3/1000 (0.3%) |
| 0.1 mm             | 2/100 (2%)    |
| 0.01 mm            | 2/10 (20%)    |

Table 4-2. Table that shows the relationship between the difference in elastic modulus between the rigid layer and the bed of springs and the rigidity measure and Cholmod's rcond value.

| $E_r - E_s$ | Mean RDR | Cholmod's rcond |
|-------------|----------|-----------------|
| 1.0e6       | 3/1000   | 2.14e-8         |
| 1.0e7       | 2/1000   | 2.14e-9         |
| 1.0e8       | 5/1000   | 2.14e-10        |

Table 4-3. Single point criteria.

|         | Compression   | Tension                |
|---------|---|------------------------|
| No Slip | $n \leq 0$ and<br>$L' \leq L$ and<br>$TNT \leq 0.70$<br>"good compressor" | $n > 0$ or<br>$L' > L$ |
| Slip    | $n \leq 0$ and<br>$L' < L$ and<br>$TNT > 0.70$                            | $n > 0$ or<br>$L' > L$ |

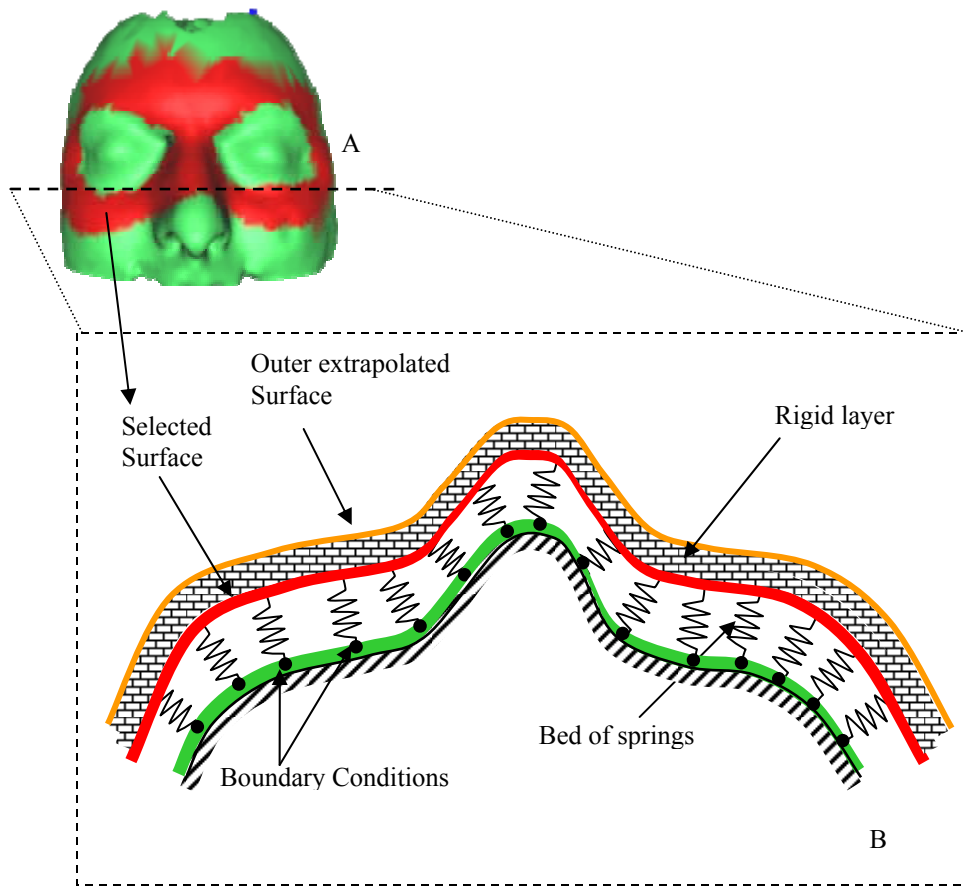


Figure 4-1. The methodology for stability of fit involves simulating a rigid layer onto of a deformable bed of springs. A) The selected surface (red) as painted on the rendered model (green). B) A cross section through the selected surfaces and anatomical model showing the idealization of the contact mechanics between the rigid frame and the solid model

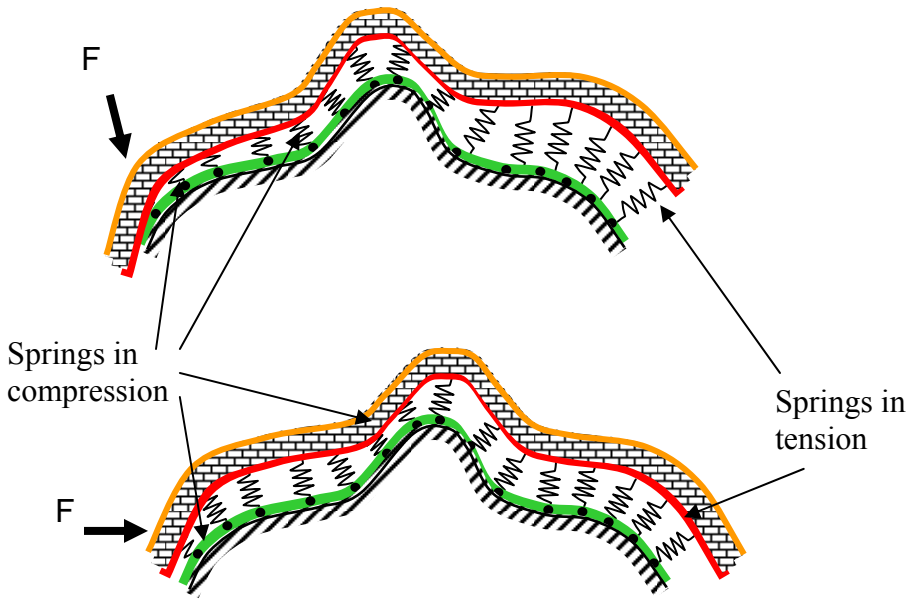


Figure 4-2. Displacement of a mask as it responds to external forces.

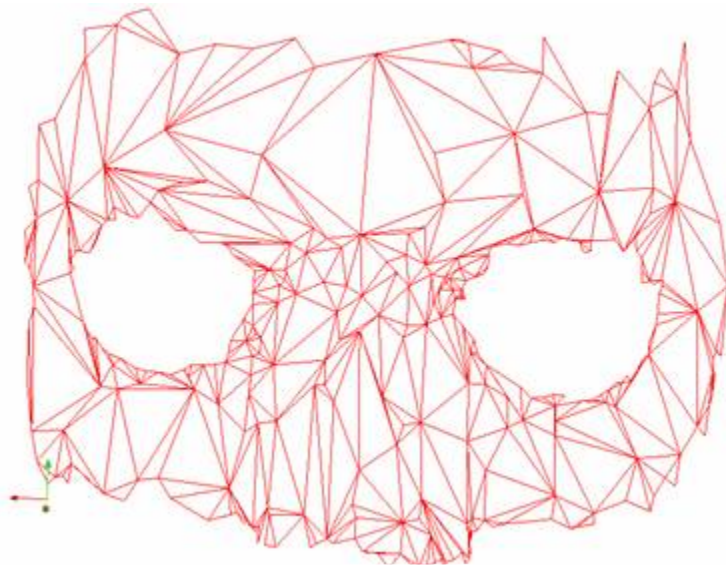


Figure 4-3. Triangulation of a customized positioning device proper to STL format. Every vertex in the mask is a point coordinate in 3D space.

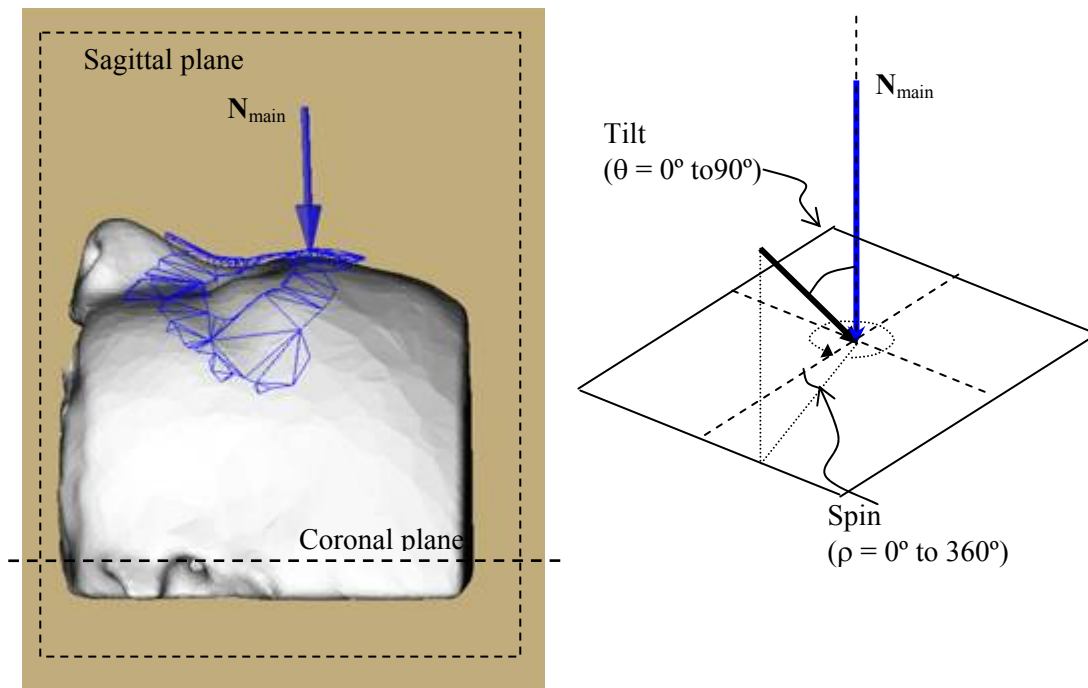


Figure 4-4. Direction of the  $N_{main}$ .  $N_{main}$  is specifically chosen for each mask, and forty nine force directions are calculated by defining a tilt and a spin angle.

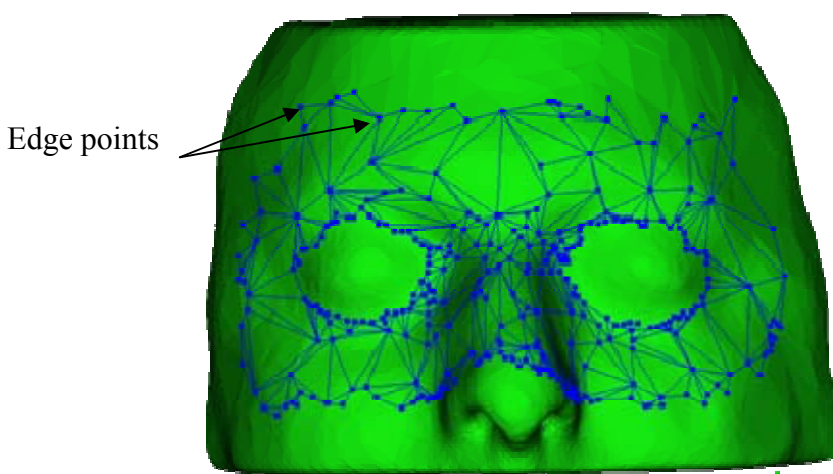


Figure 4-5. Nodes point on the rigid frame. Forces are not applied on edge points.

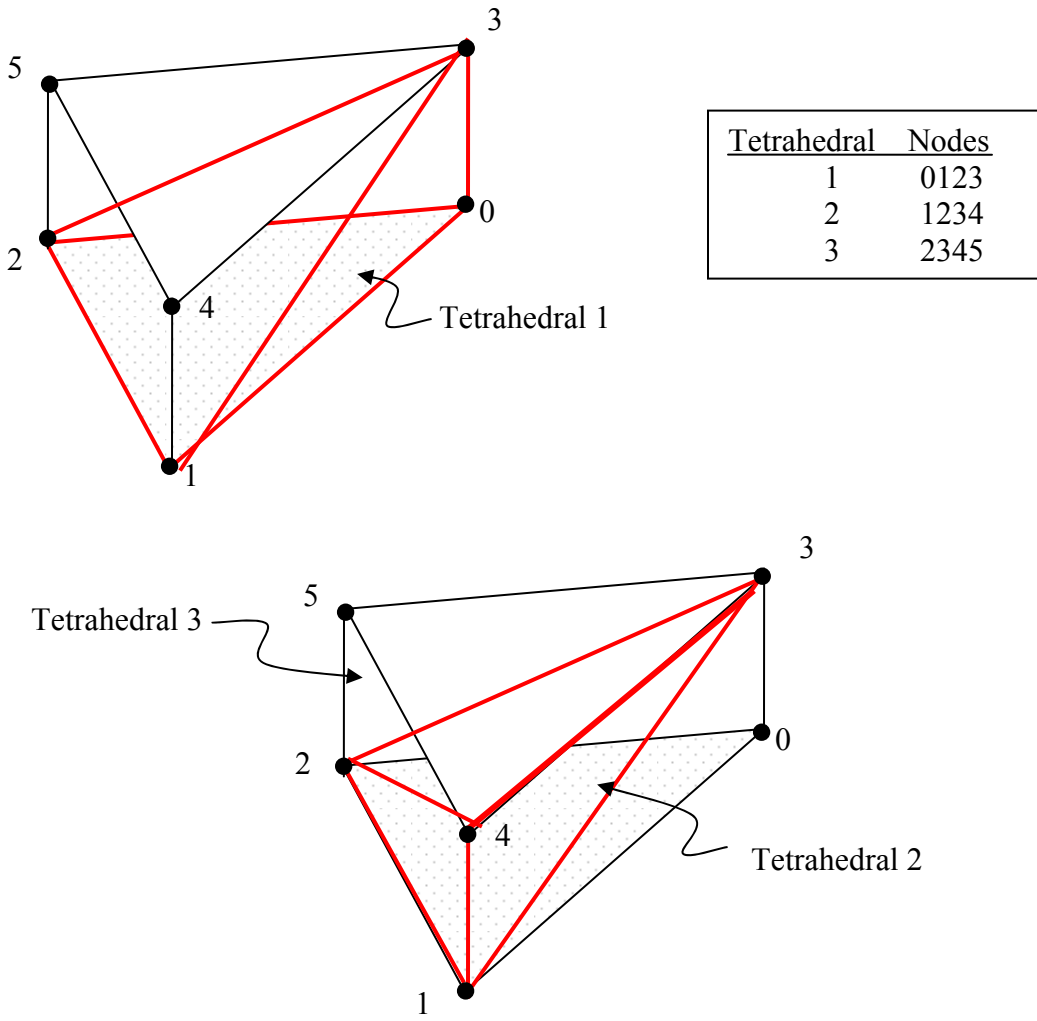


Figure 4-6. In a wedge three tetrahedral elements are fitted. The nodes are shown next to the black dots. The numbering of the tetrahedral elements is important and should be done as shown in the legend.

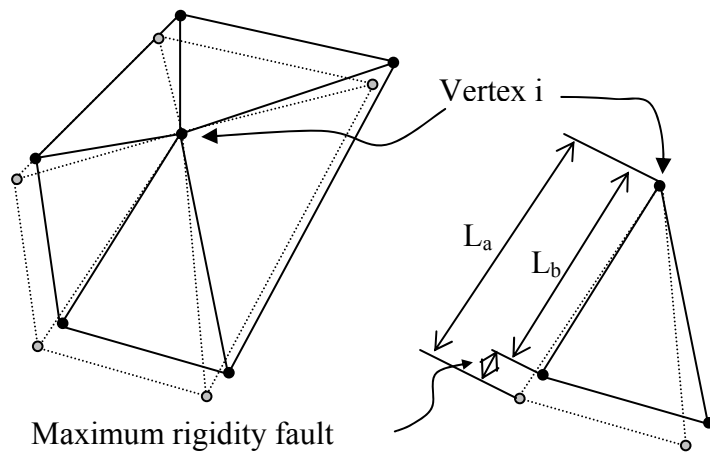


Figure 4-7. Schematic showing how the maximum rigidity fault is calculated.

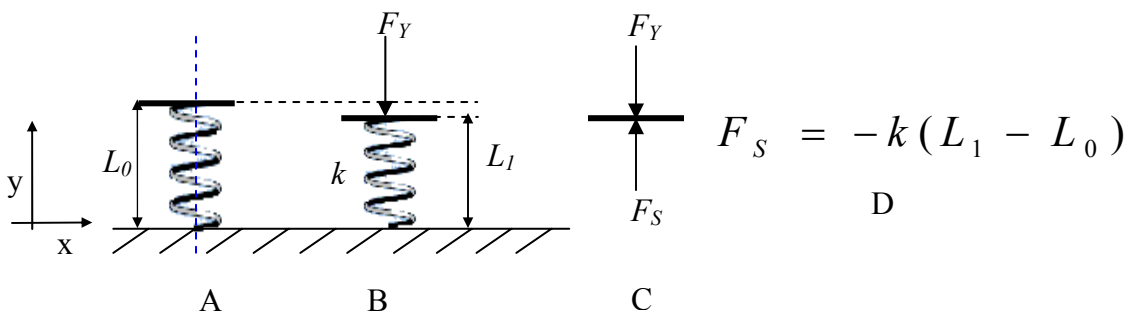


Figure 4-8. The behavior of a linear spring element under the application of an axial force. A) A spring at rest,  $n_l$  is the natural length of the spring. B) The same spring under compression by a force  $F_Y$ . C) Free body diagram of the spring in compression. D) Equation of a linear spring.

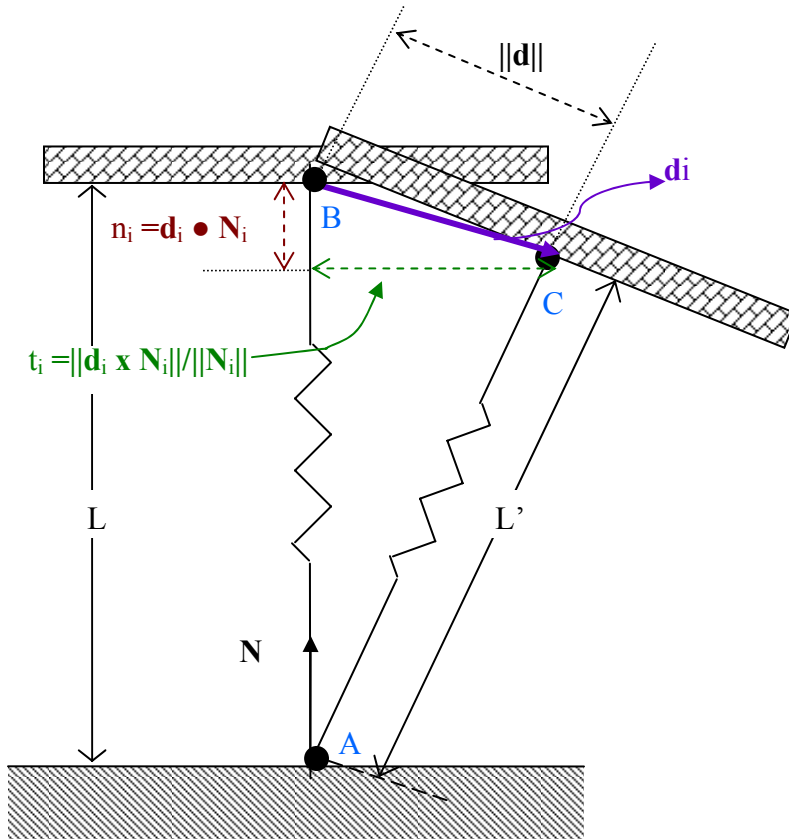


Figure 4-9. Schematic that demonstrates how each spring's displacement was evaluated by identifying the normal ( $n_i$ ) and tangential ( $t_i$ ) displacement magnitudes. The normal ( $n_i$ ) and tangential ( $t_i$ ) displacement are scalar distances. In this particular case the spring is in compression because the normal displacement magnitude  $n_i$  will result in a value less than or equal to zero, also notice that the natural length of the spring has changed from  $L$  to  $L'$ .

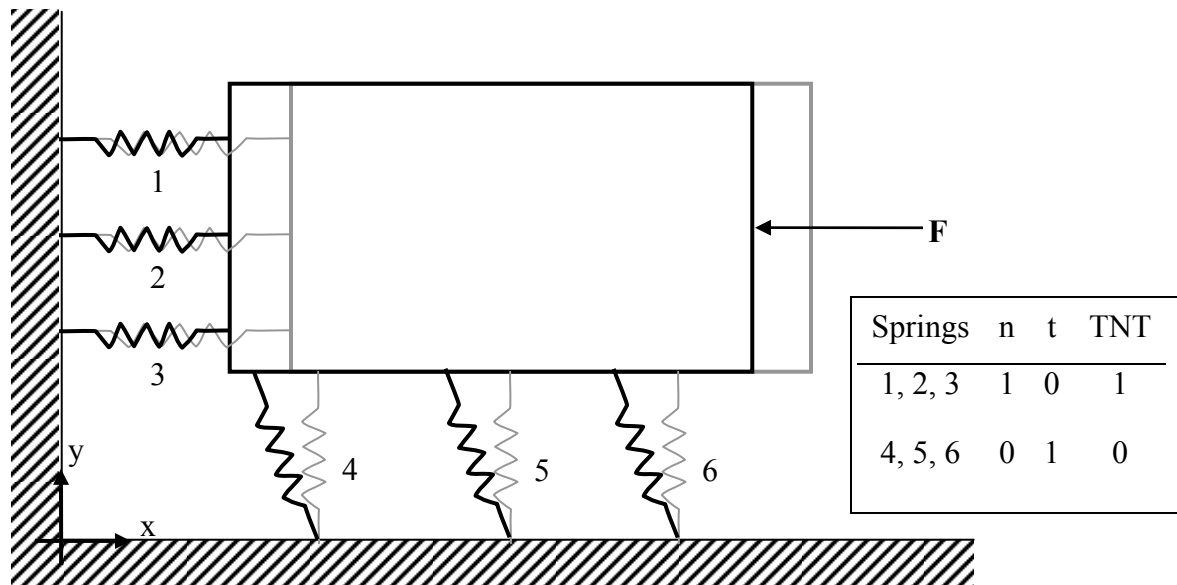


Figure 4-10. Schematic that shows why it is important to distinguish between the springs that are mostly in compression or tension and those that are basically slipping or have a high TNT ratio. The force ( $F$ ) exerts a unit displacement on the rigid box in the  $-x$  direction. As a result of the force the springs have normal ( $n$ ) and tangential ( $t$ ) displacements are shown in table.

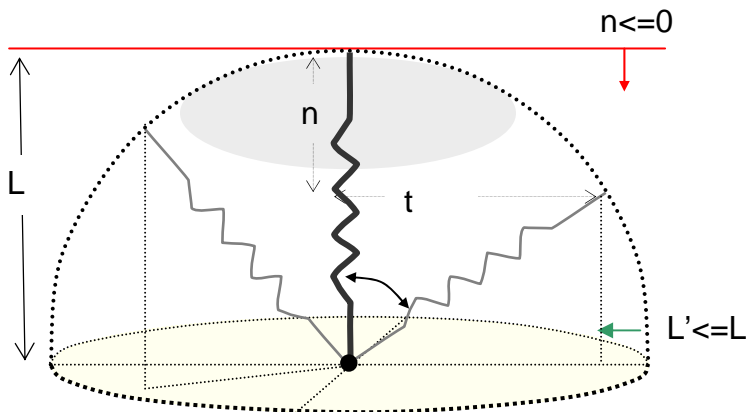


Figure 4-11. Bounding volume for a spring to be in compression. For the stable cases the springs displacements are expected to reside on the upper area of the half sphere (gray area).

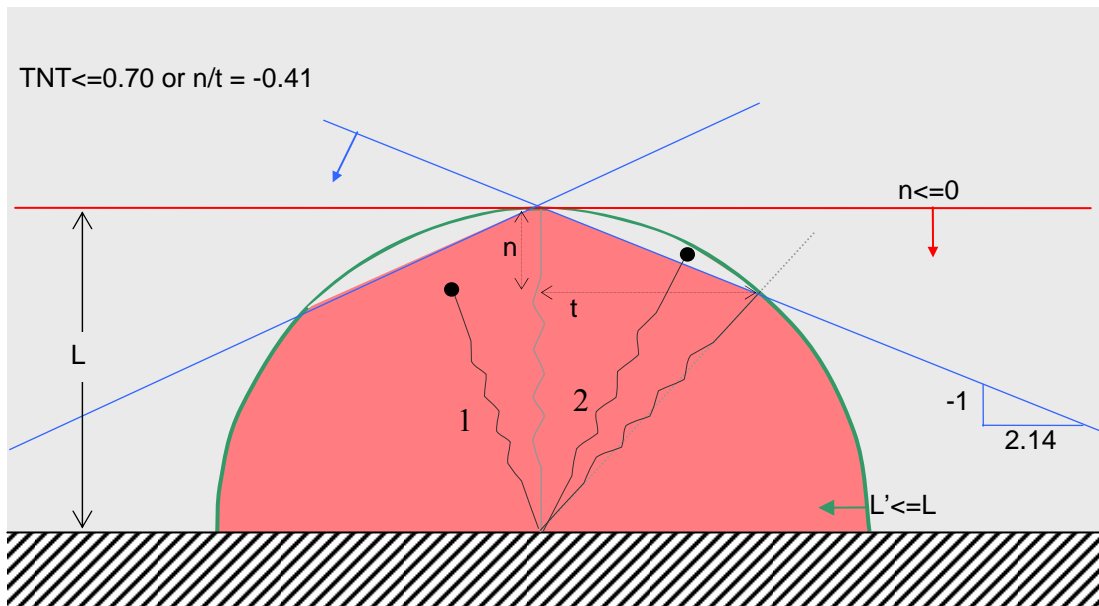


Figure 4-12. Two-dimensional interpretation of the single point criteria. In order for a spring to be considered a “good compressor” it should remain inside the red area. Consider the spring in Figure 4-13A to correspond with spring 1 (with the tangential displacement in the opposite direction), and spring 2 corresponds to the spring in Figure 4-13B.

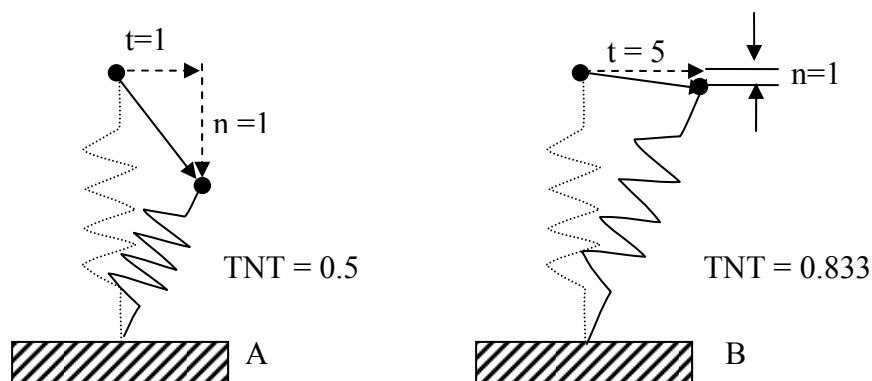


Figure 4-13. Schematic to demonstrate the importance of evaluating the percentage slip of TNT ratio for each spring. A) The TNT ratio in this case is close to 0.5 because the compression and tangential displacements are similar in length. B) The TNT ratio is close to 0.833, because the ratio of compression to tangential displacement is about 1 to 5.

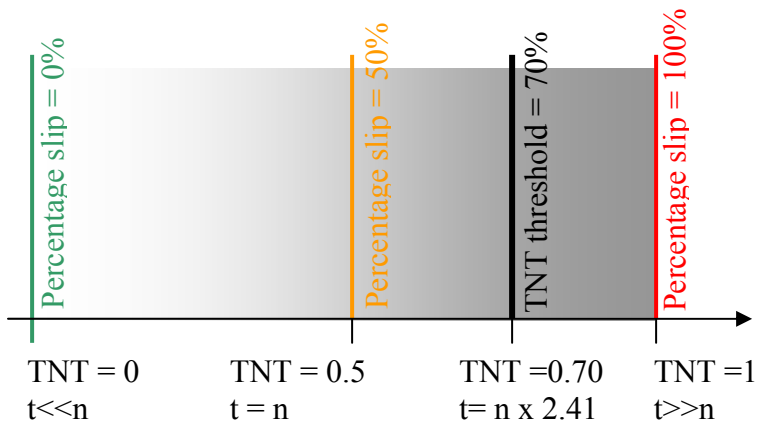


Figure 4-14. Schematic to shows at the level at which the TNT threshold was defined.

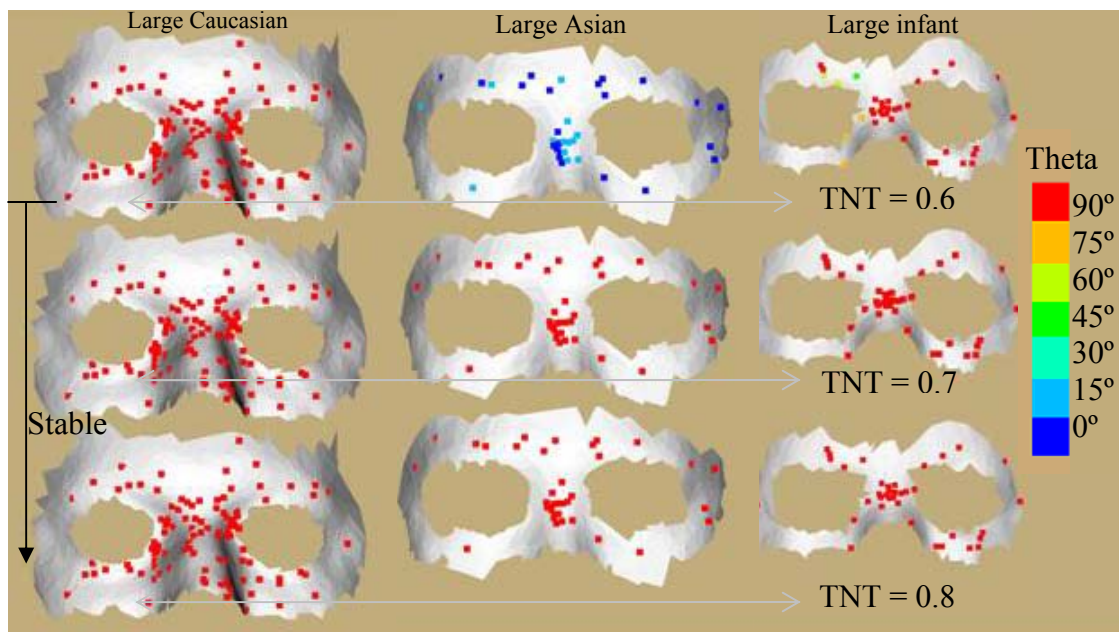


Figure 4-15. Empirical determination that the TNT threshold greater than 0.6 correlates with the training data, which says that the large masks are stable.

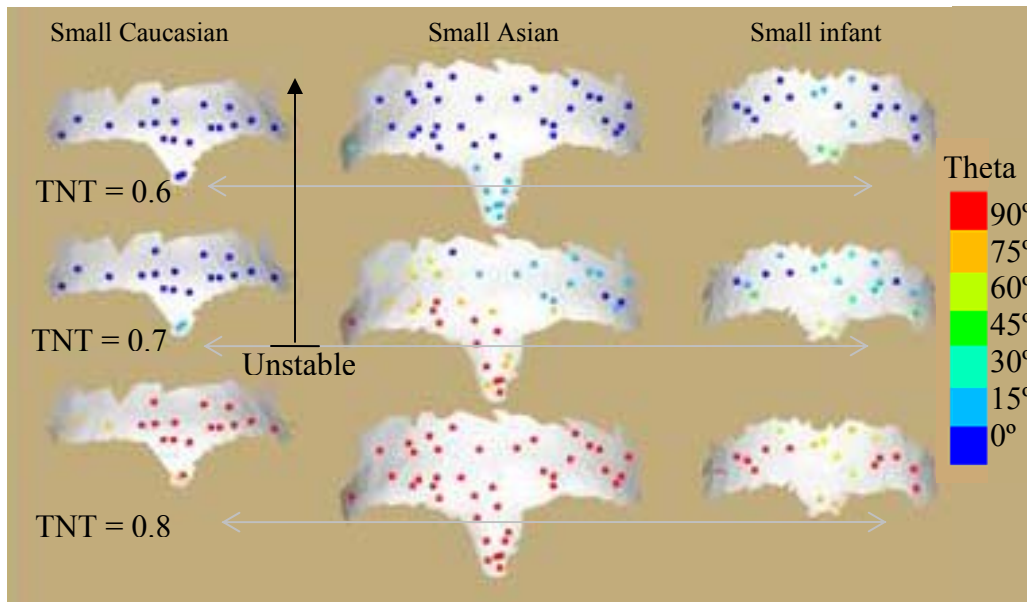


Figure 4-16. Empirical determination that the TNT threshold set smaller than 0.8 correlates with the training data, which says that the small masks are unstable.

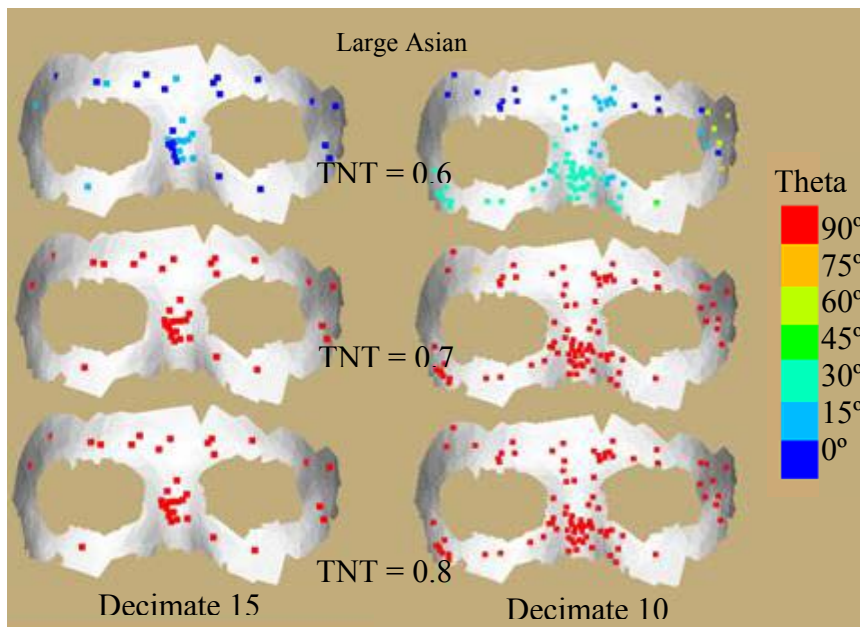


Figure 4-17. A case of the large Asian mask, which shows the consistency of an upper TNT threshold of 0.7. Even when the number of springs is increase, the TNT threshold of 0.70 shows stability.

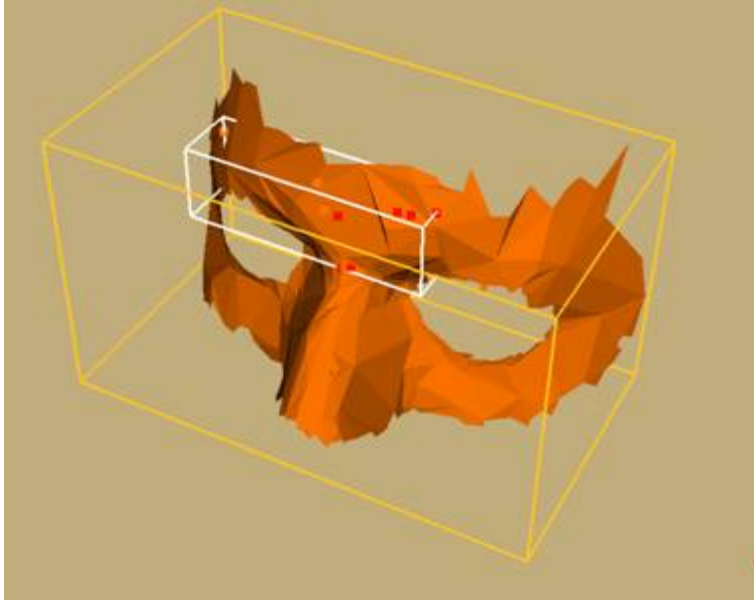


Figure 4-18. Schematic showing the relation between the volume of the entire frame ( $f_{vol}$ ) and the compression patch volume ( $c_{vol}$ ).

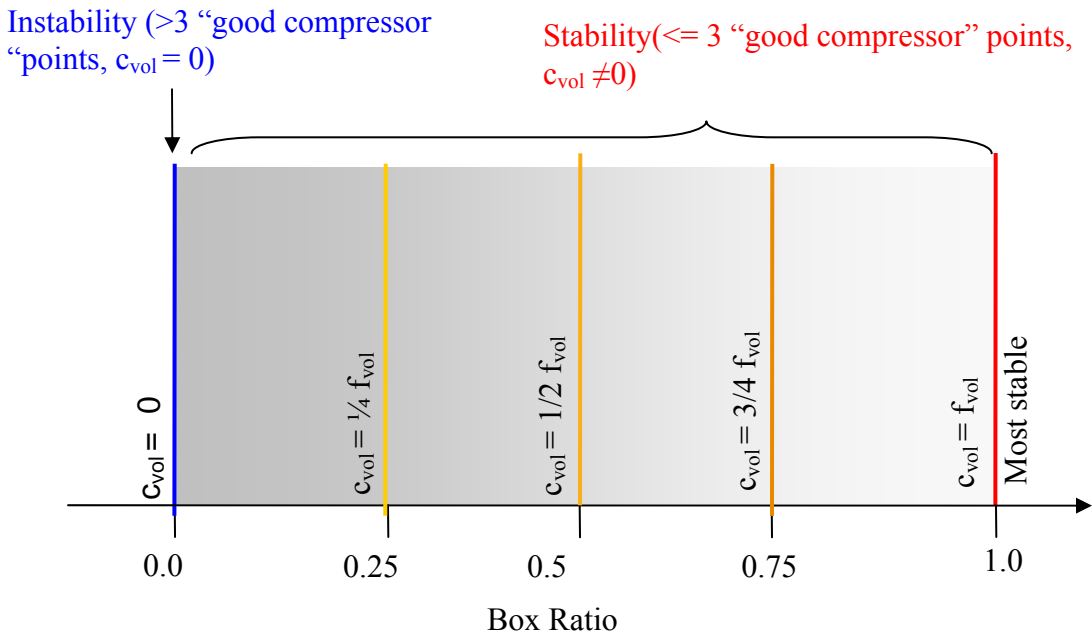


Figure 4-19. Box ratio interpretation. Notice that a box ratio of one is the most stable configuration where the compression patch volume ( $c_{vol}$ ) is equal to the entire volume of the frame ( $f_{vol}$ ), meaning that all points are “good compression” points. Also notice that a box ratio of zero corresponds to instability; since there are less than three “good compression” points, which result in a compression patch volume equal to zero.

## CHAPTER 5 PROGRAM DESCRIPTION AND VALIDATION

### **Program Description**

The program was written in C++ language and it uses open source programming libraries for image visualization: VTK (VTK 4.2, Kitware Inc., Clifton Park, NY) and, for advanced imaging processing, ITK (ITK 1.8, Kitware Inc., Clifton Park, NY). The library for advanced imaging processing has several classes dedicated to finite element method (FEM), which were used to construct the simulation of the contact problem. In addition Cholmod [13] was adapted to solve the linear system of equations particular to the FEM; also Paraview (Paraview 1.6, Kitware Inc., Clifton Park, NY) was used for the visualizations of the results.

The program is organized into five main sections. The first section is dedicated to reading the input information from the STL file, introducing input parameters and preparing the data to be written into the appropriate input format ITKFEM module. The second section requires the ITKFEM module to read the input file previously created and assemble a single global stiffness matrix ( $\mathbf{K}_g$ ) in the correct format for Cholmod. The third section defines the directions of the force at each point on the rigid layer and iterates over all points while storing into arrays the output parameters. The fourth section sorts over the information in the output parameters and applied the single point and global criteria; and finally the last section presents the results, in a histogram format and as a colormap in Paraview. Figure 5-1 is a chart flow of how the program is organized.

The first section of the program starts by reading the STL file and applying an ITK filter that selects the largest region in the STL file. This is done because sometimes additional small surfaces are selected in RPD designer that are not related to the main selected surface. In general the STL surface is characterized as an irregular mesh. The STL serves the purpose well of

describing a surface by dividing it in planar triangles. For this reason, another VTK filter, a decimation filter is applied to reduce the number of triangle that are close to each other and have the same dihedral angle [38]. The decimation filter does not alter the topology of the selected surface; rather it serves the purpose of reducing the number of triangles in the STL mesh [38]. However, sometimes the output of the decimation filter results in relatively large triangles, so an optional function was created that added nodes to large triangles and re-meshes the surface. At this level in the program the surface does not undergo additional modification, and the nodes on the edges are saved to an array for later identification. The next step is to calculate the normal at every vertex. VTK calculates the normals at every vertex on the surface as an average of the normals of the triangles connected to the vertex; however a function was created to calculate a better average normal, which is weighted by the angles of the triangles adjoining to a particular vertex. With the appropriate normal information a top surface and bottom point cloud are created by extrapolating the point coordinate information along the normal in the positive direction and in the negative direction, respectively, as shown in Figure 5-2.

The rigid layer is created by meshing with tetrahedral elements the space between the selected surface and the top surface (Figure 5-2). The bottom point cloud become boundary condition points, fixed in all 3-dimensions and represents the patient's surface. The spring elements that comprise the bed of springs extend from the point cloud to the selected surface (Figure 5-2). Next the program calculates the surface area of the frame and with the expected displacement  $s_e$  to 0.001mm, determines the magnitude of the external force (Equation 5-2). The last step of the first section of the program involves using the point coordinate information and input parameters to write an input file for the ITKFEM module.

Most of section two involves using the ITKFEM classes to read the file created, assemble a single the global stiffness matrix ( $\mathbf{K}_g$ ) that describes the entire system and the global force vector ( $\mathbf{F}_g$ ). Afterwards a function was created to read the global stiffness matrix and write it into an input format for Cholmod. The format required by Cholmod is referred as triplet format, and is a method of writing large sparse matrices in manner that saves computer space and quickens the retrieval of information [13].

The direction of forty nine force vectors is calculated in a combination of forty nine tilts ( $\theta$ ) and spins ( $\rho$ ) about the main normal ( $\mathbf{N}_{\text{main}}$ ) as shown in Figure 4-12. The same small magnitude is assigned to each force vector and all forty nine are applied onto each non-edge nodes on the mask.

One global stiffness matrix ( $\mathbf{K}_g$ ) is assembled for the entire system and is not altered once it is assembled; however, for each force application to a particular node (49 times the number of non-edge points) on the rigid layer, a global force vector  $\mathbf{F}_g$  is populated. In this manner, both the global stiffness matrix  $\mathbf{K}_g$ , and the global force vector  $\mathbf{F}_g$  are given to the Cholmod routines to solve for the displacement vector  $\mathbf{U}$  that characterizes the movement of the frame as a result of a single force application. From the displacement vector  $\mathbf{U}$ , which include displacements for each nodes, the normal (n) and tangential (t) distances are calculated for each node as shown in (Figure 4-8).

In section five, the single point criteria and the global point criteria, as described in Chapter 4, are applied to the tangential and normal scalars. In addition, the program creates histograms for the box ratio per angle rotation and creates a file for visualizing the frame with color-coded information per angle of the maximum angle in Paraview (Paraview 1.6, Kitware Inc., Clifton Park, NY).

## Validation of FEM elements

The validation of the program involves testing the behavior of the linear spring or space truss element and the linear tetrahedral element to assure they respond in the appropriate manner. In addition, the program is tested for a simple case of a corner frame.

### Linear Spring Validation

The validation of linear spring element was performed by testing the displacement of the element in three orthogonal directions as shown in Figure 5-3. In all instances the same mechanical characteristics ( $E$ ,  $\nu$ ,  $A$ ,  $L$ ) were assigned and the same force vector ( $\mathbf{F}$ ) was applied (Figure 5-3). The results of the stiffness matrix as assembled by the ITK FEM module are shown in Equation 5-1, 5-2 and 5-3, which correspond to Figure 5-3A, 5-3B and 5-3C, respectively. The resulting displacements for each case resulted in the same value of 0.1mm in the direction of the force vector, which corresponds to the displacement as hand calculated in Equation 5-4, following the linear spring equation.

$$k^{1A} = \begin{bmatrix} 750 & 0 & 0 & -750 & 0 & 0 \\ 0 & 0 & 0 & 0 & 0 & 0 \\ 0 & 0 & 0 & 0 & 0 & 0 \\ -750 & 0 & 0 & 750 & 0 & 0 \\ 0 & 0 & 0 & 0 & 0 & 0 \\ 0 & 0 & 0 & 0 & 0 & 0 \end{bmatrix} \quad (5-1)$$

$$k^{1B} = \begin{bmatrix} 0 & 0 & 0 & 0 & 0 & 0 \\ 0 & 750 & 0 & 0 & -750 & 0 \\ 0 & 0 & 0 & 0 & 0 & 0 \\ 0 & 0 & 0 & 0 & 0 & 0 \\ 0 & -750 & 0 & 0 & 75 & 0 \\ 0 & 0 & 0 & 0 & 0 & 0 \end{bmatrix} \quad (5-2)$$

$$k^{1C} = \begin{bmatrix} 0 & 0 & 0 & 0 & 0 & 0 \\ 0 & 0 & 0 & 0 & 0 & 0 \\ 0 & 0 & 750 & 0 & 0 & -750 \\ 0 & 0 & 0 & 0 & 0 & 0 \\ 0 & 0 & 0 & 0 & 0 & 0 \\ 0 & 0 & 750 & 0 & 0 & 750 \end{bmatrix} \quad (5-3)$$

$$d = \frac{FL}{AE} = \frac{75N \cdot 2mm}{0.1mm^2 \cdot 1500MPa} = 0.1mm \quad (5-4)$$

### **Tetrahedron Element Validation**

The validation of the tetrahedral element was done by comparing the ITK FEM results to those by ANSYS (Ansys Inc. Canonsburg, PA) following the example in Figure 5-5. Both ANSYS and ITK FEM provided the same displacement shown in Table 5-1.

### **A Simple Model Validation**

The program was validated with a simple frame in the shape of a corner (Figure 5-5). When a force was applied at the location marked with a white dot and in the direction of normal direction at that point; the entire corner was placed in a state of compression as will be expected if a force physically applied onto a corner (Figure 5-5A). In the reverse case where the force vector is inverted and rather than pull it pushes away, the corner results in a complete tension state.

Table 5-1. Displacement in the X, Y and Z direction from the example in Figure 5-4 tested with the ITKFEM module and ANSYS.

| Node | X      | Y      | Z          |
|------|--------|--------|------------|
| 1    | 0.0000 | 0.0000 | 0.0000     |
| 2    | 0.0000 | 0.0000 | -0.5200e-3 |
| 3    | 0.0000 | 0.0000 | 0.0000     |
| 4    | 0.0000 | 0.0000 | 0.0000     |
| 5    | 0.0000 | 0.0000 | -0.5200e-3 |

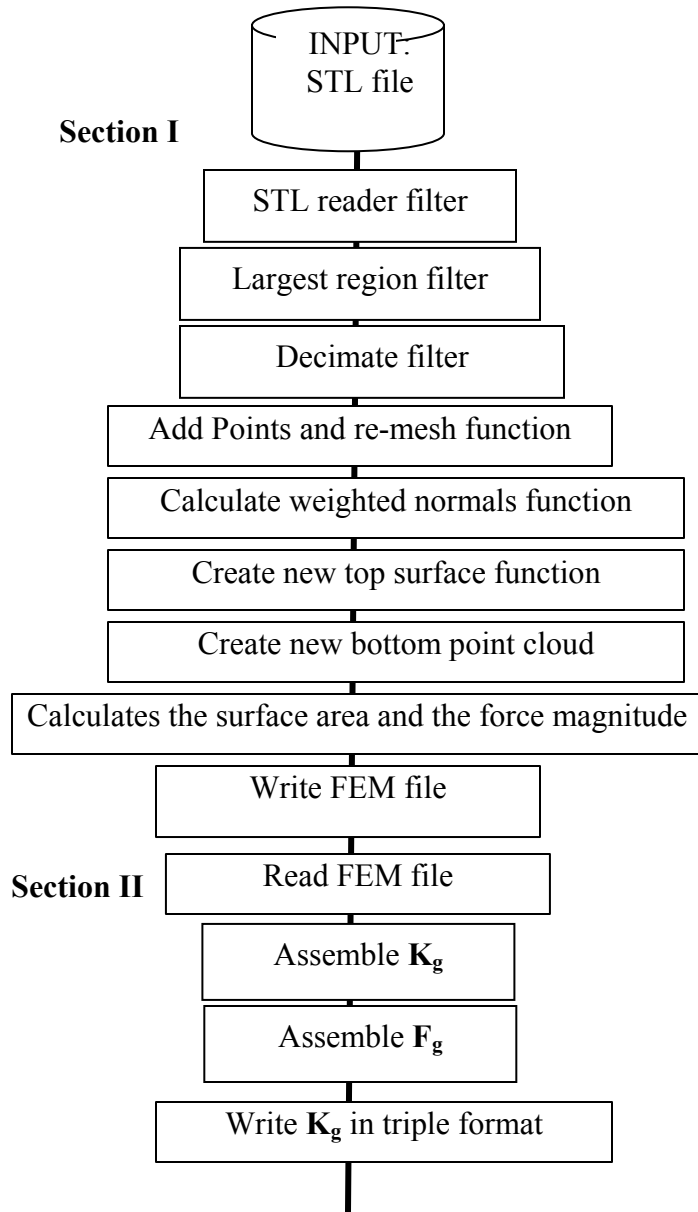
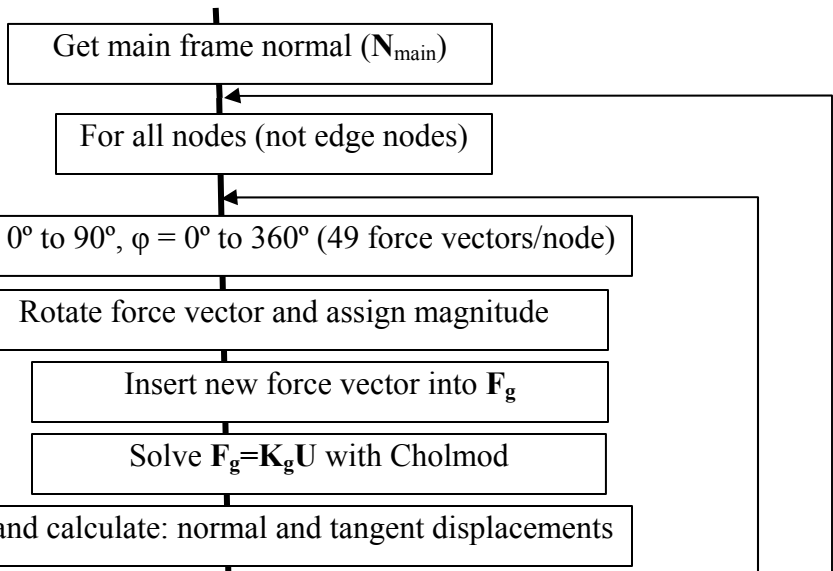


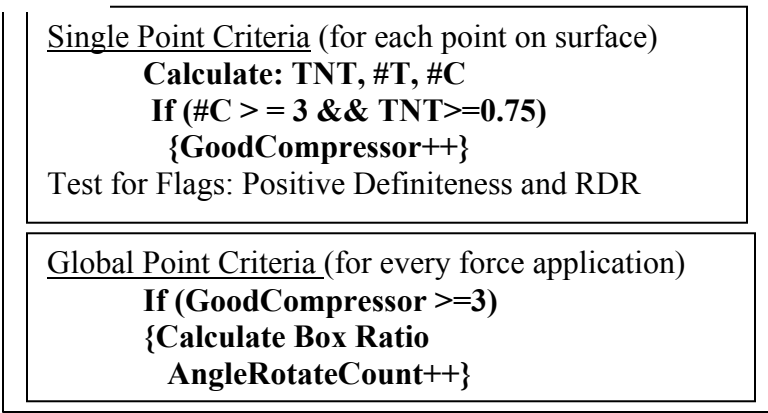
Figure 5-1. Flow chart of program for testing the uniqueness of fit.

**Section III**



**Section IV**

**Apply Criterion**



**Section V**

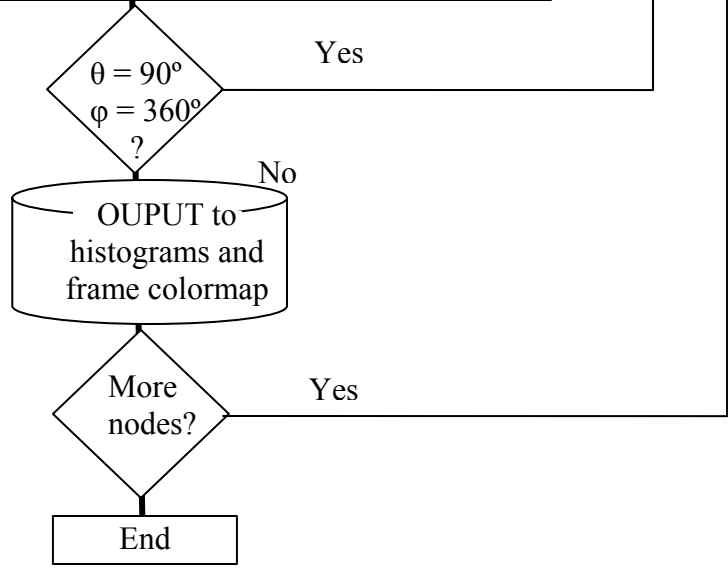


Figure 5-1. Continued.

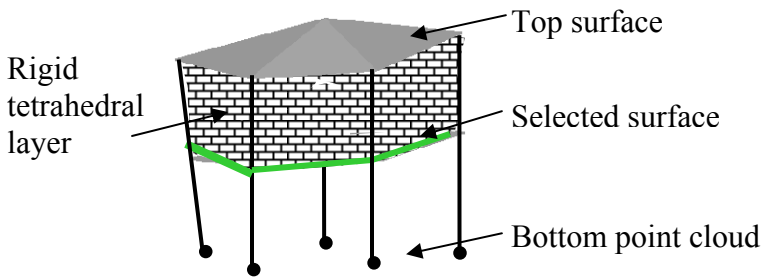


Figure 5-2. Original surface is extended in the positive normal direction to form the top surface and the points extended in the negative normal direction to become boundary condition points.

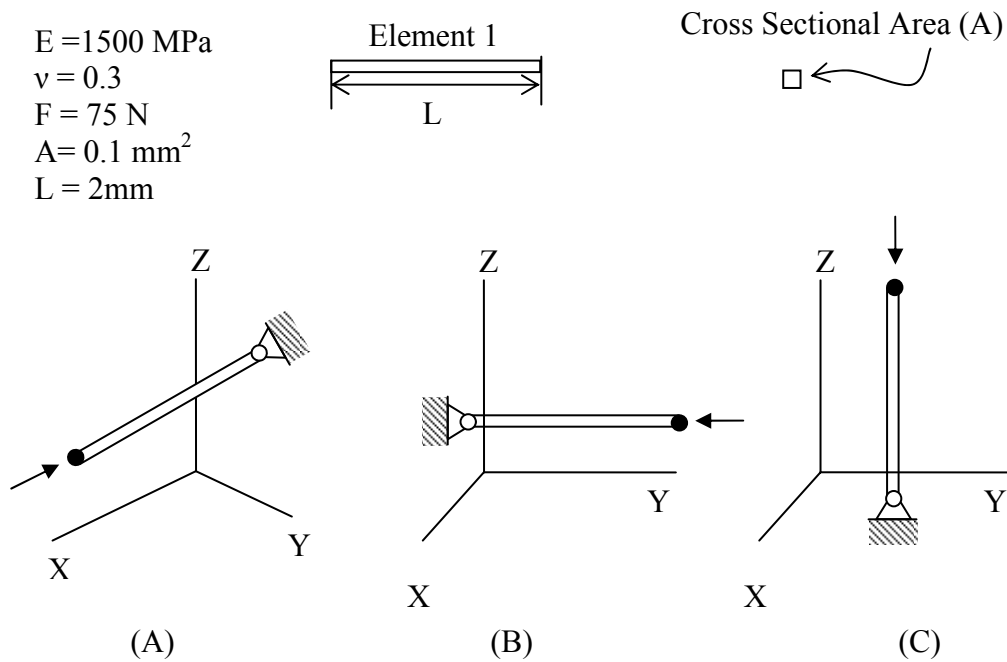


Figure 5-3. Examples of a linear spring element or space truss tested in all 3-dimensions.

$E = 30e6 \text{ MPa}$   
 $\nu = 0.3$   
 $F = 1000 \text{ N}$

| Node | Coordinates (X,Y,Z) |
|------|---------------------|
| 1    | 0, 0, 0             |
| 2    | 0,10,0              |
| 3    | 0, 0, 10            |
| 4    | -1, 0, 0            |
| 5    | -1, 10, 0           |

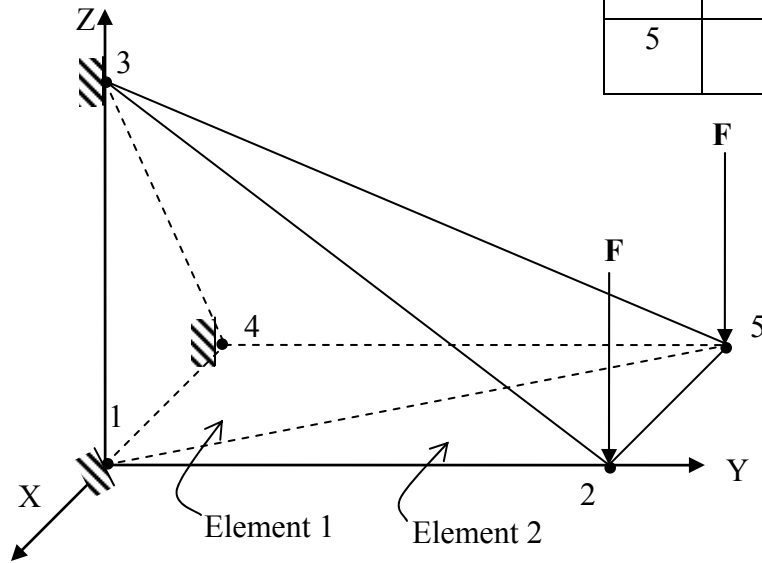


Figure 5-4. Example of two tetrahedral elements used in the validation of the tetrahedral elements used in the program.

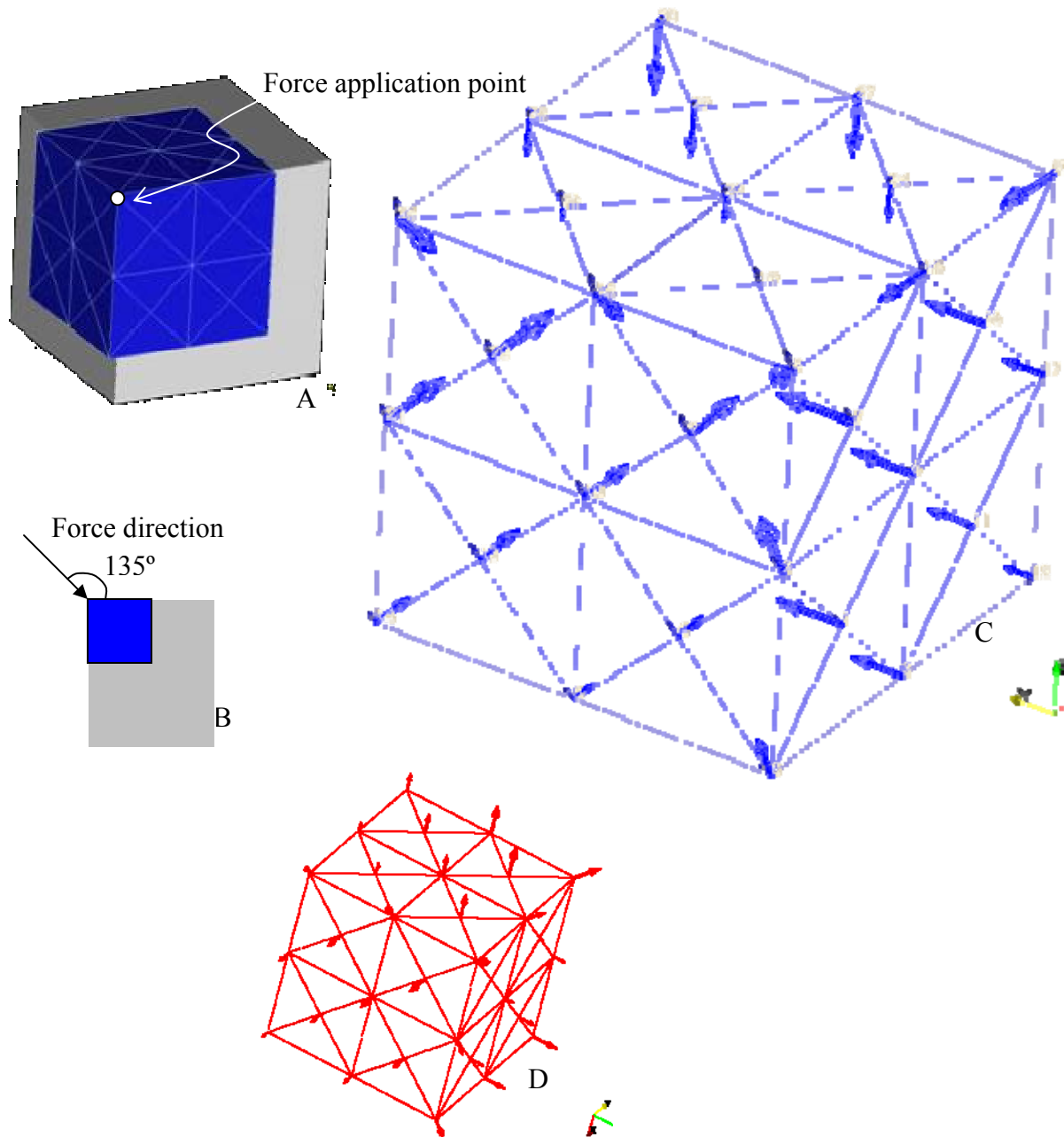


Figure 5-5. A corner frame that was used to validate the program. A) The corner frame is shown on blue and the white dot signifies the location of the force. B) The direction of the force is the normal located at  $135^\circ$  from all three sides of the corner. C) The wireframe arrows show a scaled normal displacement vector for all nodes on the frame, and the small solid arrows show the displacement vector at each node. D) The force application in the opposite direction results in all normal displacements in the opposite direction to C.

## CHAPTER 6 RESULTS AND DISCUSSION

A set of criteria were developed that showed that all large masks were found to be stable and all small masks were not stable. Also, the cap-like reference frame and the half sphere surfaces were found to be not stable.

In reality, all masks maintained stability when loaded in the direction and location of each mask's main normal ( $\mathbf{N}_{\text{main}}$ ). In reality the conforming surfaces of all small masks do not have a unique fit, meaning that there is not one unique location where the mask fits, rather there are various locations where it could fit (Figures 6-1B, 6-2B and 6-3B). The small masks were designed with the expectation that they will not have a unique fit, for the purpose of validating the methodology. For all large masks there is a unique fit (Figures 6-1A, 6-2A and 6-3A). All large masks can withstand real lateral forces or forces  $90^\circ$  from their main normal ( $\mathbf{N}_{\text{main}}$ ). The Asian small mask is the only small mask that can sustain contact stability when a real load is applied at large angles from its main normal (about  $60^\circ$  from  $\mathbf{N}_{\text{main}}$ ); it is the only small mask that extends laterally along the entire superciliary arches (Figure 6-2B). It also extends caudally onto the nasion and sits onto the upper orbital area. The small Caucasian mask does not extend onto the orbital area and does not extend onto the nasion (Figure 6-1A). The small infant mask extends laterally along the superciliary arches but it does not reach over the nasion (Figure 6-3B).

The facial angles of all three anatomical models were measured as defined by Figure 2-11; the results are shown in Table 6-1. One can appreciate that stability could be sustained if the nasiolateral and nasiofrontal angles are relatively small and if the nasiofacial angle is large. With smaller nasiolateral and nasiofrontal angles there is more opposing contact area to lateral forces

(90° from the  $N_{\text{main}}$ ). The Caucasian model has the smaller nasiolateral angle, and the second smallest nasiofrontal angle and the largest nasiofacial angle (Table 6-1).

For the simulation results, two types of graphs were produced, a) a color coded surface plot of the masks onto the solid models (Figure 6-5 to 6-9) and b) a normalized histogram for the box ratios for all values of  $\rho$  ( $\rho = 0^\circ$  to  $360^\circ$ ), for each tilt angle ( $\theta$ ) (Figure 5-12) accumulated over all points (Figure 6-10 to 6-17).

In the case of the surface models, the results are presented for each force application point where the color signifies the maximum tilt angle for which stability was found (based on the single-point and single stability criteria) for a full rotation ( $\rho = 0^\circ$  to  $360^\circ$ ). At each color coded point on Figure 6-5 and 6-9, a set of 49 force vectors were applied. For each force vector all springs that comprised the bed of springs were evaluated for stability. At each spring the maximum angular force (for a full rotation  $\rho = 0^\circ$  to  $360^\circ$ ), the furthest from the main normal ( $N_{\text{main}}$ ), at which at least 3 springs were found in compression was noted. This maximum angle is color coded in Figures 6-5 to 6-9. If the frame was found stable at every force application it will be indicated in red, demonstrating that for any force between  $\theta$  equal to  $0^\circ$  and  $\theta$  equal to  $90^\circ$ , the mask did not slide or tilt beyond the criteria established ( $TNT \geq 0.7$ ). Some masks (small unstable masks) experienced some tangential movement or rotation, so they only exhibit stability at a lesser angle (i.e.  $\theta = 45^\circ$  from the main normal).

For the box ratio histogram plots, the results are presented as frequency of the box ratio by individual tilt angle ( $\theta$  or  $\theta$ ) for all  $\rho$  values over all points on the mask (Figures 6-10 to 6-17). For example, in Figure 6-10 for the Caucasian large mask, for a tilt angle of  $0^\circ$ , 30% of the box ratios are equal to 0.4.

For the Caucasian large mask (Figure 6-5A), the surface plot shows that all non-edge points sustain stability for a maximum theta of 90° and for all rotations about the  $N_{main}$  ( $\rho = 0^\circ$  to 360°); while the small Caucasian mask's design did not sustain contact for any full rotation for any point (Figure 6-5B).

For the Asian large mask (Figure 6-6A) and for the infant large mask (Figure 6-7A), the surface plots show similar results to the large Caucasian mask (Figure 6-5A), all points sustained stability all the way to a tilt angle of 90°. It is important to notice that fewer forces were applied on the large Asian and large infant masks because there are less non-edge points (Figures 6-6 and 6-7).

The surface plot for the small Asian mask shows more stability per location than any other small mask. This mask extends along the superciliary arches and sits on top of the upper orbital area and extends caudally past the naision area providing a surface to judge correct alignment. The color coded surface plot for the small Asian mask agrees with the design as they show stability along the left lateral side and over the upper orbital area. On the right side less stability was found simply because the mask is not symmetric and includes less coverage over the right upper orbital area.

The color coded surface plot for the small infant mask shows some point locations where the tilt angle theta sustains stability up to 60° (Figure 6-7). This is due to the mask extending over the upper orbital area and laterally along the superciliary arches.

The single force criterion states that three points need to be in compression as defined by the single point criteria (with a TNT ratio of 0.70 or below) to have stability at a particular force. As mentioned before, if 3 or more “good compressor” springs are found, then the compression patch volume ( $c_{vol}$ ) is different than zero and the box ratio results in a value greater than zero and

less than or equal to one (Figure 4-19). The level of stability is the highest when the box ratio is close to 1, since this indicates that the volume of the compression patch ( $c_{vol}$ ) is similar to the volume of the entire frame ( $f_{vol}$ ).

The box ratio histograms for the small Caucasian mask (Figure 6-10) shows highest frequencies at box ratio equal to zero, this means that for most external force applications the mask was found unstable (from the single force criterion). These results correspond to the surface plot results in Figure 6-5B.

The box ratio histogram for the small Asian mask shows a range of box ratios between 0.0 and 0.55, with most frequencies (70%) at box ratios of 0.15 (Figure 6-13), this means that when stability was found the compression patch volume ( $c_{vol}$ ) was small. However, for all theta values there are frequencies where the box ratio is equal to zero, this means that even though stability was found in most of the cases, there were always instances where the mask lost stability. This results are harder to relate to the surface color maps, because as mentioned before, the surface color map show stability per location, and the box ratio histograms show stability by accumulating all forces for a particular theta value over all rotations. The infant small mask sustained stability for theta equal to  $0^\circ$ , but had no stability for all other angles (Figure 6-15). At theta equal to  $90^\circ$ , 80% of the of the box ratios are equal to zero, which signifies a high level of instability for forces applied at  $90^\circ$  from the main normal.

The box ratio histograms for the large Caucasian mask shows no instability (zero frequency for box ratios equal to zero), and the box ratios range between 0.25 and 0.95 (Figure 6-10). As the theta angle (tilt angle from the  $N_{main}$ ) increases the box ratios decreases, showing that at higher angles the compression patch volume is smaller. Similar box ratio histogram results can be seen for the Asian large mask (Figure 6-12) and the infant large mask (Figure 6-

14) where there is no instability or zero frequency for box ratios equal to zero. However, for the large Asian mask the box ratios are skewed to the left, they range from 0.25 to 0.65 (Figure 6-12). This means that for the large Asian mask, increasing theta values result in smaller compression patch volumes ( $c_{vol}$ ) than for the large Caucasian mask.

For the large infant mask the results follow the same pattern, increasing the tilt angle of the external force results in decreasing box ratios (Figure 6-14). The range for the large infant mask is from 0.15 to 0.75, this is a slightly larger box ratios range than for the box ratio range for the large Asian mask (0.25 to 0.65) (Figure 6-12).

Based on the facial angle measurements in Figure 2-11 and on the premise that the more pronounced facial features result in more stable masks, the ideal angle combination for a stable mask will be small nasiolateral and nasiofrontal angles and large nasiofacial angles. Out of the three large masks, the Caucasian mask corresponds to a model with the smaller nasiolateral angle and the second smallest nasiofrontal angle and the largest nasiofacial angle. In addition, the box ratio range for the Caucasian mask is the largest (0.25 to 0.95) when compared to the Asian (0.25 to 0.65) and infant (0.15 to 0.75). Figure 6-13 shows a profile view of all three models. The infant large mask corresponds to a model with the smallest nasiofrontal angle and the second smallest nasiolateral angle, but the smallest nasiofacial angle. The infant model has the smallest nasiofrontal angle due to a curvature on the forehead as can be seen in Figure 6-18C. It is likely that this pronounced curvature is responsible for the infant large mask having the second highest box ratios ranging between 0.15 and 0.75.

In addition to the mask reference frames, a cap-like reference frame (Figure 6-8B) and a half sphere surface (Figure 6-9) were evaluated with the methodology for testing the uniqueness of fit. In reality the cap-like frame has an uncertain fit, in other words, it was difficult to find the

location where it was designed to fit. The color coded surface plot results for the cap-like reference frame shows that the frame sustains stability (as defined by the single point and single force criteria) all the way to a maximum theta value of  $90^\circ$  when forces are applied on the upper most cephalic region. However, forces no greater than  $60^\circ$  were sustained at the coronal and sagittal extensions of the frame (Figure 6-8). The box ratio histogram (Figure 6-16) for the cap-like frame corresponds with the information on the surface plots. The box ratio histogram shows that some level of stability was found for all theta angles, but it was not sustained through out the entire surface, since about 5% of the box ratio show instability for all tilt angles. The remaining box ratios (about 70%) have values of 0.15, which signifies that the compression patch volume ( $c_{vol}$ ) was small compared to the volume of the entire mask ( $f_{vol}$ ) for the instances where stability was found.

In the case of the half-sphere surface (Figure 6-9), the surface plot shows that there were no locations where the surface sustained any force, possibility not even in the direction of the normal force ( $N_{main}$ ). The box ratio histogram for the half sphere test shows that stability was indeed found for all angles (there are box ratios between 0.0 and 0.35); however, for the majority of the cases (60% to 80% frequency) no stability was found or the box ratio equaled the value of zero.

In summary, Table 6-2 shows the instability scores for all masks and frames as defined in Equation 4-8. There is zero percent instability for all large masks and there is some percentage of instability for all small masks, the cap-like frame and the half-sphere surface, as was expected. The least stable case is the half-sphere test, with a instability score of 94%, this high percentage instability make sense because the surface has no irregularities to oppose any external forces (besides in the main normal direction). The small Asian mask was the mask with the smallest

instability score at 5%, as was mentioned previously; this is due to the design of the mask that includes the upper orbital area on one side and extends the furthest medially and laterally along the superciliary arches. This results correlate well with the color coded surface plots, were stability was found in the left upper orbital region on the mask.

Table 6-1. Measurement of the facial angles for the three anatomical models.

| Model     | Nasiolateral angle | Nasiofrontal angle | Nasiofacial angle |
|-----------|--------------------|--------------------|-------------------|
| Caucasian | 89°                | 116°               | 40°               |
| Asian     | 123°               | 124°               | 29°               |
| Infant    | 104°               | 106°               | 23°               |

Table 6-2. Instability score, presented as the percentage of forces that resulted in instability and the total forces applied on a frame.

| Frame                | Total Number of forces applied | Total Number of forces applied | Percentage |
|----------------------|--------------------------------|--------------------------------|------------|
| Large Caucasian mask | 4935                           | 0                              | 0%         |
| Large Asian mask     | 1575                           | 0                              | 0%         |
| Large infant mask    | 1702                           | 0                              | 0%         |
| Small Caucasian mask | 874                            | 602                            | 69%        |
| Small Asian mask     | 1755                           | 88                             | 5%         |
| Small infant mask    | 874                            | 334                            | 38%        |
| Cap-like frame       | 2695                           | 241                            | 9%         |
| Half-sphere test     | 1094                           | 975                            | 94%        |

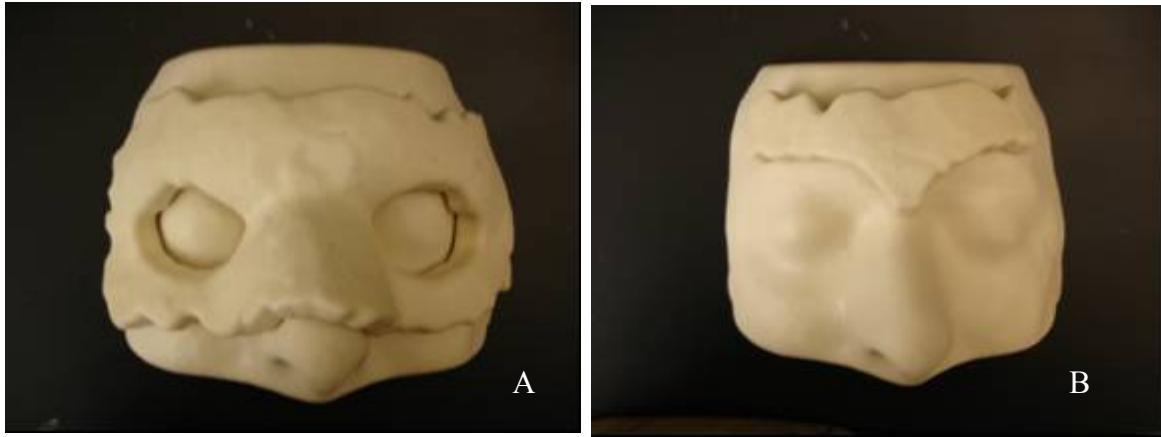


Figure 6-1. Placement of Caucasian masks onto solid model. A) Large Mask. B) Small Mask.

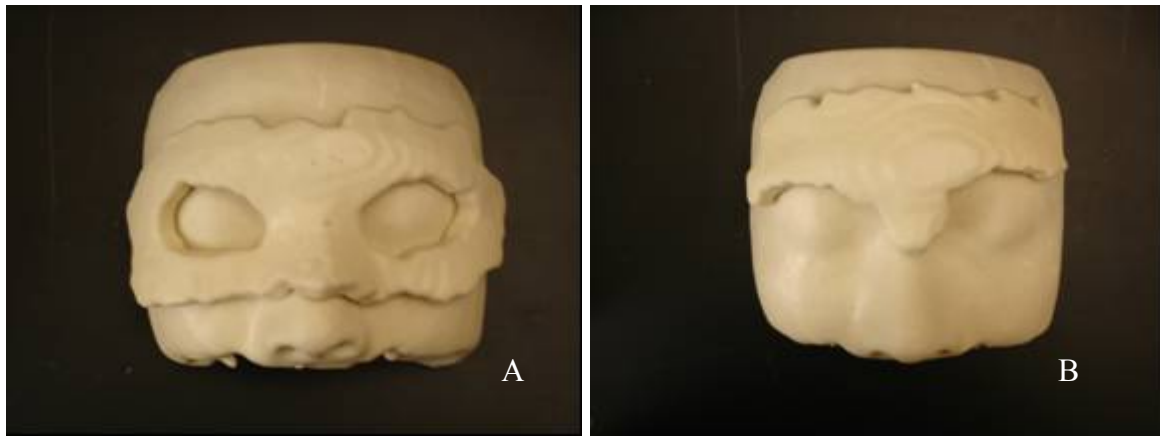


Figure 6-2. Placement of Asian masks onto solid model. A) Large Mask. B) Small Mask.

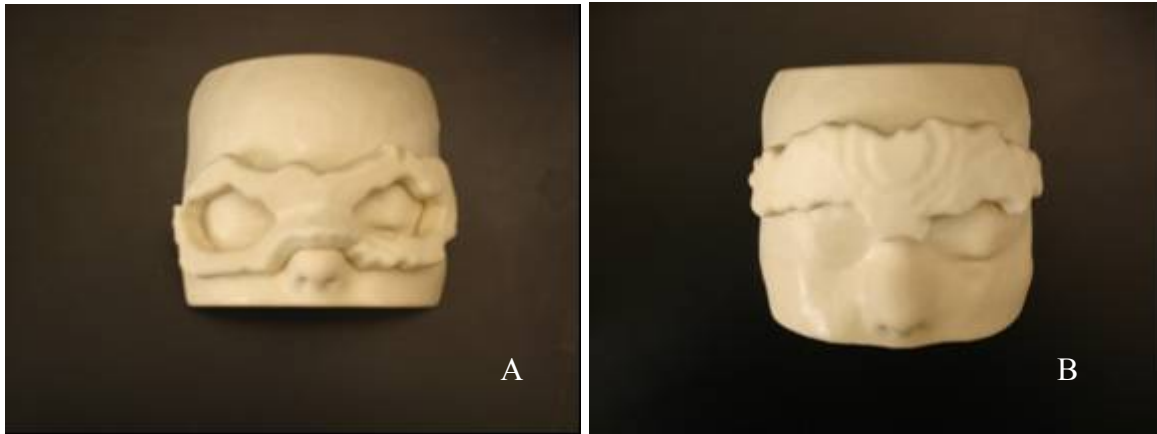


Figure 6-3. Placement of infant masks onto solid model. A) Large Mask. B) Small Mask.

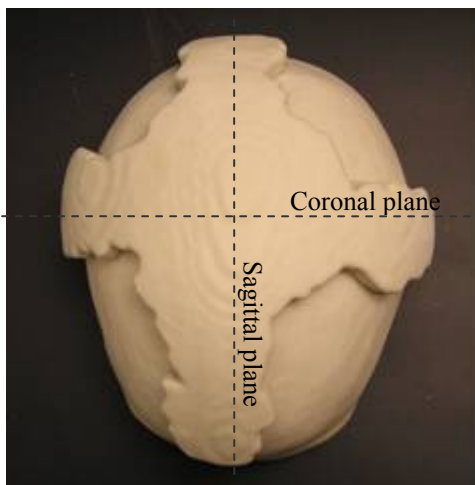


Figure 6-4. Placement of a cap-like reference frame onto an upper head model.

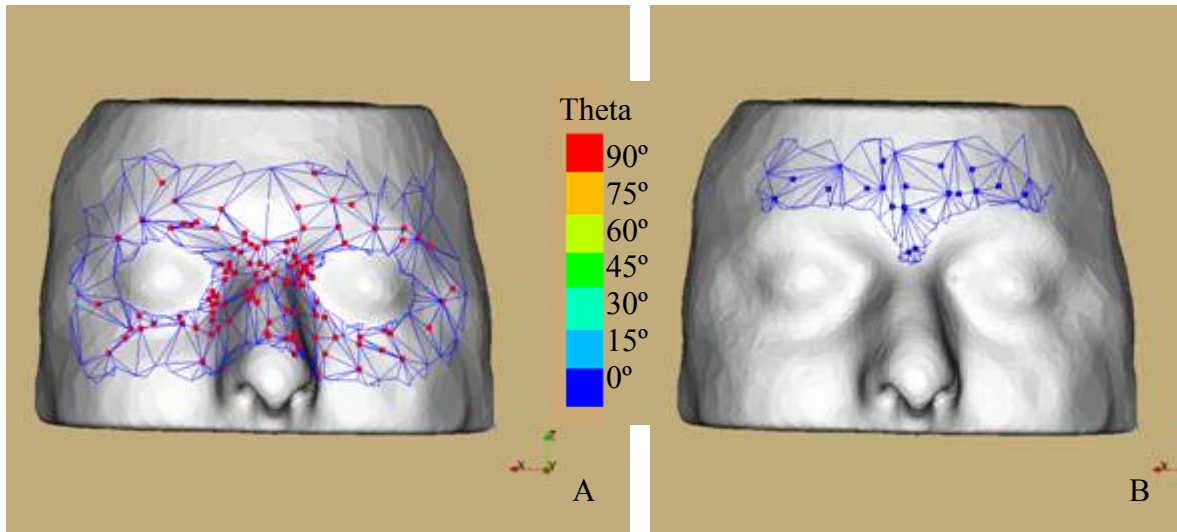


Figure 6-5. Surface plot color coded by the maximum full rotation angle for the Caucasian masks. A) Large Mask. B) Small Mask.

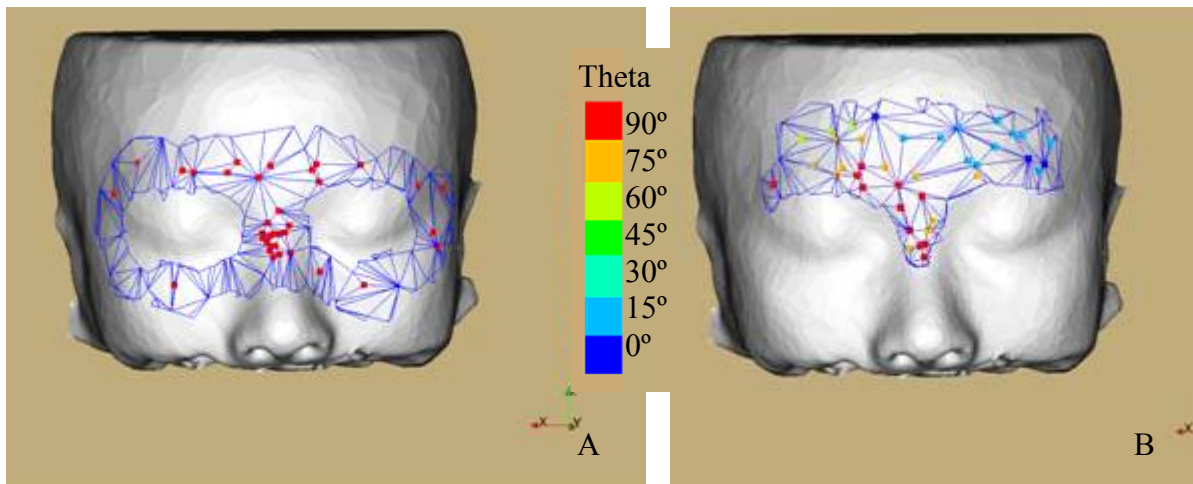


Figure 6-6. Surface plot color coded by the maximum full rotation angle for the Asian masks. A) Large Mask. B) Small Mask.

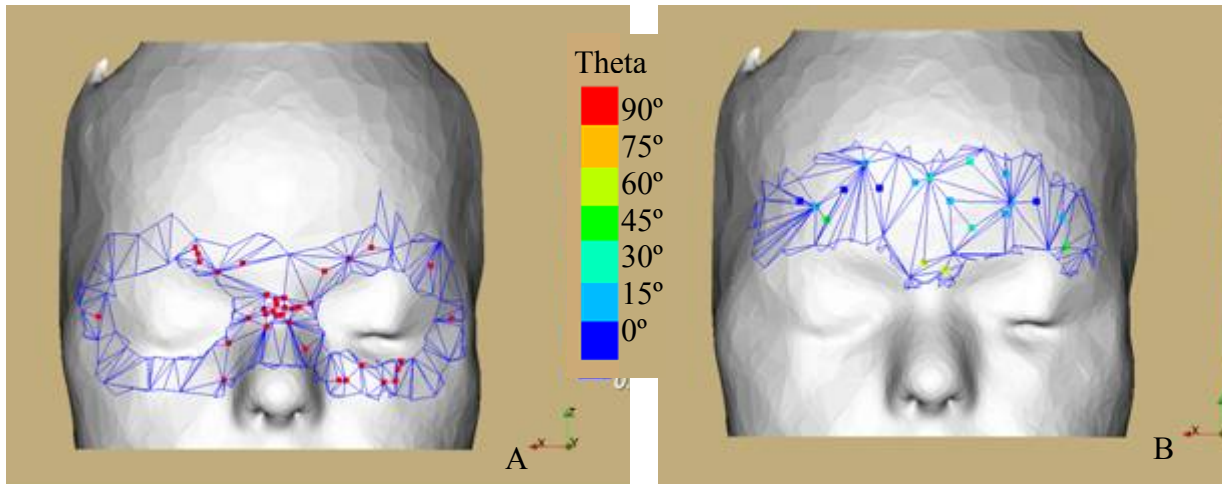


Figure 6-7. Surface plot color coded by the maximum tilt angle for the infant masks. A) Large Mask. B) Small Mask.

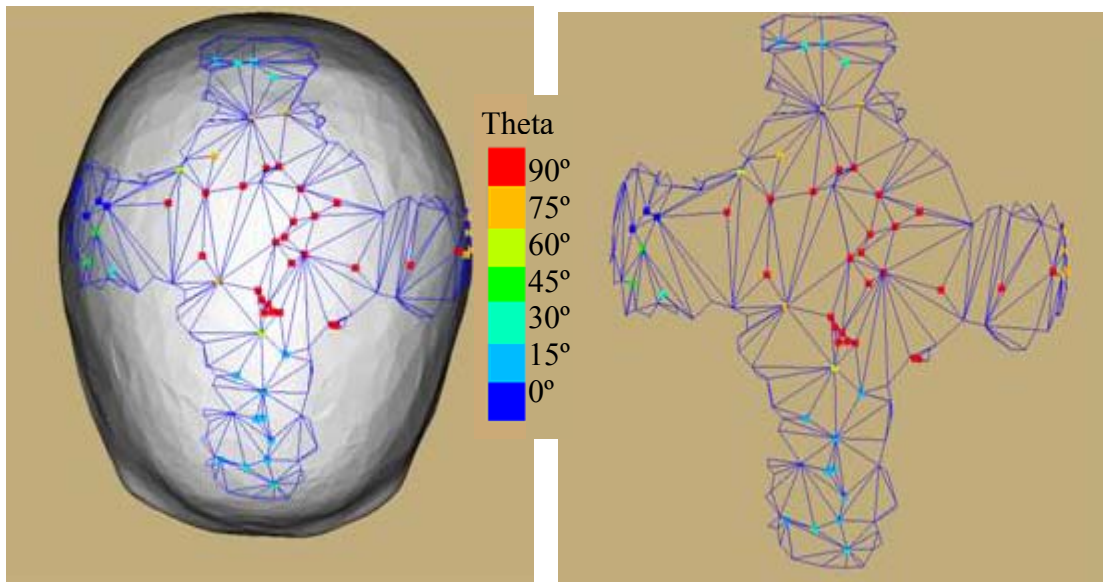


Figure 6-8. Surface plot color coded by maximum tilt angle for the cap reference frame design

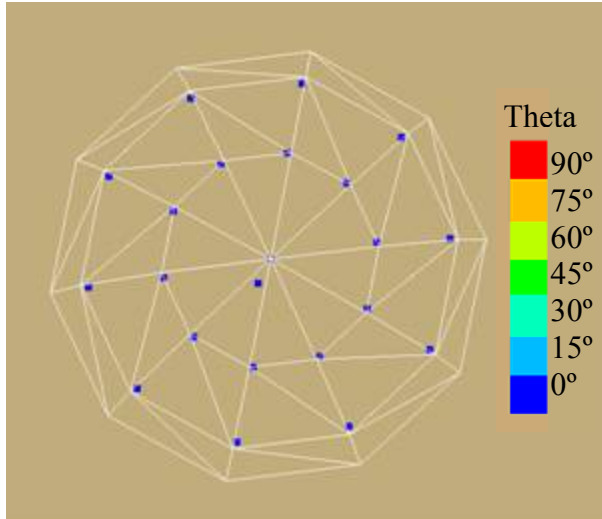


Figure 6-9. Surface plots color coded by maximum tilt angle for the half sphere test.

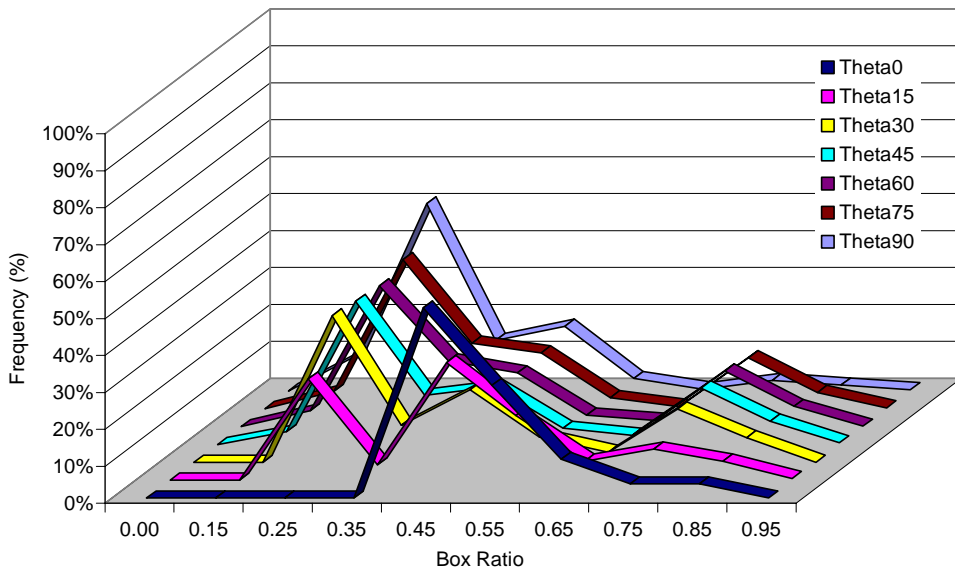


Figure 6-10. Normalized histogram of box ratios for each tilt angle ( $\theta$ ) for the Caucasian large mask.

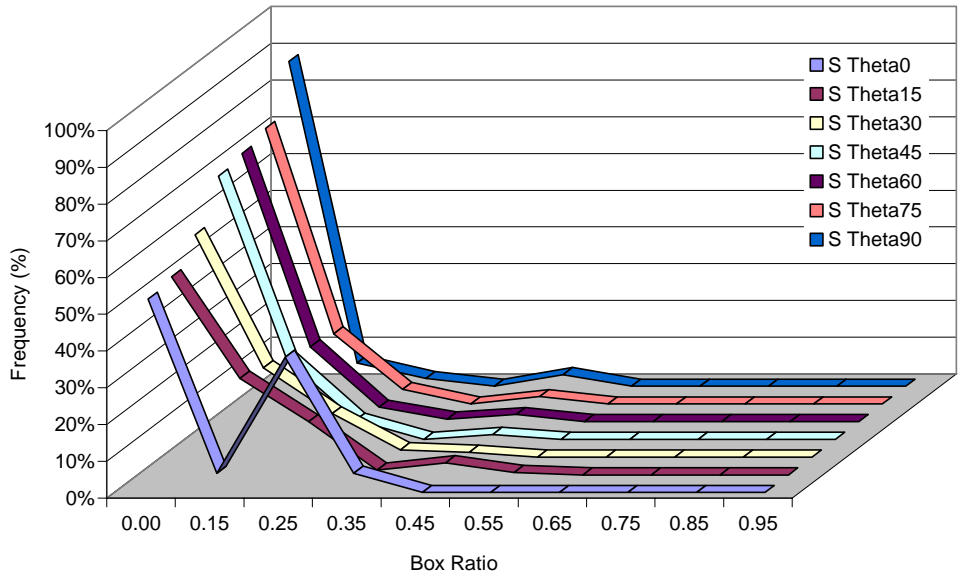


Figure 6-11. Normalized histogram of box ratios for each tilt angle ( $\theta$ ) for the Caucasian small mask.

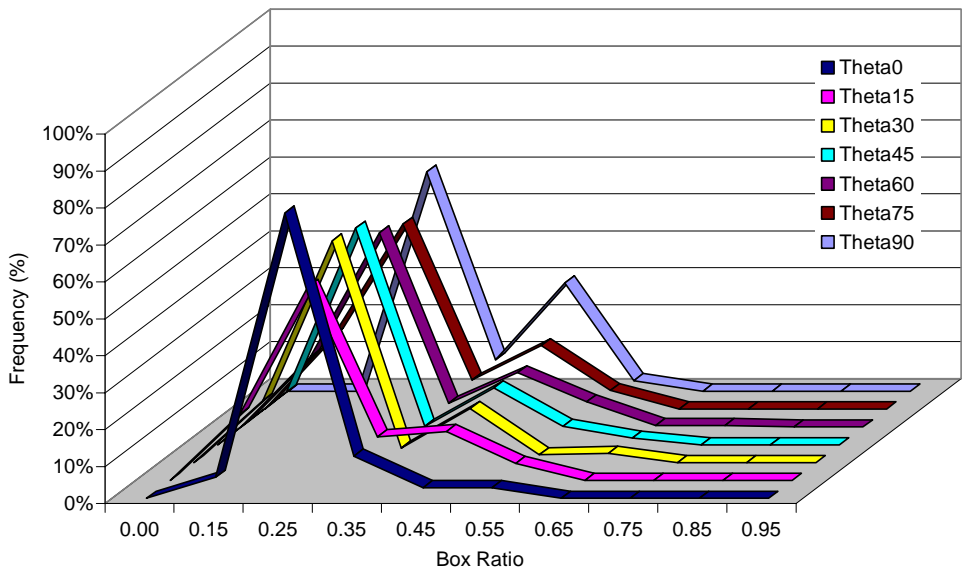


Figure 6-12. Normalized histogram of box ratios for each tilt angle ( $\theta$ ) for the Asian large mask.

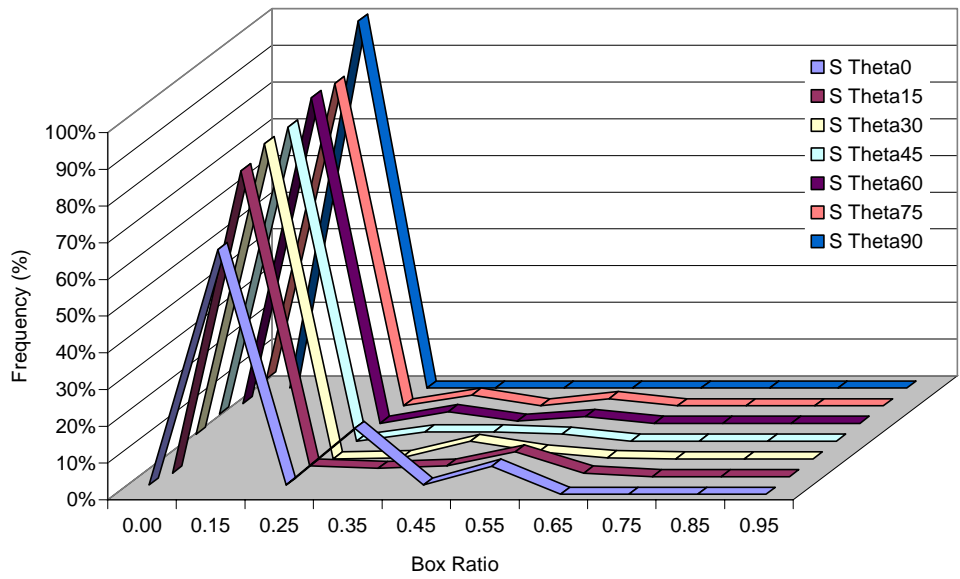


Figure 6-13. Normalized histogram of box ratios for each tilt angle ( $\theta$ ) for the Asian small mask.

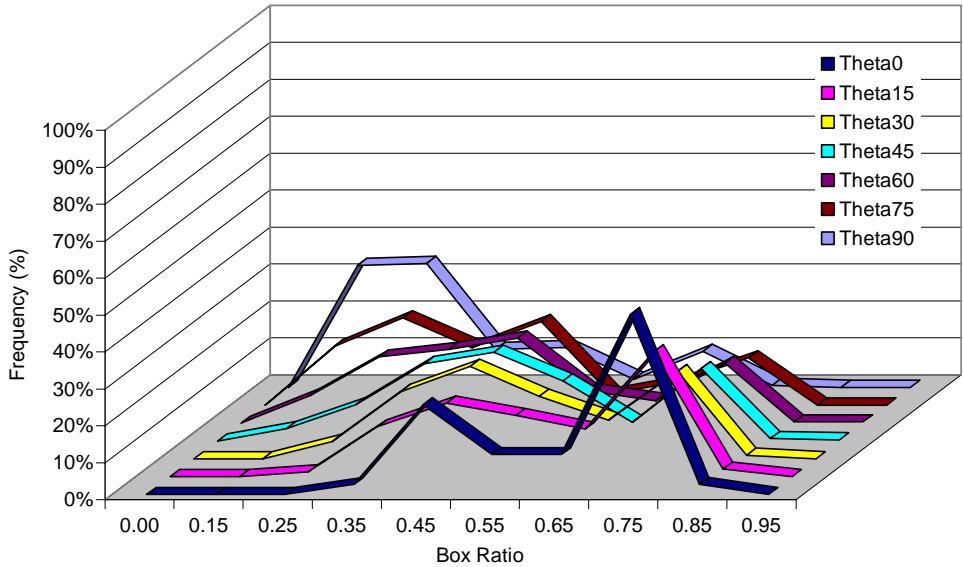


Figure 6-14. Normalized histogram of box ratios for each tilt angle ( $\theta$ ) for the infant large mask.

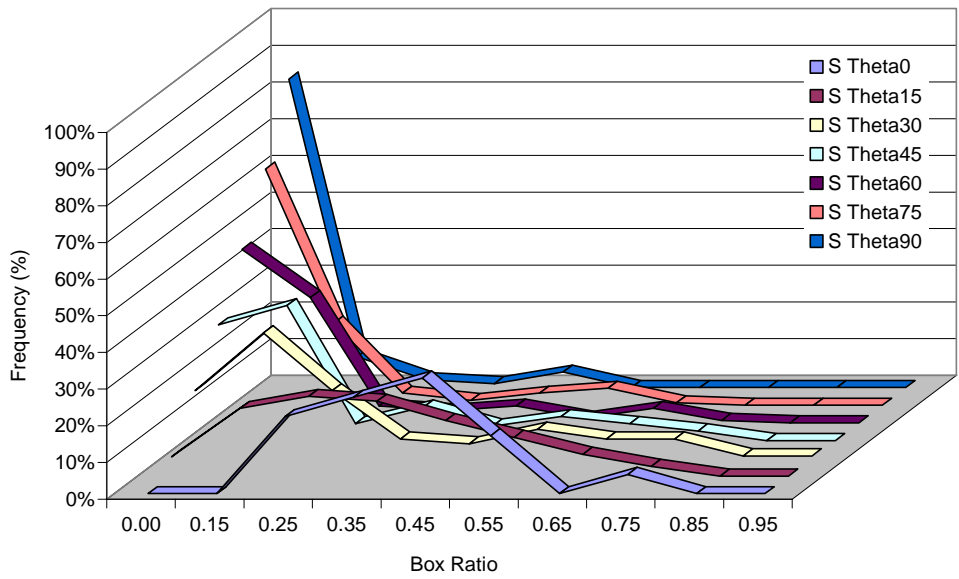


Figure 6-15. Normalized histogram of box ratios for each tilt angle ( $\theta$ ) for the infant small mask.

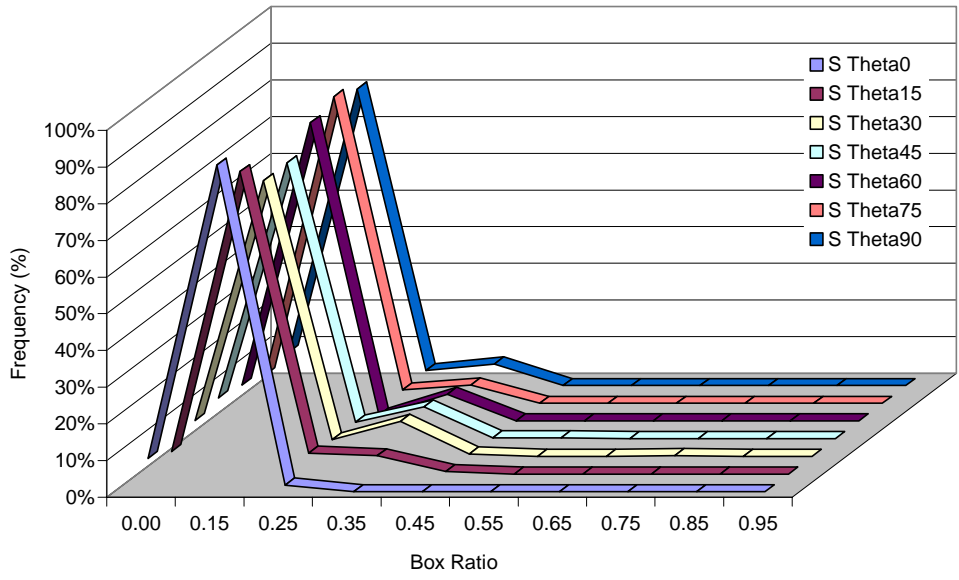


Figure 6-16. Normalized histogram of box ratios for each tilt angle ( $\theta$ ) for the cap reference frame design.

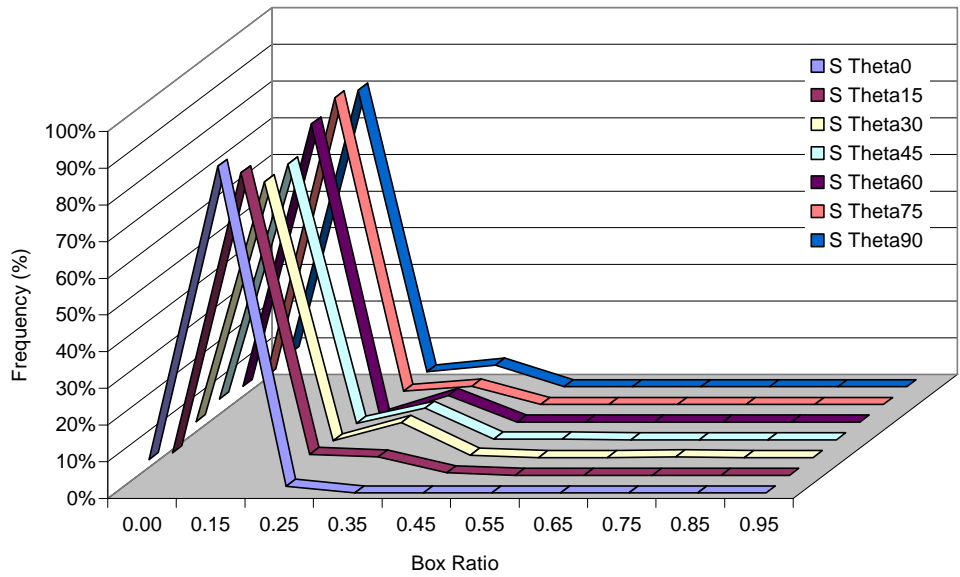


Figure 6-17. Normalized histogram of box ratios for each tilt angle ( $\theta$ ) for the half sphere test.

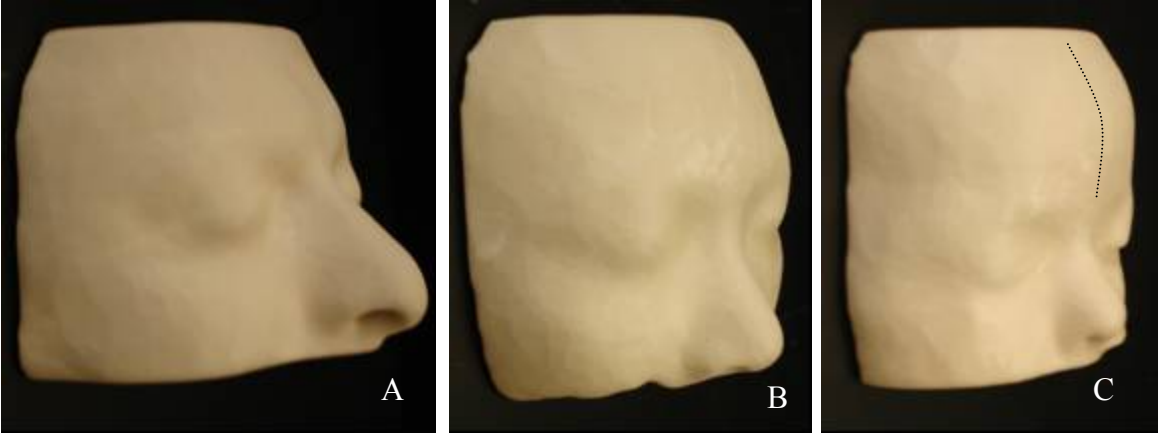


Figure 6-18. Profiles of solid models. A) Caucasian. B) Asian. C) Infant.

## CHAPTER 7 CONCLUSION AND FUTURE WORK

The results have determined a clear difference in stability of fit between the large masks and the small masks for all cases. Both the surface plots and the box ratio histograms show that the large masks are stable while the small masks are not. Furthermore, the surface plots are able to show which force location points and what angles result in an unstable fit. The box ratio histograms are able to quantify stability on a tilt angle basis; by assigning a normalized numerical value to the magnitude of the contact volume, if three compression points are present that satisfy the TNT threshold. In addition, the box ratio histograms are able to provide information about the maximum tilt angle ( $\theta$ ) that the entire mask can withstand over all rotations about the main mask normal.

The two additional cases, the cap-like reference frame and the half sphere surface have further validated the program by providing expected results when compared to predicted real-space frame movements. Furthermore, these two additional surfaces have shown that the surround coverage of the head does not particularly results in stability, and hints that the facial landmarks are the best locations to uniquely fit a mask reference frame onto a patient.

The training data was compared to the three models' facial landmarks and motivating relations about stability and facial angles were found, which suggests that if masks are built for patients with small nasiolateral and nasiofrontal angles and large nasiofacial angles, their masks may be highly stable.

In the future more masks should be tested with the parameters defined in the methodology. Also it could be worth while to measure the facial angles of more patients and run statistical analysis to compare the relations between facial angles and stability as measured by the methodology defined in this investigation. Concerning the program, a meshing filter could be

beneficial for regularly meshes the surfaces. Also the box ratio definition could be redefined for easy understanding, by simply calculating the compression patch volume ( $c_{vol}$ ) divided by the entire frame volume ( $f_{vol}$ ), this will result in values from zero to one, in which zero signifies instability and one signifies full stability.

The present investigation has provided with a methodology for testing uniqueness of fit for the patient-specific reference frames that improves the new and promising technology to perform image-guided surgery. The methodology will provide the clinician with prior information of frame-on-patient stability, which was not available before and is essential for allowing the clinician to effectuate his surgical plan with more confidence and accuracy. In addition the methodology was created using an open source image analysis software (ITK and VTK), and by doing so, it will be easily adapted to the already existing user interface (RPD designer also was created with ITK and VTK), which allows the surgeon to create his/her own reference frames based on diagnostic images. By including the stability measuring module in the already existing graphical user interface (RPD designer), the new technology for image-guided surgery will be more robust and a step closer towards being introduced to other medical communities.

## APPENDIX A PRINCIPLE OF VIRTUAL WORK AND ITK FEM MODULE

This section provides additional background information related to the finite element method (FEM) for two main reasons. The methodology for testing the stability of fit of the patient-specific frames is based on FEM and the tools used for performing the FEM lack documentation. This chapter first provides background information on FEM, and then uses the direct stiffness method to explain the basic steps to derive the element stiffness matrix for a 2-dimensional truss element. It also comments on the principles of virtual work because the ITK FEM module (ITK 1.8, Kitware Inc., Clifton Park, NY) follows them to arrive to one of the element's stiffness matrices used in this investigation. Finally it discusses the ITK FEM module and its organization in an attempt to supplement for the currently available documentation.

### **FEM Terminology for Truss Elements**

There is a specific technical terminology associated with FEM. The following list [4,28,46] presents the main components involved in FEM as it relates to structural analysis and will aid in the understanding of the subsequent sections.

- **Discretization:** The process of subdividing a structures into members or finite elements with the purpose of modeling, simulating, or approximating their mechanical behavior under known forces.
- **Elements:** In the case of structure analysis, an element is a single member of a structure. Its contribution to the structure is defined by a force-displacement relationship and this relationship is used to analyze the element.
- **Node:** The purpose of the node is to connect elements, it is assumed to be infinitesimally small in size and therefore frictionless. Depending on the structure or part simulated the nodes can behave differently. For example, a node will act as a frictionless hinge in 2-dimensional truss elements, and as a frictionless ball-and socket in 3-dimensional truss elements.
- **Global and Local Coordinates:** In FEM, usually two coordinate systems are used. One is referred as the global coordinate system (X, Y, and Z) and it describes the overall geometry and load-deformation relation of the entire structure. The other is referred as a local coordinate system (x, y and z) and it describes the force-displacement relations for each

individual element. In the case of the truss element, the local coordinate system's origin is located at one end of the truss element and the local x-axis is oriented along the axis of the element.

- **Degrees of Freedom (DOF):** Degrees of freedom represent node displacements, such as translations and rotations. When a structure is subjected to an external load, the degrees of freedom are the independent node displacements necessary to indicate the deformed shape of the structure. A 1-dimensional truss element has 1 DOF per node, a 2-dimensional truss element has 2 DOF per node and a space truss has 3 DOF per node. For truss elements the nodes are assumed to be frictionless joints, so the elements are not subjected to moments, and the rotations are zero.
- **Boundary Conditions (BC):** Boundary conditions are applied at nodes to fix the model in space or to set a prescribed displacement onto the nodes. In a structural model, they represent fixed supports necessary to remove the rigid body motion of a structure. In addition, when the boundary conditions are set correctly, the total number of unknowns must be equal to, or smaller than, the number of equation necessary to describe the model under known loading conditions [4].
- **External forces and internal forces:** External forces are specified in global coordinates and internal forces are specified in local coordinates. Local coordinates are induced onto elements by external forces. For example, an external force is applied on a particular node on a structure, as a result the elements that compose the structure will deform and internal forces will be induced at each individual element's node.
- **Material Properties:** Material properties define elastic characteristics of the elements. For simple truss elements they are the elastic modulus  $E$  (MPa), and the Poisson ratio  $\nu$  [3].
- **Transformation Matrices ( $\mathbf{T}$ ):** For simplification, the integration of the element is performed in local coordinates. A transformation matrix is need that allows the transition from local to global (and vice versa) coordinates. It involves the direction cosines of the local coordinate system in the global coordinate system.
- **Element Stiffness Matrices ( $\mathbf{k}^e$ ):** The stiffness matrix of an element relates the local forces to the local nodes' displacement. The element stiffness matrix is composed of stiffness coefficients. The stiffness coefficient denoted  $k_{ij}$  is explained as the force in the  $i$  direction required to cause a displacement at node  $j$  while all other node displacements are zero [4].

### **Principle of Virtual Work**

In the FEM the force-displacement relations can be derived from the work-energy principles; the main reason for this being that by using work-energy principles the force-displacement relations can be conveniently applied to solid elements. The principle for virtual work for rigid bodies states [4].

If a rigid body, which is in equilibrium under a system of forces (and couples), is subjected to any small virtual rigid-body displacement, the virtual work done by the external forces (and couples) is zero.

A virtual displacement is simply a small imaginary displacement. The principle of virtual work for rigid bodies implies that if the rigid body is in equilibrium, then the sum of forces and moments must add to zero, thereby causing the virtual work,  $\delta W_e$ , to be equal to zero, or  $\delta W_e =$

0. The principle for virtual work for deformable solids state [4].

If a deformable structure, which is in equilibrium under a system of forces (and couples), is subjected to any small virtual displacement consistent with the support and continuity conditions of the structure, then the virtual external work done by the real external force (and couples) acting through the virtual external displacements (and rotations) is equal to the virtual strain energy stored in the structure.

The principle mentioned above implies that virtual external work is equal to virtual internal work, and since internal work is equal to the structure strain energy then  $\delta W_e = \delta U$ .

In this investigation we are using only linear elements. FEM linear analysis follows two basic assumptions [4].

- The part or model is simulated with a linear elastic material, this means that the strain-stress relations behave in a linear manner and follow Hooke's Law, which states that the stress  $\sigma$  (MPa) is proportionally related to the strain  $\epsilon$  (unitless), by the elastic modulus of the material denoted as  $E$  (MPa), or  $\sigma = E\epsilon$ .
- The model experiences deformations that are infinitesimally small; therefore the squares and higher powers of the element's deformed shapes are negligible in comparison to unity. Indeed, the equation of equilibrium can be based on the non deformed geometry of the part.

### **ITK FEM and Principles of Virtual Work**

The following section is based on information from the ITK libraries [24], Aslam et al. [4] and Felippa et al. [17, 18] and has the purpose of providing background information on how the ITK FEM module sets up the element stiffness matrix, because the module lacks explanations and clear documentations.

The ITK FEM module follows principles of virtual work to generate the element stiffness matrix in local coordinates. The ITK FEM module requires 1) the definition of the shape functions for each element types, 2) the derivation of the shape functions (strain displacement matrix) and 3) values related to the numerical integration of the element stiffness matrix.

To get a brief idea of how these components relate to the principles of virtual work first consider a 3-dimensional differential element in equilibrium and subjected to loading (Figure A-1). Following the principle of virtual work for deformable solid bodies [4], the loading on the differential element results in real stresses ( $\sigma$ ), which cause in virtual strains ( $\delta\epsilon$ ) and internal forces that perform virtual work.

$$\delta\epsilon = \begin{bmatrix} \delta\epsilon_x \\ \delta\epsilon_y \\ \delta\epsilon_z \\ \delta\gamma_{xy} \\ \delta\gamma_{yz} \\ \delta\gamma_{zx} \end{bmatrix} \quad \sigma = \begin{bmatrix} \sigma_x \\ \sigma_y \\ \sigma_z \\ \tau_{xy} \\ \tau_{yz} \\ \tau_{zx} \end{bmatrix} \quad (\text{A-1})$$

Equation A-1 shows the notation for the stresses ( $\sigma$  and  $\tau$ ) and virtual strain that define the differential element under loading and in equilibrium. The total virtual internal work (or virtual strain energy) stored in the element can be measured by integrating over the volume [4], as shown in Equation A-2.

$$\delta W_e = \int_V (\delta\epsilon_x \sigma_x + \delta\epsilon_y \sigma_y + \delta\epsilon_z \sigma_z + \delta\gamma_{xy} \tau_{xy} + \delta\gamma_{yz} \tau_{yz} + \delta\gamma_{zx} \tau_{zx}) dV \quad (\text{A-2})$$

$$\delta W_e = \int_v \delta\epsilon^T \sigma dV \quad (\text{A-3})$$

Equation A-2 and Equation A-3 (compressed formed) defines the principle of virtual work for deformable bodies expressed in terms of stresses ( $\sigma$ ) and virtual strains ( $\delta\epsilon$ ), they represent the virtual strain energy stored in the element.

Now the focus becomes defining the local element stiffness matrix  $\mathbf{k}^e$ , in terms of stresses and strain using principles of virtual work of deformable bodies. The first step is to define the node displacements in terms of stresses and strains.

### Displacement Functions

The node displacement for a truss element can be represented by a displacement function with the form of a linear polynomial (Equation A-4) [11]. The displacement function or displacement variation  $\bar{u}(x)$  needs to be defined solemnly along the local x-axis.

$$\bar{u}(x) = a_0 + a_1x \quad (\text{A-4})$$

The roots of the polynomial,  $a_0$  and  $a_1$ , are constants and must satisfy the boundary conditions, that is the displacement conditions at the nodes [11]. From Figure 2-1, when  $x$  is equal to 0 (at the origin of the local coordinate system), the displacement variation function  $\bar{u}(x)$  is equal to  $u_1$ .

$$\bar{u}(0) = u_1 = a_0 \quad (\text{A-5})$$

In the same way, when  $x$  is equal to  $L$ ,  $\bar{u}(x)$  is equal to  $u_2$ .

$$\bar{u}(L) = u_2 = a_0 + a_1L \quad (\text{A-6})$$

The displacement variations of the truss element in terms of node displacements,  $u_1$  and  $u_2$  can be calculated by substituting Equation A-5 and A-6 into A-4 and rearranging to yield Equation A-7 [11].

$$\bar{u}(x) = \left(1 - \frac{x}{L}\right)u_1 + \left(\frac{x}{L}\right)u_2 \quad (\text{A-7})$$

### Shape Functions

The displacement function (Equation A-7) can be alternatively expressed as shape functions. There are as many shape functions for an element as there are nodes, and they have

the characteristic of having a value of one at its corresponding node ( $N_1$  has a value of one at node 1) and a value of zero at the other node points [3]. For a truss element there are two shape functions denoted by  $N_1$  and  $N_2$ . The roots of the polynomials in Equation A-7 represent the shape functions (Equation A-8).

$$N_1 = \left(1 - \frac{x}{L}\right) \quad N_2 = \left(\frac{x}{L}\right) \quad (\text{A-8})$$

For convenience the displacement variation function ( $\bar{u}(x)$ ) can be expressed in terms of shape functions and node displacements (Equation A-9). Equation A-10, is the final form of the element's displacement function (or interpolating function) and  $\mathbf{N}$  is the element's shape function matrix, and  $\mathbf{u}$  are the element's node displacements.

$$[\bar{u}_x] = [N_1 \quad N_2] \begin{bmatrix} u_1 \\ u_2 \end{bmatrix} \quad (\text{A-9})$$

$$\bar{\mathbf{u}} = \mathbf{N}\mathbf{u} \quad (\text{A-10})$$

### Strain Displacement Equation

Getting back to the aim of representing the node displacement in term of stresses and strain, Equation A-11 shows the relationship between strain ( $\varepsilon$ ) and displacement variation function ( $\bar{u}(x)$ ), for a truss element [11].

$$\varepsilon = \frac{d\bar{u}_x}{dx} \quad (\text{A-11})$$

From Equation A-11, notice that a truss element only withstand strains along the local x-axis.

$$\boldsymbol{\varepsilon} = \left[ \frac{du_x}{dx} \right] [\bar{u}_x] = \mathbf{D}\bar{\mathbf{u}} \quad (\text{A-12})$$

$\mathbf{D}$  is called the differential operator matrix [4]. At last the strain can be related to the node displacements  $\mathbf{u}$  by substituting Equation A-10 into Equation A-12.

$$\boldsymbol{\varepsilon} = \mathbf{D}\mathbf{N}\mathbf{u} = \mathbf{B}\mathbf{u} \quad (\text{A-13})$$

In order to get the strain displacement matrix,  $\mathbf{B}$ , the derivatives of the shape functions need to be calculated (Equation A-13). The node displacements do not depend on the local  $x$  direction, so they are treated as a constant, while the differentiation can be applied to shape functions  $\mathbf{N}$  and not to the node displacements  $\mathbf{u}$  [4].

Following Hooke's law, the stresses can also be related to the end displacements (Equation A-14), as required by the principle of virtual work for deformable bodies [4].

$$\boldsymbol{\sigma} = E\mathbf{B}\mathbf{u} \quad (\text{A-14})$$

So far both strains (Equation A-13) and the stresses (Equation A-14) are expressed in terms of node displacements.

### Local Element Stiffness Matrix

All the necessary information required by the ITK FEM module is now available to determine the element's stiffness matrix, with the exception of a relation between the element end forces ( $f_1$  and  $f_2$  as in Figure 3-1) and the node displacements  $\mathbf{u}$ .

When subjecting a truss element to the principles of virtual external work ( $\delta W_e$ ), the truss element will be in equilibrium and subjected to end forces. These end forces will manifest themselves as virtual end displacements ( $\delta u_1$  and  $\delta u_2$ ). Equation A-15 shows how the virtual external work can be defined in terms of virtual end displacements and end forces [4].

$$\delta W_e = f_1 \delta u_1 + f_2 \delta u_2 \quad (\text{A-15})$$

$$\delta W_e = \delta \mathbf{u}^T \mathbf{f} \quad (\text{A-16})$$

In symbolic form Equation A-16  $\delta \mathbf{u}^T$  is the transform of the virtual end displacements and  $\mathbf{f}$  is the end force vector. Equation A-16 can be substituted into Equation A-3 to get Equation A-17.

$$\delta \mathbf{u}^T \mathbf{f} = \int_v \delta \boldsymbol{\varepsilon}^T \boldsymbol{\sigma} dV \quad (\text{A-17})$$

A relation between the element stiffness matrix  $\mathbf{k}^e$  and the strain displacement matrix  $\mathbf{B}$  is finally accomplished by substituting Equations A-11 and A-12 into Equation A-17 and simplifying by canceling  $\delta \mathbf{u}^T$  (Equation A-18) [4].

$$\mathbf{f} = \left( \int_v \mathbf{B}^T E \mathbf{B} dV \right) \mathbf{u} = \mathbf{k}^e \mathbf{u} \quad (\text{A-18})$$

The element stiffness matrix  $\mathbf{k}^e$  is determined by virtual work principles as defined by Equation A-19 [4].

$$\mathbf{k}^e = \int_v \mathbf{B}^T E \mathbf{B} dV \quad (\text{A-19})$$

### Gauss Quadrature

To evaluate the integration in Equation A-18, the ITK FEM module uses a method of numerical integration called the Gauss quadrature (Equation A-20) [18].

$$\mathbf{k}^e = \sum_{i=1}^n w_i J_i \mathbf{B}_i^T E \mathbf{B}_i \quad (\text{A-20})$$

In this equation,  $n$  is the number of integration points,  $i$  is the integration point index,  $w$  is the integration weight,  $\mathbf{B}$  is the strain displacement matrix, and  $J_i$  is the jacobian determinant evaluated at the integration point. In the ITK FEM module all these parameters are necessary to define an element [18].

The determination of the element stiffness matrix is the fundamental part of the ITK FEM process; afterwards the element stiffness matrix needs to be transformed into global coordinates

and assembly into the stiffness matrix that defines the complete system [28]. In the ITK FEM module after the element stiffness matrix is constructed for a particular element and transformed into the global coordinates, the remaining steps of assembly and reduction are operations that are not element dependent. The purpose of the past section was to explain the basic of parameters in referenced to the ITK FEM module to complement for the lack of documentation.

### **ITK FEM Module**

ITK is open source software that provides data representation and algorithms for implementing image analysis, primarily segmentation and registration [24]. Its origins date back to 1999 when the US National Library of Medicine of the National Institute of Health granted a three-year contract to create an open-source registration and segmentation toolkit, later it came to be known as the Insight Toolkit or ITK. The software is written in C++ and is greatly object oriented and its organization represents a pipeline where data and process are connected together. ITK has an FEM module primarily intended to be used for image registration, but complete to perform mechanical modeling.

ITK provides an object-oriented FEM library to solve general FEM modeling. Classes are used to specify the geometry, behavior of the elements, apply external forces, apply boundary conditions, specify elasticity, and to solve the problems (Figure A-2). The core of the library is the element class, which is divided in two parts: the definition of the element geometry, and the physics of the elements or the behavior of the element. The outcome of combining the two parts results in the creation of a new element. Figure A-2 shows a section of the ITK FEM element class. Notice that from the Element class (`itk::fem::Element`) the space truss is defined by `itk::fem::ElementStd<2,3>` and the linear tetrahedron by `itk::fem::ElementStd<4,3>`. The first number in the class name implies the number of nodes in the element and the second number implies the dimension in which the element resides.

Following Figure A-2B, `itk::fem::Element3DCOLinearLine` is a class derived from `ElementStd` (`ElementBaseClass`), this class defines the geometry of the element by defining the following parameters. These parameters relate to the following the FEM by principles of virtual work.

- Integration Point and weight
- Number of Integration Points
- Shape Functions
- Shape Function Derivatives
- Get Local From Global coordinates
- Jacobian

In the class `itk::fem::Element3DStrain<Element3DCOLinearLine>`, `Element3DStrain` is a templates class that is used to define an element in 3D space. `Element3DStrain` together with `Element3DCOLinearLine` define the element in full. `itk::fem::Element3DCOLinearLineStrain` provides access to the following functions that sets the element stiffness matrix.

- Get Strain Displacement Matrix
- Get Material Matrix
- Get number of degrees of freedom per node

The following list [24] of bullets further explains Figure A-2.

- `itk::fem::LightObject`: base class that defines the entire FEM library.
- `itk::fem::Element`: Abstract base class created as the parent structure, like any base class no objects are created here; subclasses are derived and used to create the objects.
- `itk::fem::ElementStd`: Templated class that automatically defines the sum of the virtual functions in the elements. Three template parameters are defined here: number of nodes, number of spatial dimension, and the template class from which this class is derived.
- `itk::fem::ElementNode`: this class stores information required to define a node, like the node coordinates.
- `itk::fem::Load`: Abstract base class that defines external loads that act on the FEM system.
- `itk::fem::LoadElement`: Subclass that defines the external loads that act on the element. A force vector is defined; it has pointers that point to the element where the load acts.

- `itk::fem::LoadBC`: Class that applies essential or dirichlet boundary conditions, specifies which degrees of freedom are fixed in the model.
- `itk::fem::LoadNode`: Class used to specify a load on a point within an element object. A pointer to an element object, the number of the node on which the load acts, and the force vector.
- `itk::fem::Material`: Base class that defines the element's material properties,
- `itk::fem::MaterialLinearElasticity`: Class that defines the material properties of the finite elements, these are: E (elastic modulus), A(area), I (moment of inertia), nu (poisson ratio), h (thickness), and Rhoc (density multiplied by heat capacity).

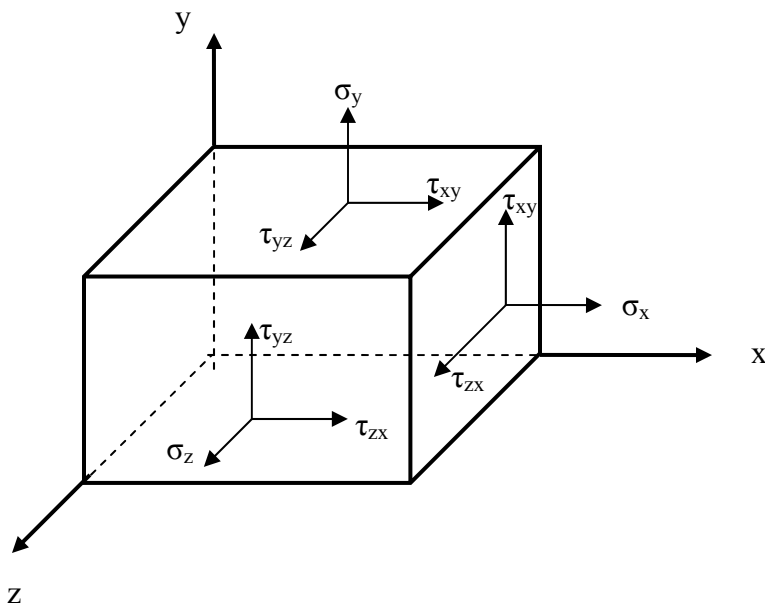


Figure A-1. Differential element subjected to real stresses and in equilibrium.

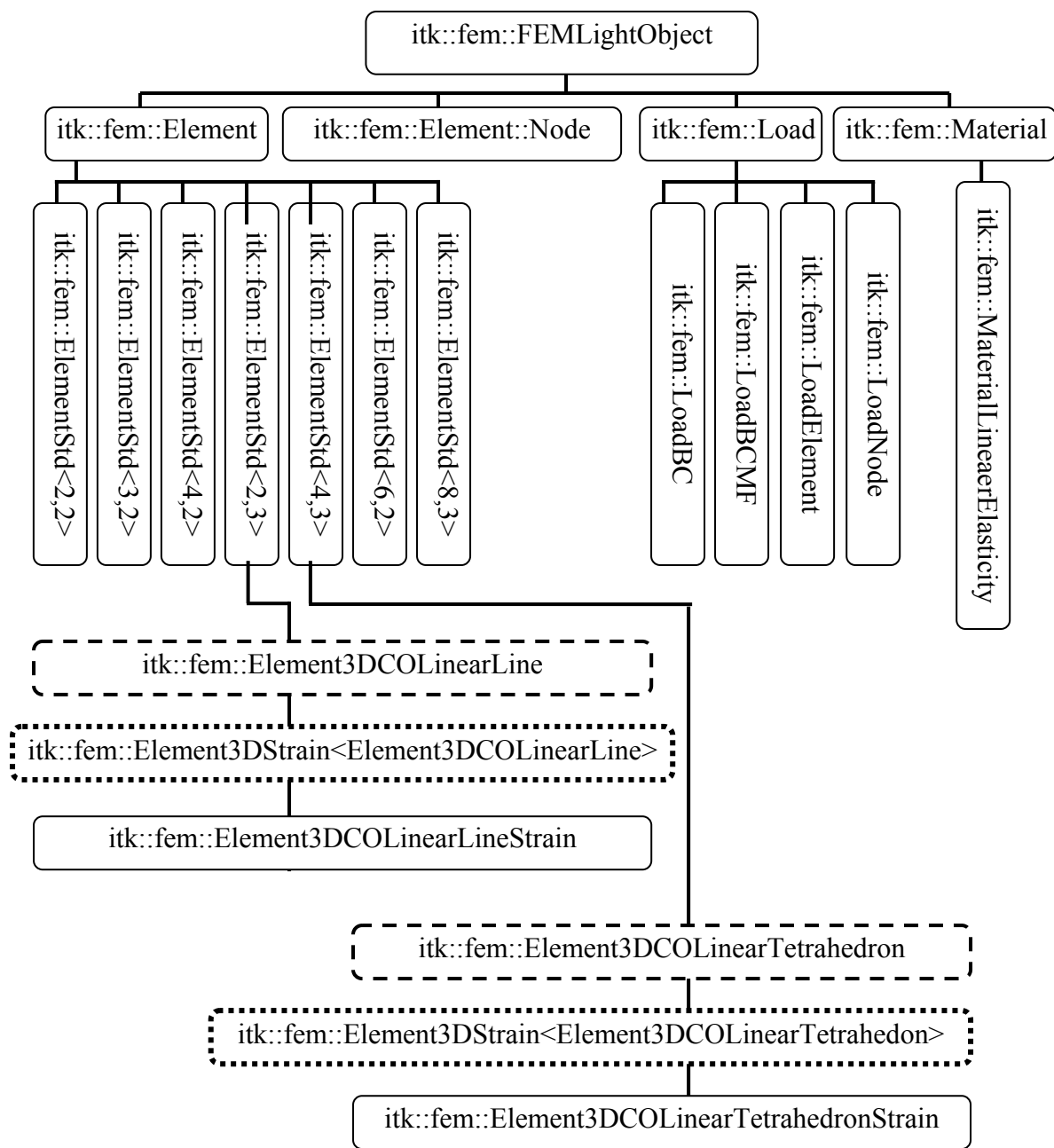


Figure A-2. The greater part of the ITK FEM library. The boxes surrounded by dashed lines represent where the geometry of the element is defined. The boxes surrounded by dotted line, represent where the physics of the problem is defined. Together they entirely define the element, in this cases the Element3DC0LinearLineStrain and the Element3DC0LinearTetrahedronStrain [24].

## LIST OF REFERENCES

1. Adler JR. Surgical guidance now and in the future. The next generation of instrumentation. *Clinical neurosurgery. Proceedings of the Congress of Neurological Surgeons*. San Diego, California 2001. Ed Lippincott Williams & Wilkins 2002;105-114.
2. Alker G, Kelly PJ. An overview of CT based stereotactic systems for localization of intracranial lesions. *Computational Radiology* 1984;8:193-196.
3. Allaire PE. *Basics of the finite element method*. Iowa: Wm. C. Brown Publishers, 1985.
4. Aslam, Kassimali. *Matrix analysis of structures*. California: Brooks/Cole Publishing Company, 1999.
5. Becker AA. *An introductory guide to finite element analysis*. New York: ASME Press, 2004.
6. Birnbaum Klaus, S.E., Decker Nils, Prescher Andreas, Ulrich Klapper, Radermacher Klaus. *Computer-Assisted Orthopedic Surgery with individual templates and comparison to Conventional Operation Method*. *Spine* 2001;26:365-370.
7. Bova, F. Grant proposal: Image-guided surgery based on rapid prototyping models. Department of Neurological Surgery, University of Florida. Gainesville, FL. March 2003
8. Brown RA: A computer tomography-computer graphic approach to stereotactic localization. *J Neurosurg* 1979; 50:715-720.
9. Brown RA: A stereotactic head form for use with CT body scanners. *Invest Radiol* 1979;14:300-304.
10. Cheney ML. *Facial surgery. Plastic and reconstructive*. Baltimore: Williams & Williams, 1997.
11. Cheung YK, Yeo MF. *A practical introduction to finite element analysis*. London: Pitman Publishing Limited, 1979.
12. Cowin, S. C. *Bone Mechanics*. New York: CRC Press, 2001.
13. Davis, T A. *User Guide for Cholmod: A Sparse Cholesky Factorization and Modification Package. Version 1.4*. Gainesville: Department of Computer and Information Science and Engineering, 2006.
14. D'Urso PS, Atkinson RL, Lanigan MW, Earwaker WJ, Bruce IJ, Holmes A, Barker TM, Effenev DJ, Thompson RG. Stereolithographic (SL) biomodelling in craniofacial surgery. *British Journal of Plastic Surgery* 1998;51:522-530.

15. D'Urso PS, Earwaker WJ, Barker TM, Redmond MJ, Thompson RG, Effeney DJ, Tomlinson FH. Custom cranioplasty using stereolithography and acrylic. *British Journal of Plastic Surgery* 2000;53:200-204.
16. D'Urso US Patent # 5,752,962. 1998.
17. Felippa Carlos. Introduction to finite element methods 2006. Department of Aerospace Engineering Sciences, University of Colorado at Boulder. Last Accessed 30 Jan 2006. <http://www.colorado.edu/engineering/CAS/courses.d/IFEM.d/>
18. Felippa Carlos. Nonlinear Finite Element Methods 2006. Department of Aerospace Engineering Sciences, University of Colorado at Boulder. Last Accessed 30 Jan 2006. <http://www.colorado.edu/engineering/CAS/courses.d/NFEM.d/>
19. Gildenberg PL. Stereotactic Surgery: Present and Past. In Heilbrun MP, ed. *Stereotactic Neurosurgery Vol 2: Concepts in Neurosurgery*. Baltimore:Williams & Williams, 1988.:1-16.
20. Goffin J., V.B.K., Vander Sloten J., Van Audekercke R., Smet M. H., Marchal G., Van Craen W., Swaelens B., Verstreken K. 3D-CT based, personalized drill guide for posterior transarticular screw fixation at C1-C2: Technical Note. *Neuro-Othopedics*1999;25:47-56.
21. Goffin Jan, Van Brussel Karel, Martens Kristen, Vander Sloten Jos, Van Audekercke Remi, Smet Maria-Helena. Three-dimensional computer tomography-based, personalized drill guide for posterior cervical stabilization at C1-C2. *Spine* 2001,21;12:1343-1347.
22. Heilbrun MP. Computed tomography-guided stereotactic system. *Clinical Neurosurgery*1984;31:564-581.
23. Horsley V, Clarke RH: The structure and function of the cerebellum examined by a new method. *Brain*1908;31:45-124.
24. Ibanez L., Schroeder. W., Ng L, Cates J. *The ITK Software Guide*.NewYork: Kitware Inc.,2003.
25. Loftis KL, Geer CP, Daneslson KA, Slice DE, Stitze JD. Analysis of pediatric head anthropometry using computed tomography for application to head injury prediction. 2007;43:86-90.
26. Mackerle J. Finite element modeling and simulations in orthopedics: a bibliography 1998-2005. *Comput Methods Biomech Biomed Engin*2006;9(3):149-199.
27. Maciunas RJ, Galloway RL, Latimer JW. The Application Accuracy of Stereotactic Frames. *Neurosurgery*1994;35(4):682-695.
28. Kim NH., Sankar B V. Lecture notes: EML 4500. Finite Elements analysis and design. Gainesville: Department of Mechanical & Aerospace Engineering, 2004.

29. Pham DT, Gault RS. A comparison of rapid prototyping technologies. *International Journal of Machine tools and Manufacturing* 1998;38:1257-1287.
30. Pikley WD, Pikley OH. *Mechanics of Solids*. New York: Schaum, 1974.
31. Popov, E P. *Introduction to mechanics of solids*. New Jersey: Prentice Hall, 1968.
32. Raabe A, Krishnan R, Zimmermann M, Seifert V: Frame-less and Frame-based stereotaxy? How to choose the appropriate procedure. *Zentralbl Neurochir.* 2003;64(1): 1-5.
33. Rajon DA, Bova FJ, Bhasin RR, Friedman WA. An investigation of the potential of rapid prototyping technology for image-guided surgery. *Journal of Applied Clinical Medical Physics* 2006;7(4):81-98.
34. Rajon DA, Bova FJ, Bhasin RR, Friedman WA. Poster Presentation: Fabrication of custom surgical guides using rapid-prototyping technology. University of Florida College of Medicine. Celebration of Research; March 20, 2007.
35. Saw CB, Ayyangar K, Suntharalingam N: Coordinate transformation and calculation of the angular paramters for stereotactic system. *Med Phy* 1987;14:1042-1044,.
36. Schad L, Lott S, Schmitt F, Sturn V, Lorenz WJ: Correction of spatial distortion in MR imaging: a prerequisite for accurate stereotaxy. *Journal Computer Assisted Tomography* 11(3):499-505, 1987.
37. Schileo E, Taddei F, Malandrino A, Cristofolini A, Viceconti M. Subject-specific finite element models can accurately predict strain levels in long bones. *Journal of Biomechanics*. 2007 doi: 10.1016/j.biomech.2007.02.010
38. Schroeder W, Lorensen B. *The visualization Toolkit*. New Jersey: Prentice Hall, 1997.
39. Sedef M, Samur E, Basdogan C. Real-time finite-element simulation of linear viscoelastic tissue behavior based on experimental data. *IEEE comput Graph Appl* 2006;26(6):58-68.
40. Smith KR, Frank KJ, Bucholz RD. The NeuroStation—a highly accurate, minimally invasive solution to frameless stereotactic neurosurgery. *Computerized Medical Imaging and Graphics* 1994;18(4):247-256.
41. Shewchuck JR. What is a good linear element? Eleventh International Meshing Round Table. New York: Sandia National Laboratories September 2002:115-126.
42. Spiegel EA, Wycis HT. *Stereoencephalotomy, Part I*. New York: Grune & Shatton, 1952.
43. Spiegel EA, Wycis HT, Lee MM. A: Stereotactic apparatus for operations on the human brain. *Science* 1947;106:349-350.
44. Spiegel EA, Wycis HT: Thalamotomy and related procedures. *JAMA* 1952;148:446-451.

45. Suresh G, Elliot N, Pinson N, Sinden FW. Simulation of dynamics of interacting rigid bodies including friction I: General problem and contact model. *Engineering and Computers* 1994;10:162-174.
46. Timoshenka. S P, Gere J M. *Mechanics of Materials*. California: Thomson Brooks/Cole Engineering Division, 1984.
47. Van Cleynenbreugel J., S. F., Goffin J., Van Brussel K., Suetens P.. Image-based planning and validation of C1-C2 transarticular screw fixation using personalized drilled guides. *Computer Aided Surgery*. 2002;7:41-48.
48. Van Staden RC, Guan H, Loo YC. Application of the finite element method in dental implant research. *Comput Methods Biomech Biomed Engin*. 2006;9(4):257-270.
49. Yan X, Gu P. A review of rapid prototyping technologies and systems. *Computer Aided Design*1996;28(4):307-318.
50. Yoo T. S., M.J., Chen D. T., Richardson A. C., Burgess J., *Template Guided Intervention: Interactive Visualization and Design for Medical Fused Deposition Models*. *Proceedings of the Workshop on Interactive Medical Image Visualization and Image Analysis* 2001;18:45-48.
51. Zamorano LJ, NolteL, Kadi AM, Jiang Z. Interactive intraoperative localization using an infrared-based system. *Stereotactic and Functional Neurosurgery* 1994;63:84-88

## BIOGRAPHICAL SKETCH

Barbara Garita Canet was born in 1977. She is the second child of Donato Garita and Noemi Canet who had six children. She grew up in San Jose, Costa Rica and attended Lincoln School from 1983 to 1995. After graduation from Lincoln School, she started her career in mechanical engineering at the Universidad de Costa Rica; however she only studied there for a semester. She was offered a scholarship for playing varsity volleyball for Florida Institute of Technology (FIT). From FIT she graduated with honors with a bachelor's degree in mechanical engineering in May 2000. In August 2000 she started a master's in biomedical engineering at the University of Florida and graduated in December 2002. The topic of her master's thesis was related to bone mechanics. From December 2002 to January 2003 she looked for a new committee chair to work on her doctorate. Finally, in January 2004 she stated her doctorate, on mechanical stability for customized instruments in image-guided surgery, and in August 2007 she completed her doctoral studies. Immediately after graduation she will rest and travel. She will then look for a job in biomedical engineering field and will write a business plan with the goal to start her own company.